Grain Boundaries, Deformation and Energy Dissipation in Water Ice

by

Tess E. Caswell

B.S., University of Alaska Fairbanks, 2009

Sc. M., Brown University, 2015

A dissertation submitted in partial fulfillment of the requirements for the degree of

Doctor of Philosophy in the Department of Earth, Environmental and Planetary Sciences

at Brown University

Providence, Rhode Island

May 2018

Tess Elaina Caswell

Zonta International Amelia Earhart Fellow
National Science Foundation Graduate Research Fellow

EDUCATION

Brown University, Providence, RI
Ph.D., Earth, Environmental and Planetary Sciences (Defense: December 2017)
M.Sc., Earth, Environmental and Planetary Sciences (Received: May 2015)
University of Alaska Fairbanks, Fairbanks, AK
B.S., Mechanical Engineering (Received: May 2009)
-Degree Emphasis: Aerospace Engineering. Minor: Mathematics
-Magna Cum Laude, Leadership Honors

PROFESSIONAL EXPERIENCE

NASA/JPL Planetary Science Summer School, Pasadena, CA *June – August 2015*

Project Manager, Testing the Habitability of Enceladus's Ocean (THEO) Concept Mission
-Primary point of contact for science/engineering integration and requirements verification during the THEO mission design process
-Received rigorous planetary mission design training from JPL's "Team X"

United Space Alliance, Houston, TX *June 2009 – July 2012*

Flight Controller, Environmental and Thermal Operating Systems (ETHOS), International Space Station (ISS)
-Monitored and controlled the life support and thermal systems of the ISS from the NASA Mission Control Center in Houston, TX
-Instructed flight controllers and astronauts on ISS environmental systems, internal thermal control systems, and emergency response
-Served as ETHOS Group Lead for U.S. Lab Vacuum System and primary liaison for associated science payloads

Alaska Space Grant Program, Fairbanks, AK *January 2005 – May 2009*

Team Lead, NASA Reduced Gravity Student Flight Opportunities Program
-Managed a student team in design, construction, integration and flight of two payloads aboard the NASA Reduced Gravity Aircraft
-Developed rigorous design and safety review documentation
Project Manager, Alaska Student Rocket Project (SRP) 5 Sounding Rocket Mission
-Supervised final integration and development of technical documentation for a student-built sounding rocket payload
-Managed student team during launch operations at Poker Flat Research Range, Alaska
Mechanical Engineering Team Lead
-Managed student employees

-Coordinated mechanical design elements of the SRP-5 payload with electrical and science requirements

Mechanical Engineering Student Assistant

-Designed and fabricated mechanical components of the SRP-5 payload

SKILLS

- Excellent teamwork, communication, and problem solving as demonstrated by real-time spacecraft operations
- Cryogenic Scanning Electon Microscopy and Electron Backscatter Diffraction (EBSD), including sample preparation, SEM operation, and data processing
- Instron Materials Testing Apparatus operation
- X-Ray Diffraction (XRD) operation and data analysis
- Matlab
- SolidWorks 3D CAD Software
- Mechanical design and integration
- Machining and fabrication

PUBLICATIONS

Caswell, T. E., D. L. Thorsen and J. G. Hawkins (2010), Preliminary Thermal Science Results of the Ionospheric Science and Inertial Sensing Sounding Rocket Payload, *Proceedings of the NASA Thermal and Fluids Analysis Workshop*, Houston, TX.

Prior, D. J., K. Lilly, M. Seidemann, M. Vaughan, R. Easingwood, S. Diebold, R. Obbard, C. Daghlian, I. Baker, **T. E. Caswell**, N. Golding, D. L. Goldsby, W. B. Durham, S. Piazolo, C. J. Wilson (2015). Making EBSD on water ice routine. *Journal of Microscopy.*

Caswell, T.E., R. F. Cooper and D. L. Goldsby (2015). The constant-hardness creep compliance of polycrystalline ice. *Geophys. Res. Lett.*, 42, doi: 10.1002/2015GL064666.

MacKenzie, S.M., **T. E. Caswell** et al. (2016) THEO Concept Mission: Testing the Habitability of Enceladus's Ocean. *Advances in Space Research,* 58 (6)

Caswell, T.E. and R. E. Milliken (accepted). Evidence for hydraulic fracturing of mudstones at Gale crater, Mars: Implications for burial depth of the Yellowknife Bay formation. *Earth and Planetary Science Letters.*

CONFERENCE PROCEEDINGS

Talks

- "Preliminary Thermal Science Results of the Ionospheric Science and Inertial Sensing Sounding Rocket Payload," *NASA Thermal and Fluids Analysis Workshop*, Houston, TX, 2011
- Invited: "Five Years, Zero Gravity, One Rocket; a Success Story Begun With the Alaska Space Grant," *National Space Grant Directors' Meeting*, Charleston, SC, October 14, 2013
- "The 'Hardness' of Ice-Ih: From Hart's Model to Tidal Dissipation," *Gordon Research Seminar, Rock Deformation,* Andover, NH, August 16, 2014
- "Exploring the microstructural 'hardness' of polycrystalline ice: An experimental approach," *Lamont-Doherty Earth Observatory Geophysics Seminar*, Pallisades, NY, October 10, 2014

- "Graduate Students Teaching Elementary Earth Science Through Interactive Classroom Lessons," *American Geophysical Union*, San Francisco, CA, December 17, 2014
- "Creep and the Characteristic Length Scale of Strain-Energy Dissipation in Polycrystalline Ice; Implications for Tidal Dissipation," *American Geophysical Union*, San Francisco, CA, December 16, 2015

Posters

- "The Role of Stress-Effected Subgrain Size Distribution in Anelastic Recovery: An Experimental Study on Polycrystalline Ice-Ih," *American Geophysical Union,* San Fracisco, CA, December 9-13, 2013.
- "Developing and testing models for creep of polycrystalline ice: new laboratory approaches," *American Geophysical Union,* San Francisco, CA, December 9-13, 2013
- "The 'hardness' of grain size-sensitive creep: An experimental study on Ice-Ih," *Gordon Research Conference, Rock Deformation*, Andover, NH, August 18, 2014
- "Grain size-sensitive creep and its relationship to grain size-insensitive attenuation in ice-I," *American Geophysical Union*, San Francisco, CA, December 16, 2014
- "Burial History of the Yellowknife Bay Formation: Insight from Fracture Morphology and Mechanics," *46th Lunar and Planetary Science Conference,* The Woodlands, TX, March 16-20, 2015
- "The Mechanical Attributes Characterization (MAC) Instrument; Linking Rock Properties to In-Situ Drill Data," *47th Lunar and Planetary Science Conference,* The Woodlands, TX, March 21-26, 2016
- "THEO Concept Mission: Testing the Habitability of Enceladus's Ocean," *47th Lunar and Planetary Science Conference*, The Woodlands, TX, March 21-26, 2016
- "Convection-Induced Microstructure and Tidal Dissipation in Polycrystalline Ice." *47th Lunar and Planetary Science Conference,* The Woodlands, TX, March 21-26, 2016
- "Grain size evolution in icy satellites: New experimental constraints." *48th Lunar and Planetary Science Conference,* The Woodlands, TX, March 20-24th, 2017

HONORS AND AWARDS

- Stephen E. Dwornik Student Award, GSA Planetary Geology Division, 2017
- Zonta International Amelia Earhart Fellow, 2016-2017
- National Science Foundation Graduate Research Fellow, 2013-2016
- Geological Society of America Bruce L. "Biff" Reed Scholarship Recipient, 2016
- Outstanding Student Paper Award, American Geophysical Union, 2016
- Elected to Sigma Xi, 2015
- Doctoral Research Travel Grant Award, Brown Univ., 2013, 2015
- Charles Wilson Brown Fellow, Brown Univ., 2012-2013
- Johnson Space Center Group Achievement Award, STS-135/ULF-7 Training Team, July 2011
- United Space Alliance Performance Award, August 2008
- Gerald A. Soffen Leadership Award, The NASA Academy at Goddard Space Flight Center, August 2007
- Tau Beta Pi Engineering Honor Society, 2007

LEADERSHIP EXPERIENCE

- President, Brown University GeoClub, 2013-2014
- President, Society of Women Engineers (SWE) – Texas Space Center (TSC), May 2011-June 2012 (Previous offices: Vice President May 2010-May 2011, Education and Outreach Committee Chair July 2009-May 2010)
- Head Instructor, UAF Aikido Club, 2007-2009
- President, SWE Farthest North (Fairbanks, AK), 2006-2008
- Vice President, Tau Beta Pi Engineering Honor Society, 2008-2009

SERVICE

- Executive Secretary, NASA Proposal Review Panels, 2016-2017
- GeoClub First Year Student Mentorship Co-Chair, 2015-present
- GeoClub Faculty Representative, 2015-present
- GeoClub Education/Outreach Volunteer Coordinator, 2013-2015
- Mentor, NASA Reduced Gravity Student Flight Opportunities Program, 2009-2012
- Volunteer Flight Director, Expedition Center at the George Observatory, 2009-2012
- Space Exploration Speaker, Advocate, and Consultant, 2004-present

Acknowledgements

The completion of a doctoral dissertation is a monumental undertaking and it would be impossible to thank each person who has had a positive influence on my time at Brown. For the "fun" aspects of graduate school – fellowship, moral support, and winning seasons with Billy's Blue Room – I thank the graduate students, faculty, and staff in DEEPS who make this Department a friendly and supportive community of scholars. During graduate school I have met some of the coolest, kindest, and most brilliant minds in the world, and made friendships that I expect will last a lifetime. Of course, a PhD comes with its fair share of challenges, too, and at many times throughout this process I have been immeasurably grateful for the support and guidance of my advisor, Professor Reid Cooper, who has patiently shepherded me over countless learning curves – for which the distributions of technical and philosophical "length scales" are undoubtedly self-similar. I have often leaned on the technical support of Tom Kiefer, who never failed to expertly machine the seemingly endless stream of parts for the lab, and I am grateful to David Goldsby for teaching me the ways of the Ice Lab. Finally, I thank my family: my parents, who always made it clear that I could succeed at anything I set my mind to, and my wife, Jenny, whose support was crucial to enduring what sometimes seemed like endless frustration in the lab and who, in sharing in the joy of successes along the way, has made the journey that much sweeter.

Ad Astra.

Table of Contents

Figures and Tables

1. Introduction

2. The Constant-hardness Creep Compliance of Polycrystalline Ice

3. Inhibited Grain Growth During Grain Size-sensitive Creep in Polycrystalline Ice; An Energy Dissipation Perspective

Chapter 1 | Introduction

Tess Caswell[1]

[1]Department of Earth, Environmental and Planetary Sciences, Brown University

Providence, Rhode Island 02912

1. The Planetary Context

Icy bodies throughout the outer solar system possess a dazzling array of geologic diversity. Pits, bands, and chaos terrain hint that warm ice upwells through the shell of Jupiter's moon Europa, warping and disrupting the surface (Greeley et al., 1998; Pappalardo et al., 1998; Pappalardo & Barr, 2004). At Saturn's Enceladus, geysers from the moon's enigmatic South Polar Terrain tap an ocean beneath the ice shell, producing plumes of water ice and vapor that feed the gas giant's E ring. The timing of plumes from the South Polar Terrain reflects the influence of gravitational tides on the moon's icy lithosphere (Nimmo et al., 2014; Porco et al., 2006; Waite Jr et al., 2009). At Uranus's moon Miranda, massive scarps may be the surface manifestation of tidally-heated convective upwelling within the ice shell (Hammond & Barr, 2014). Still further into the Solar System, plumes of nitrogen vapor erupt from the icy surface of Neptune's moon Triton. Finally, at Pluto, freezing and phase change within the ice shell may have generated global volume changes, inducing global stresses and networks of scarps on the dwarf planet's surface. Coupled with the extraordinarily young surfaces of some icy satellites (Triton's may be as young as 6 Ma in some locations (Schenk & Zahnle, 2007)), these observations suggest that despite their frigid surface temperatures, it is clear that icy worlds have undergone (and are still undergoing) a stunning variety of geophysical processes.

Though impacts play an obvious role in affecting the surfaces of many ice satellites, the role of plastic deformation within a thick, perhaps convecting, ice shell is strongly suggested by the myriad surface features described above. The low melting temperature of ice facilitates global melting and differentiation due to accretional or radiogenic heating early in a satellite's life. This leads to thick water/ice shells overlying silicate mantles (Consolmagno & Lewis, 1976) and, perhaps, Fe/Fe-S cores. Induced magnetic fields at Europa and Callisto indicate that some icy bodies maintain a global, salty liquid-water ocean to the present day (Khurana et al., 1998). Enceladus, too, appears to have a liquid ocean: in addition to the plumes erupting from Enceladus's South Polar Terrain, which suggest a regional sea, the moon's libration suggests that the ice shell is fully decoupled from the rocky mantle by a *global* ocean (Thomas et al., 2016; Waite Jr et al., 2009). Overlying these oceans, thick layers of water ice most likely undergo convection at some point in their history (Reynolds & Cassen, 1979).

In this context, viscoelastic properties of ice at planetary conditions are obviously paramount to developing realistic models of icy satellite geophysics. The coexistence of liquid oceans and convection presents an enigma, however, as ongoing convection in an H_2O layer as thin as Europa's would be expected to freeze the layer completely within a few tens of millions of years.

The process sustaining geological activity on many icy satellites is tidal heating, which stems from the dissipation of gravitational tides imposed on the ice shell. Tides are raised by the gravitational potential of the satellite's parent planet. If a satellite is tidally locked (that is, it presents the same face to its parent at all times) and is in a perfectly circular orbit (eccentricity, e, is zero), the tidal bulge is permanent and static. Deviations from perfectly synchronous rotation or perturbations to the satellite's orbital eccentricity, however, drive cyclic motion of the magnitude and position of the bulge and thereby generate time-varying stresses within the ice shell (Collins et al., 2009; Greenberg et al., 1998; Helfenstein & Parmentier, 1985). Dissipation of this time-varying tidal energy through viscous flow and anelasticity generate heat within the shell (Ojakangas & Stevenson, 1989). It is worth noting that, in addition to tidal heating, tidal stresses may directly fracture the icy lithosphere. Tidal stresses, however, are generally on the order of 10-100 kPa – far less than the fracture strength of pure, undamaged water ice (which is ~1 MPa in tension). Some mechanism must therefore be invoked to weaken the ice shells before tidal stresses can generate fractures.

The role and relative importance of tidal heating varies between satellites. In some cases (e.g. Enceladus and Europa), tidal heating is required to explain any activity at all; while oceans within larger icy satellites (e.g. Triton or Callisto) may be sustained by radiogenic heat from their rocky cores (Cassen et al., 1979; Consolmagno & Lewis, 1976; Schenk & Zahnle, 2007), many satellites' radiogenic and accretionary heat alone are insufficient to sustain a liquid ocean for more than a few tens of millions of years (Roberts & Nimmo, 2008; Waite Jr et al., 2009). In other cases, such as that of Uranus's moon Miranda, one must invoke tidal energy to develop a geothermal gradient appropriate to the magnitude and wavelength of observed topography (Hammond & Barr, 2014; Pappalardo et al., 1997). Finally, within satellites such as Europa, tidal heating may drive surface expressions of convective upwelling within the ice shell (Pappalardo & Barr, 2004). Tidal heating plays a fundamental role in each of these scenarios. The key to understanding geologic activity within these tiny, yet active, icy worlds is thus tidal heating.

But *how* is heat generated – and how much? When a material undergoes cyclic loading such as tidal forcing, the amount of heat produced per cycle of loading is expressed by attenuation (Q^{-1}), which is in the inverse of the tidal quality factor, Q.

Attenuation is first-order when calculating the amount of heat generated ($\dot{F}_{Tidal}$) in an icy body subjected to tidal forces:

$$\dot{F}_{Tidal} = \frac{21}{2}\left(\frac{k_2}{Q}\right)\frac{r_S^5 \Theta M_P^2 m e^2}{a^6} \qquad [1]$$

where R_S is the radius of the satellite, Θ is the gravitational constant, M_P is the mass of the parent planet, m is the satellite's mean motion (the satellite's average angular velocity throughout its orbit), e is the satellite's orbital eccentricity, a is the semi-major axis of the satellite's orbit, and k_2 is the degree-two tidal Love number [see Moore & Schubert (2000) for representative values]. The Love number describes the magnitude of the deformation of a planetary body in response to an imposed tidal potential, and is a function of the rigidity of the planet (or moon). Attenuation describes the amount of energy dissipated per cycle of loading and depends upon the rheological mechanism that gives rise to tidal dissipation (Cassen et al., 1979).

The value of Q has been estimated in many ways, most often beginning with the assumption that an icy satellite's interior behaves as a Maxwell Solid. In the absence of definitive mechanical data on the rheology of an icy satellite's interior and lacking a solid understanding of the physics at the heart of Q, this assumption has allowed investigators of planetary geophysics to represent the material within the tidally-deformed body as a mechanical spring and dashpot in (mechanical) series, for which rigidity and dissipation can be analytically derived.

A Maxwell solid does not account for transient creep or anelasticity, however, and as a result, does not accurately depict the response of real materials to transient or time-varying loading. Models of tidal dissipation – which is a distinctly transient and time-varying process – relying on values of Q derived using the Maxwell model are thus suspect. Thus, poor understanding of the physics of tidal dissipation hobbles the community's efforts to understand the geophysics of icy worlds. A realistic rheology for icy planetary interiors and a deeper understanding of the means by which this rheology transforms time-varying, tidal energy into heat are required in order to realistically model icy satellite geophysics.

This work addresses the fundamental mechanism of ice rheology at planetary conditions – Grain Boundary Sliding (GBS) – through exploration of the physics at the heart of GBS (Chapter 2) and the effect of GBS on grain size evolution within a deforming ice shell (Chapter 3). These findings bolster our interpretation of measured attenuation (Q^{-1}) in polycrystalline ice simultaneously deforming via GBS. The complete work sheds light on the physics of ice deformation in ice satellite interiors, contributing to a better understanding of worlds beyond our own.

The interpretation of the following chapters relies on an understanding of two fundamental topics: (i) ice rheology and (ii) grain boundary structure and energetics. The remainder of this chapter provides an overview of these subjects as a means of familiarizing the reader with critical subjects at the heart of the research presented here.

2. Ice Rheology

The rheology of water ice has been studied extensively because of its criticality to terrestrial glaciology as well as to planetary science. In particular, the rheology of polymorph ice Ih, which is stable at terrestrial pressures and temperatures, has been explored in numerous experimental studies at glaciological conditions (Glen, 1955;

Montagnat & Duval, 2000; Piazolo et al., 2013; Wilson & Peternell, 2012) and planetary conditions (e.g., Durham et al., 2001; Goldsby & Kohlstedt, 2001).

Studies of ice in the terrestrial context are often based upon the pioneering work of Glen (1955), who measured the creep response of cylinders of polycrystalline ice at stresses (~0.1-1 MPa) and temperatures (260-273K) similar to those within a terrestrial glacier or ice sheet. Glen observed power-law creep of the form

$$\dot{\varepsilon} = \alpha\sigma^{n}\exp\left(\frac{-E}{RT}\right) \qquad [2]$$

where $\dot{\varepsilon}$ is strain rate, α is a pre-exponential constant, σ is deviatoric stress, E is activation energy, R is the gas constant and T is temperature. For the stress exponent, n, Glen identified a value of approximately 3. This value has been applied extensively in the terrestrial glaciological literature as the "Glen Law" (Cuffey & Paterson, 2010). Though Glen did not report grain size-sensitivity in his experimental data, some authors have incorporated grain size effects into a multiplicative enhancement factor, E, applied to Eq. (2) (e.g., Cuffey et al., 2000). Enhancement factors based on c-axis fabric development. debris content, and chemical impurities have also been used to make models match nature (Cuffey et al., 2000; Paterson, 1991).

Scrutinizing Glen's original work, however, reveals that a stress exponent of 3 does not fit the data well across the measured range; the Glen Law systematically underestimates the strain rate at the high and low ends of the range of deviatoric stresses studied, suggesting that the stress exponent (and, hence, rate-limiting creep mechanism) actually changes in the range studied. (Goldsby & Kohlstedt, 1997, 2001) attributed this change in slope to a switch in rate-limiting rheological mechanism, further demonstrating that the transition point between mechanisms was influenced by grain size. These authors conducted a suite of experiments exploring the roles of grain size, stress and temperature on polycrystalline ice at ambient pressure. They observed three rate-limiting processes in the creep of polycrystalline ice, all of which are non-Newtonian (i.e., $n \neq 1$): dislocation creep, which dominates at high temperature, coarse grain sizes, and high deviatoric stress; GBS rate-limited by sliding on the boundary, which is mildly grain size-sensitive; and GBS rate-limited by basal dislocation glide, which is grain size-insensitive. Though it was not experimentally observed, Goldsby and Kohlstedt (2001) hypothesized that a fourth creep regime, Newtonian diffusional creep, would exist at sufficiently low stress and fine grain sizes. As of this writing, diffusional creep has never been explicitly observed experimentally – though the work presented here in Chapter 2 hints at diffusional stress relaxation.

(Goldsby & Kohlstedt, 2001) articulated a composite flow law incorporating the roles of each deformation mechanism described above:

$$\dot{\varepsilon} = \dot{\varepsilon}_{diff} + \left(\frac{1}{\dot{\varepsilon}_{basal}} + \frac{1}{\dot{\varepsilon}_{gbs}} \right)^{-1} + \dot{\varepsilon}_{dis} \tag{3}$$

where $\dot{\varepsilon}_{diff}$, $\dot{\varepsilon}_{basal}$, $\dot{\varepsilon}_{gbs}$, and $\dot{\varepsilon}_{dis}$ are, respectively, the strain rates due to diffusion creep, basal slip-limited GBS, boundary sliding-limited GBS, and dislocation creep. The form of Eq. (3) indicates that while diffusion creep and dislocation creep are parallel (independent) kinetic processes, GBS in ice is a serial kinetic process of sliding along the boundary and basal dislocation glide – that is, one must occur in order for the other to continue.

Boundary sliding-limited GBS and diffusion creep include a grain size exponent, p, such that Eq. 2 takes the form.

$$\dot{\varepsilon}_{gbs} = \frac{A\sigma^n}{d^p} \exp\left(\frac{-E}{RT}\right) \qquad [4]$$

Note that in this case the semi-empirical pre-exponential factor, A, is different from α described for Eq. (2) in that it includes grain size-sensitivity.

The rheology is described schematically in Fig. 1. Each mechanism is briefly described in the following sections, though the reader is referred to detailed reviews, such as Durham et al. (2010), for thorough treatment of the topic.

2.1. Dislocation Creep

Dislocation creep occurs through the glide and climb of one-dimensional crystallographic defects known as dislocations. In order for the dislocations to glide, shear stress applied on the glide plane must combine with thermal energy to overcome the lattice resistance to dislocation motion (i.e., the distorted bonds constituting the dislocation must be stretched to the point of breaking, thus allowing the dislocation to propagate). Dislocations will glide until an obstacle is met or the driving force for motion is removed. Thus, dislocation creep can either be rate-limited by glide ("glide-controlled," in which case lattice friction is rate-limiting) or by the process of overcoming obstacles to glide ("climb-controlled") (Poirier, 1985, p. 94). Above 60% of the melting temperature ($T_H = T/T_{\mathrm{m}} = 0.6$), climb is generally considered to be rate-limited by lattice diffusion, though numerous experimental measurements of stress exponents, $n > 3$ (Eq. 4) are inconsistent with this theory (Frost & Ashby, 1982). At lower temperatures,

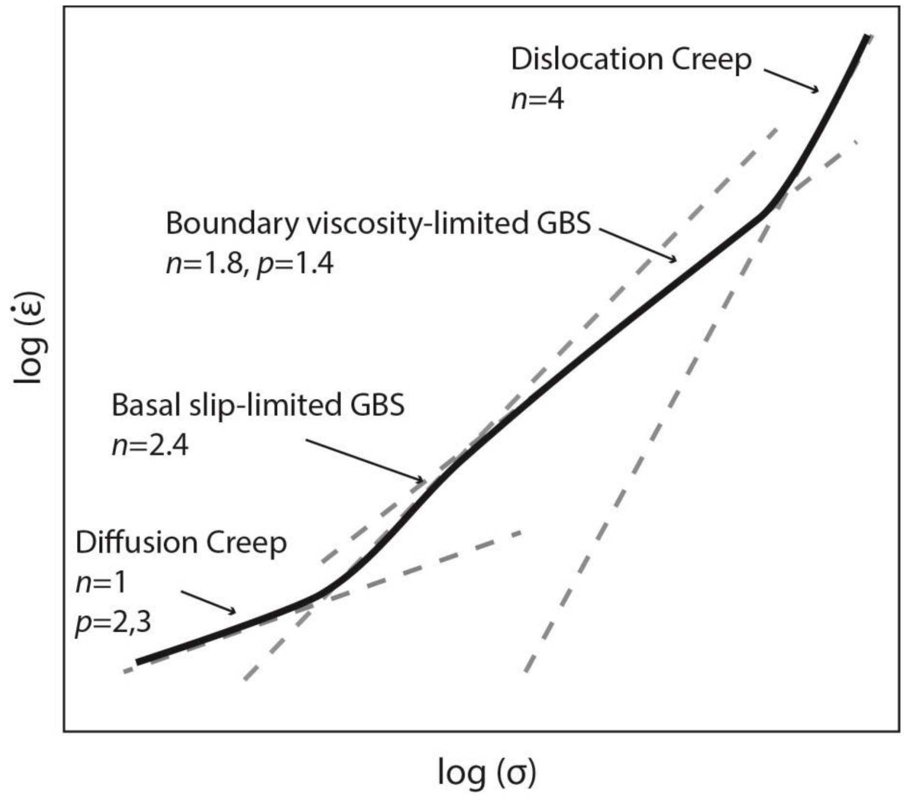

Figure 1: Schematic representation of the composite rheology of pure, polycrystalline water ice according to Goldsby & Kohlstedt (2001). The composite curve shown is for a constant grain size and temperature. The concave-up nature of the transition between dislocation creep and GBS indicates that the mechanisms are independent (kinetic parallel): under given (P, T, σ, d) conditions, the faster of the two mechanisms will dominate. The concave-down nature of the GBS regime illustrates that boundary sliding and basal slip are in kinetic series, and thus the slower of the two processes rate-limits deformation. The values of stress exponent (n) and grain-size exponent (p) are provided for each kinetic segment of the rheology (Eq. 4).

dislocation core diffusion may contribute a substantial fraction of the measured strain rate (Frost & Ashby, 1982). The observed activation energy for dislocation creep in ice, ~60 kJ/mol, is in good agreement with that for molecular self-diffusion of H_2O in ice (Goldsby & Kohlstedt, 2001; Ramseier, 1967).

Dislocation creep in ice is highly anisotropic and is dominated by slip on the basal plane. Ice possesses a very low stacking fault energy, which favors the dissociation of $(1/3)[11\bar{2}0]$ basal dislocations into two partials, $(1/3)[10\bar{1}0]$ and $(1/3)[01\bar{1}0]$ separated by a stacking fault approximately 20 nm wide. Cross-slip of these dissociated dislocations requires that the partials be constricted (Fukuda et al., 1987). Given this extra energy barrier to cross-slip, the dislocations tend to remain on the basal plane. Thus, though the dislocation *velocity* is higher on the prismatic planes in ice, the dislocation *density* is much lower and glide on these planes does not contribute significantly to the macroscopic strain rate (Fukuda et al., 1987).

2.2. Grain Boundary Sliding

In the regime of grain boundary sliding, which is favored by low stress, high temperature, and fine grain size, deformation occurs by accumulated shear along grain boundaries (Poirier, 1985; Raj & Ashby, 1971). Steps in the process of GBS can be illustrated by imagining a network of polygonal grains. When a shear stress is applied, the grains are driven to move relative to each other, sliding along the grain boundary interface until the grains impinge upon one another at triple junctions or at interlocking grain boundary topography. Initial sliding proceeds until triple junctions or topography are encountered, at which point limited additional strain is possible by elastic flexure of the contact points. (If load were removed at this point, the elastic strain would relax, rate-limited by the grain boundary viscosity – this is “elastically-accommodated Grain Boundary Sliding.”) In order for plastic strain to accrue, the obstacles resisting sliding must be eradicated by internal deformation of the grains. This may occur by diffusive flux away from stressed regions of the adjoining grains or by emission of dislocations from the compressed region (Raj & Ashby, 1971). Thus, GBS is a serial-kinetic process of sliding along the boundaries and eradication of obstacles to continuing glide. In ice, obstacles to grain boundary shear are removed predominantly by glide of basal dislocations. GBS in ice therefore exhibits two regimes: one rate-limited by the grain boundary viscosity and one rate-limited by basal dislocation glide.

Grain size-sensitivity arises when the grain boundary viscosity rate-limits GBS, necessitating a grain size exponent, p, of 1.4 (Eq. 4). This grain size-sensitivity indicates a contribution of grain boundary processes but is not consistent with purely diffusional creep, for which $p = 2$ for volume diffusion or 3 for grain boundary diffusion (Coble, 1963; Herring, 1950; Nabarro, 1948). Creep in this regime is nonlinear, as well, with a stress exponent, n, of 1.8. Such nonlinearity indicates a contribution from dislocation plasticity. The combination is consistent with “dis-GBS,” or grain boundary sliding that is geometrically accommodated by a dislocation motion (Ball & Hutchison, 1969; Langdon, 1991). Furthermore, the microstructures of samples deformed in this regime display equant grain sizes and shapes, as well as numerous four-grain junctions – a microstructural feature considered diagnostic of GBS (Ashby & Verrall, 1973; Caswell et al., 2015; Goldsby & Kohlstedt, 1997, 2001).

At still lower stresses, dislocation emission to remove obstacles to sliding becomes the rate-limiting process of GBS. In this regime, the stress exponent increases to

2.4 and the grain size sensitivity disappears (Fig. 1). The stress exponent and activation energy measured in this regime by Goldsby & Kohlstedt (2001) are consistent with deformation of ice single crystals oriented for basal slip (e.g., Readey & Kingery, 1964). Because of the concave-down transition between the n=2.4 and n=1.8 regimes in Fig. 1, Goldsby & Kohlstedt (2001) inferred that the two rate-limiting processes in these regimes are serial-kinetic. Thus the n = 2.4 regime is considered to be GBS rate-limited by basal dislocation glide.

2.3. Diffusion Creep

Though it has yet to be conclusively observed experimentally, diffusion creep is hypothesized to rate-limit the deformation of ice at sufficiently low stresses and fine grain sizes (Fig. 1). This prediction is based upon the measured thermodynamic properties (Eq. 4) of the mechanisms observed by Goldsby and Kohlstedt (2001), compared to the constitutive equation for diffusion creep (Coble, 1963; Herring, 1950; Nabarro, 1948), parameterized by measured values of diffusion in ice (Ramseier, 1967). Despite the fact that diffusion creep has not be conclusively identified in the laboratory setting, it is often assumed, on the basis of the Goldsby & Kohlstedt (2001) parameterization (which is an entirely theoretical lower-bound on the viscosity), to play an important role in icy satellite interiors (Barr & Pappalardo, 2005).

3. "Grain Boundaries Are Not Amorphous Goo"

The rate of grain boundary sliding is intimately linked to the structure of the grain boundary itself, which is first-order in determining the landscape of grain boundary tractions and, hence, the chemical potential gradients that drive GBS (Raj & Ashby, 1971). Sliding is accomplished by the motion of Grain Boundary Dislocations (GBD's) whose density and rate of motion are functions of the microscopic boundary structure (Ashby, 1972; Hirth, 1972; Sutton & Balluffi, 1995). Interpreting the following chapters thus relies heavily on an understanding of the structure of grain boundaries, how they evolve under deviatoric stress, and how they respond to the chemical potential gradients that drive viscoelastic processes.

A grain boundary is a two-dimensional interface along which two grains of differing orientations (and/or phases) meet. In general, grain boundaries can be thought of as having both macroscopic and microscopic degrees of freedom: macroscopic degrees of freedom are defined by the relative orientations of the adjoining crystal lattices (three degrees of freedom are used to define a proper rotation) and the orientation of the grain boundary plane (two degrees of freedom specify the boundary normal), while microscopic degrees of freedom describe the atomic structure of the interface (Sutton & Balluffi, 1995, p. 21). Alternatively, the five macroscopic degrees of freedom can be assigned in a manner that focuses on the boundary plane by specifying the normal to each crystal surface to be joined, then specifying a rotation angle around either of those normal vectors (Sutton & Baluffi, 1995, p. 21), In the case of a single-phase polycrystal, the lattices on either side of the boundary can be related by simple rotations and translations (Sutton & Balluffi, 1995). Figure 2 demonstrates a simple grain boundary structure using a dot matrix that schematically represents the {100} plane of a simple cubic crystal. A simple matrix of blue dots ("bubbles") represents the crystal structure of Grain A, while the matrix of semitransparent, red dots represents the crystal structure of Grain B (Fig. 2a). The two hypothetical structures meet along a planar boundary parallel to the page, and are perfectly matched across this boundary (they are epitaxially registered) in Fig. 2b.

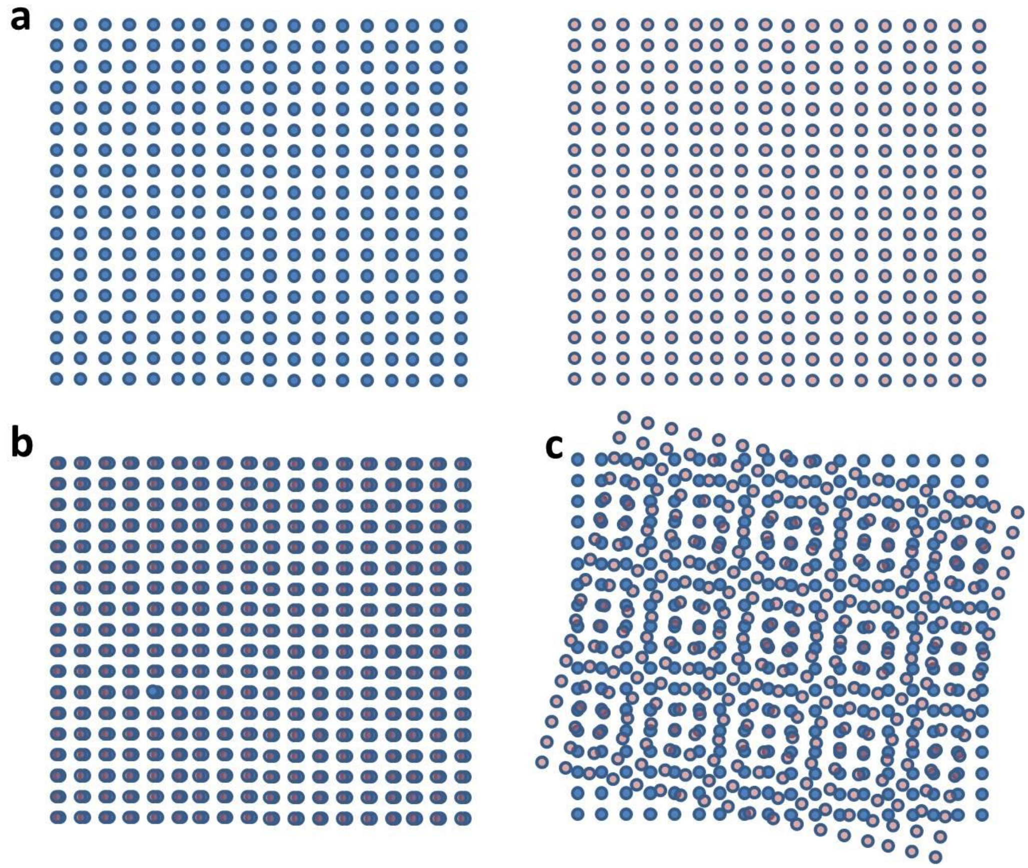

Figure 2: Schematic representation of grain boundary structure. When the basal plane of two simple cubic lattices, represented by the red and blue dot matrices in (a), are placed adjacent to one another as if along a grain boundary (as in b) and then rotated with respectect to one another (as in c), the boundary forms a "fit-misfit" pattern of a coincident site lattice separated by linear intrinsic grain boundary dislocations (GBD's). In this case, the pattern formed is an orthogonal array of screw dislocations. During grain boundary sliding, GBD's glide and climb in the boundary plane.

When one grain is rotated relative to the other, however, once sees that the grain boundary transforms into a pattern with two types of regions: those with poor fit between the structures on either side of the boundary, and those with good fit (Fig. 2c). Regions of fit are separated by linear defects on the plane of the boundary that are known as intrinsic grain boundary dislocations (GBDs). The "fit-misfit" pattern is not random (Baluffi et al., 1982): the density, orientation and type of GBDs formed is a function of the lattices on either side of the boundary and their relative orientations. Between the GBD's, the regions of fit create a Coincident Site Lattice (CSL). A CSL is generally described by the reciprocal density, Σ, which is defined as the inverse of the proportion of coincident sites (Hondoh & Higashi, 1978; Poirier, 1985, p. 64).

The hypothetical boundary in Fig. 2 is a "twist" boundary in which the rotation axis and the boundary normal coincide. "Tilt" boundaries, in which the rotation axis lies perpendicular to the boundary normal, and mixed boundaries are also possible. The salient point is that grain boundaries are not, generally, amorphous; they have a structure borne of the symmetry between crystal lattices on either side of the boundary (Hirth, 1972).

Grain boundary dislocations are integral to the process of grain boundary sliding. As two grains slide past each other, GBDs must glide and climb to prevent voids from nucleating in the grain boundary (Ashby, 1972). These processes require diffusive flux of atoms along and across the grain boundary. Based on an atomistic approach to deriving the velocity of GBDs during sliding, Ashby (1972) posited that if diffusion is the rate-limiting step in GBD motion and there is a sufficiently high GBD density, the continuum model of diffusion creep can be derived from GBD motion. Grain boundaries are not perfectly planar, however, and the motion of GBDs can be impeded by this grain boundary topography. Of particular relevance are facets, which have been observed to form in ice along grain boundaries subjected to deviatoric stress (Figure 3; Hondoh & Higashi, 1983). Stress concentrations generated by GBS that emit lattice dislocations into the adjoining crystals suggest that GBDs form pileups at facet intersections (Fig. 3c) (Hondoh & Higashi, 1983). Thus, faceting of a grain boundary hardens it by increasing the resistance to GBD motion – a process that is explored in detail in Chapter 2.

Facets form in order to reduce the free energy of the grain boundary. Grain boundaries have an associated energy, γ_{GB}, generally expressed in J m^{-2}. At low misorientation angles, this energy can be directly related to the density of dislocations in the boundary through the Read-Shockley formula:

$$\gamma_{GB} \cong \gamma_o \theta \left(\xi - \ln \theta \right) \qquad [5]$$

where θ is the misorientation angle of the boundary, ξ is a constant related to the energy of dislocations in the boundary, and γ_o is related to the elastic properties of the material:

$$\gamma_o = \frac{Gb}{4\pi(1-\nu)} \qquad [6]$$

Here *G* is the shear modulus, *b* is the magnitude of the burgers vector, and ν is Poisson's ratio. The energy of dislocations in the boundary, ξ in Eq. 5, is calculated as :

$$\xi = \frac{4\pi(1-\nu)C_E}{Gb^2} - \ln\left(\frac{r_o}{b}\right) \qquad [7]$$

where C_E is the energy per unit length of a dislocation core and r_o is the dislocation core radius. This straightforward relationship is based on a model of low-angle tilt boundaries

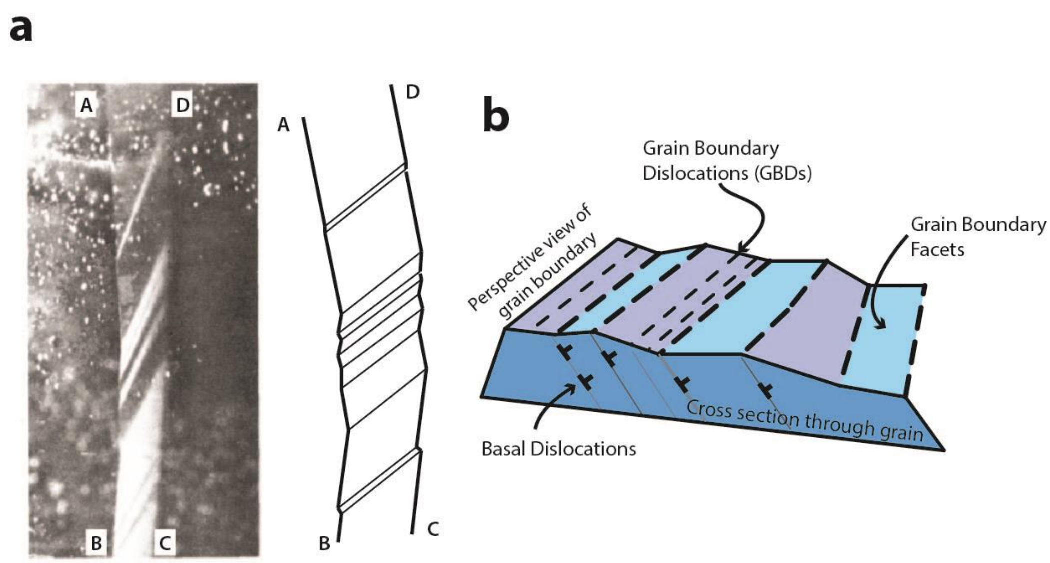

Figure 3: (a) Faceting along the grain boundary in an ice bicrystal, photographed in transmitted light (left) and drawn schematically (right). The image is looking down on a boundary inclined relative to the page. The actual boundary width (BC) is ~ 5mm. Reproduced from Hondoh & Higashi (1983). During these authors' study, 34° tild boundaries in ice bicrystals were subjected to shear stress of ~100 kPa. They have interpreted the variations of refracted light along the grain boundary to be facets with orientations varying as in the sketch. (b) Schematic interpretation of the structure of grain boundaries during deformation of polycrystalline ice (Caswell et al., 2015). GBDs (light-dashed lines) are able to glide along facets but pile up at facet intersections (heavy-dashed lines). Stress concentrations due to these pileups cause emission of lattice dislocations, which relieve pileup stresses and allow sliding to continue; thus, grain boundary structure plays a first-order role in GBS in ice.

in which the tilt misorientation angle, θ, is derived from the Burgers vector and the spacing of dislocations:

$$\theta = \frac{b}{S} \qquad [8]$$

where b is the magnitude of the burgers vector and S is the dislocation spacing in the boundary.

Equations (5)-(8) agree well with experimental data for low-angle grain boundaries (Sutton & Balluffi, 1995). The distinction between “low-” and “high-“ angle boundaries is somewhat arbitrary, though the Read-Shockley equation reaches an asymptotic value at θ~15°. At higher misorientations, grain boundary energy has been determined for ice from measurements of grain boundary groove angles under liquid and vapor (Ketcham & Hobbs, 1969). A mean value of 0.065 J m^{-2} is accepted for Ice Ih, although this value is diminished by a factor of ~5 when the boundaries are aligned in CSL orientations (Druetta et al., 2013). The latter factor may promote facet formation; Hondoh & Higashi (1983) noted that the orientations of facets in ice grain boundaries under load corresponded to the close-packed directions of the boundary CSL (Hondoh & Higashi, 1983). Thus, facet formation may lower the overall free energy of the system by reducing local interfacial energy energy.

Each of the phenomena described here is intimately linked to grain boundary sliding. The boundary between two ice crystals in a polycrystalline matrix, when subjected to a long-range shear stress, will evolve into a faceted grain boundary composed of patches of low-energy CSL orientations separated by grain boundary dislocations. The GBDs glide and climb in the boundary plane as the grain boundary shears, but their motion is inhibited by facet intersections; the slowest step in this process is the rate-limiting step in the regime of grain boundary sliding rate-limited by the boundary viscosity. Ultimately, these microscopic processes control the macroscopic viscosity of ice and, therefore, the tectonics of icy worlds.

4. Attenuation: From Grain Boundaries to Tidal Dissipation

Grain boundaries are integral to the process of low-frequency (seismic to sub-seismic) attenuation and, hence, to tidal dissipation in ice (Section 1). Prior to delving into the relationship between grain boundaries and attenuation, however, it is worth describing some of the basics of attenuation.

4.1. Viscoelasticity and Complex Compliance

Attenuation (also known as internal friction or mechanical damping) is the transformation of mechanical strain energy, imposed by a time-varying cyclic load, into heat. It is generally presented as Q^{-1}, defined as the ratio of energy dissipated (W_d) to energy stored (W_S) within a material during a cycle of loading (Nowick & Berry, 1972):

$$Q^{-1} \equiv \frac{1}{2\pi}\left(\frac{W_d}{W_S}\right) \qquad [9]$$

Attenuation arises from the *viscoelastic* properties of a material. Many readers will be familiar with elastic deformation; that is, strain resulting from distortion of atomic bonds that is fully and nominally immediately recovered upon removal of load. Similarly, most will be familiar with purely viscous behavior – deformation that results from the motion of crystalline defects and is not recovered once load is removed. From a thermodynamics perspective, elasticity is fully reversible (100% of the energy require to stress interatomic bonds is recovered when load is removed), while plastic deformation is irreversible (100% of the energy invested in moving crystallographic defects is dissipated irreversibly as heat) (Cooper, 2002). When strain is fully recovered over time, rather than instantaneously, it is known as anelasticity. Viscoelasticity is, in a sense, a combination of all three, with time-dependent relationships between stress and strain (Lakes, 1998).

Q^{-1} can be modeled from time-dependent viscoelastic properties. A common formulation uses the compliance (J), which is defined as the ratio of strain to stress. If strain increases with time due to viscous deformation, then compliance is a time-dependent function. In the case of a constant-stress (creep) experiment, the compliance increases with time from J_o, the unrelaxed compliance observed at initial loading, to a time-dependent value, $J(t) = \varepsilon(t)/\sigma$.

The time-dependent compliance thus requires a model for time-dependent strain. Historically, the viscoelastic properties of real materials have been modeled by combinations of springs and dashpots, with one of the most commonly used being the Burgers solid (Fig. 4) (Cooper, 2002; Faul & Jackson, 2005; Findley et al., 1976). The Burgers solid represents elasticity and steady-state creep as a spring and dashpot, respectively, in mechanical series, and represents anelasticity (time-dependent, recoverable strain) as a spring and dashpot in mechanical parallel. The time-dependent compliance of a Burgers solid is shown schematically in Fig. 4. When a Burgers solid is subjected to a constant stress at $t > 0$, it first produces instantaneous, elastic deformation, then a decelerating transient leading to steady-state creep. The latter components constitute time-dependent, inelastic strain – both plastic (irrecoverable) and anelastic (recoverable). Unfortunately, the Burgers solid underestimates the contribution of anelastic strain (Cooper, 2002). This inadequacy was addressed by building "extended"

Burgers solid models, with numerous viscoelastic elements in mechanical series (e.g., Faul & Jackson, 2005), to match real data. The use of an extended Burgers solid presents a challenge, however, in that in order to be physically sound, the distinct compliance of each element must be tied a physical process (Cooper, 2002).

Though spring and dashpot models such as the Burgers solid are useful pedagogical tools, an alternative model for time-dependent strain was proposed by Andrade (1910). The Andrade function represents elastic, transient, and steady-state behavior as (Andrade, 1910):

$$\varepsilon(t) = \sigma\left[\left(\frac{1}{Y}\right) + \left(\beta t^{\psi}\right) + \left(\frac{t}{\eta_{SS}}\right)\right] \quad [10]$$

where Y is Young's modulus, β and ψ are constants related to rate and magnitude transient creep (Bunton, 2001), and η_{ss} is the steady-state viscosity. The Andrade model matches transient creep data well, and was tied to a physical foundation by Gribb & Cooper (1998). Through study of extremely fine-grained polycrystalline olivine carefully fabricated to induce diffusion creep, these authors showed that the power-law term associated with transient creep captured the physics of the diffusional evolution of tractions on grain boundaries (Raj, 1975). Thus, the Andrade model provides a model of time-dependent strain that captures the behavior of real materials well and has a physically-sound basis. The Andrade model was first applied to ice by Duval (1978), and parameterized with β = 4.5×10^{-12} and ψ=0.25 by McCarthy & Cooper (2016) for polycrystalline ice creeping at 1 MPa in the regime of GBS rate-limited by sliding on the grain boundaries.

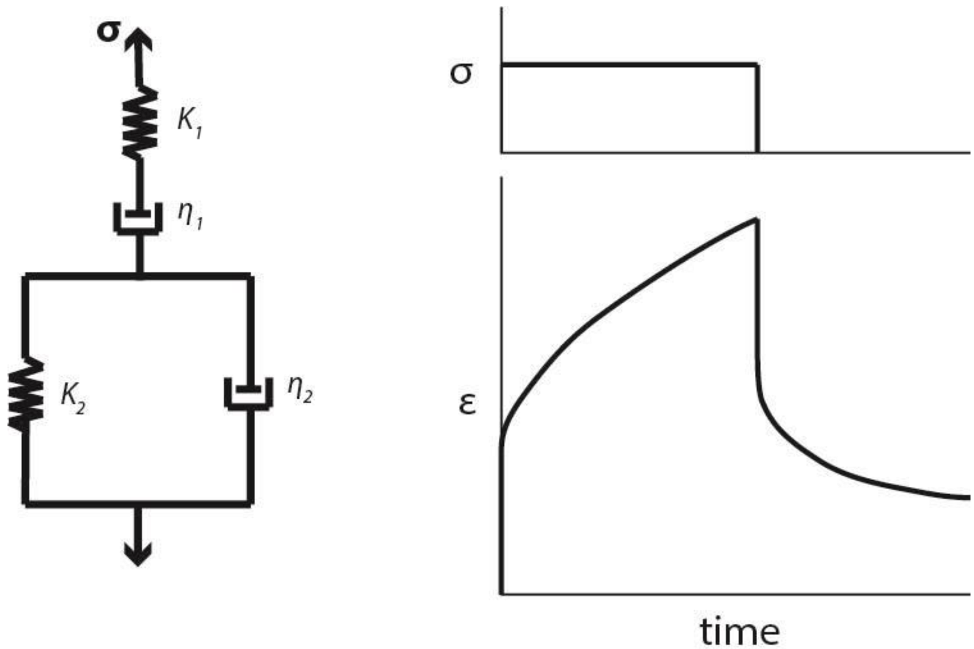

Figure 4: Illustration of the Burgers solid (left), which represents the viscoelastic properties of materials as a combination of springs and dashpots. The spring K_1 models the elastic modulus of the material, the dashpot with viscosity η_I represents steady-state creep, and the (mechanically) parallel spring (K_2) and dashpot (η_2) model transient creep and anelasticity. The time-dependent strain accrued by a Burgers solid subjected to constant stress (creep) is shown at right. At time $t > 0$, the anelastic element produces a decelerating creep transient leading to steady-state deformation with viscosity η_1. Upon removal of the stress, elastic recovery due to K_1 is followed by time-dependent recovery due to the anelastic element.

Inserted into the compliance function, the Andrade model yields:

$$J(t) = J_U + \beta t^{\psi} + \frac{t}{\eta_{SS}} \qquad [11]$$

When a sinusoidal, time-varying load is applied, the compliance becomes a complex function.

$$J^* = J_1(\omega) - iJ_2(\omega) \qquad [12]$$

where J_1 is the storage compliance, J_2 is the "loss compliance," and ω is the angular frequency (rad/s; ω=2π*f*). The storage and loss compliance of the Andrade model formulation are, respectively (McCarthy & Cooper, 2016),

$$J_1 = J_U + \beta\Gamma(1+\psi)\omega^{-\psi}\cos\left(\frac{\psi\pi}{2}\right) \text{, and} \qquad [13]$$

$$J_2 = \beta\Gamma(1+\psi)\omega^{-\psi}\sin\left(\frac{\psi\pi}{2}\right) + \frac{1}{\eta_{SS}\omega}. \qquad [14]$$

It should be noted that η_{ss} in Eq. 14 *is that of the relaxation mechanism*; if a sinusoidal stress perturbation overlies a background stress, the viscosity relevant to attenuation need not be the same as the creep viscosity effecting background deformation. From complex analysis, one can then calculate that attenuation is the ratio of the two components of the complex compliance (Nowick & Berry, 1972):

$$Q^{-1} = \frac{1}{2\pi}\frac{J_2}{J_1} \qquad [15]$$

4.2. The Andrade Model and the High-Temperature Background

Plotting Q^{-1} vs f according to Eqs. (13)-(15) produces a spectrum such as that shown schematically in Fig. 5a. This broad attenuation spectrum, where $Q^{-1} \propto f^{-\varphi}$ ($0 < \varphi \leq 0.5$) is known as the "high-temperature background" and has been robustly observed

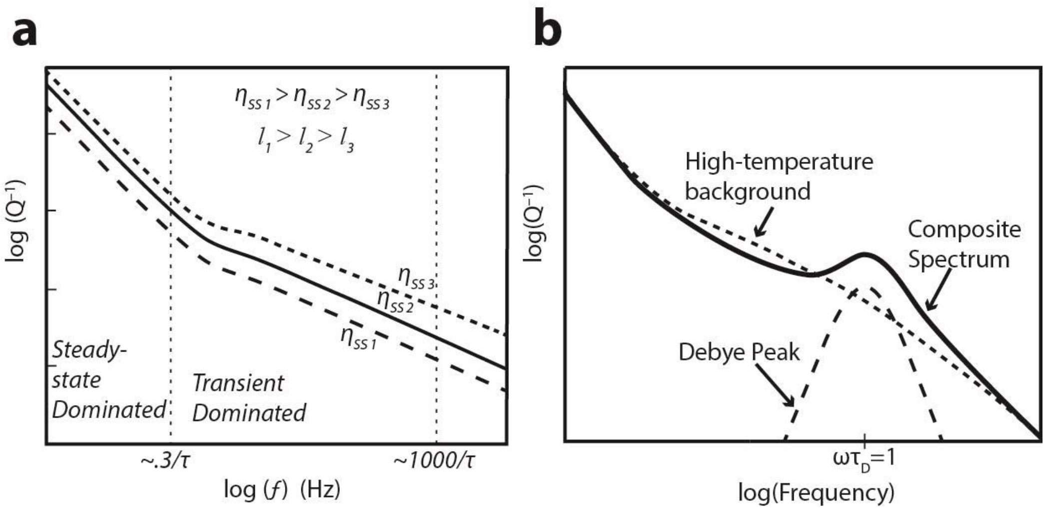

Figure 5: (a) The high temperature background attenuation spectrum, modeled by transformation of the Andrade model of viscoelastic rheology. Near-steady-state flow dominates the response at low frequencies (< ~0.3τ, where τ is the characteristic time of the diffusion-effected evolution of grain boundary tractions), while transient flow dominates at high frequencies. The physical foundation of the model, which fits real data well, is the physics of diffusion creep(Gribb & Cooper, 1998). The spectrum shifts to higher frequency when the steady-state diffusion creep viscosity decreases, e.g., by an increase in temperature and/or a decrease in grain size. (b) The effect of a superimposed Debye-type peak onto the attenuation spectrum. The peak arises from a singular exponential decay mechanism with a characteristic relaxation time, τ_D, is approximately one decade of frequency wide, and is centered around $\omega\tau_D$.

by many authors for a variety of materials (e.g., Faul & Jackson, 2005; Gribb & Cooper, 1998; McCarthy et al., 2011; McMillan et al., 2003). The excellent agreement between the high-temperature background and the Andrade model indicates that the physical basis for the high-temperature background is the same as that for transient diffusion creep: chemical diffusion in the context of a diminishing potential.

Gribb & Cooper (1998) extended their analysis of the Andrade model to address the physical basis of the high-temperature background. After parameterizing the Andrade model based on the measured creep response of their olivine aggregates, they then measured attenuation in the same material and compared the Andrade model inversion (e.g. Eq's 13-15) to the measured attenuation. The Andrade model inversions – parameterized solely via the diffusion creep experiments – fit the attenuation data well, anchoring the physics of the high temperature background in the diffusional evolution of tractions on grain boundaries (Gribb & Cooper, 1998; Raj & Ashby, 1971; Raj, 1975).

The critical implication is that the high-temperature background has, at its heart, the process of chemical diffusion in the context of a diminishing potential. Scaling of the high-temperature background is therefore governed by the characteristic timescale of the diffusional process, τ (in a creep test, the strain rate decays to within ~1% of steady state by 0.25τ). This time scale is a function of diffusion kinetics (Cooper, 2002; Gribb & Cooper, 1998; Rishi Raj, 1975):

$$\tau = \frac{3\sqrt{3}\left(1-\nu^2\right)l^3 kT}{2\pi^3 Y D_b \delta\Omega} \qquad [16]$$

where l is the length scale of diffusion, D_b is the grain boundary diffusivity ($D_b = D_o$exp(-E/RT), δ is the grain boundary width, and Ω is the atomic volume of the diffusing species.

Equation (16) assumes boundary diffusion and thus $\tau \propto l^3$ (Coble, 1963; Raj, 1975). For volume diffusion, $\tau \propto l^2$ (Herring, 1950; Nabarro, 1948; Raj, 1975). For a material deforming via diffusion creep (for which $l = d$), modifying the length scale modifies both the relaxation timescale and the steady-state viscosity (Eq. 4), which shifts the attenuation spectrum in frequency space (dashed and dotted lines, Fig. 5a).

The criticality of l in Eq. (16) means that extrapolation of laboratory attenuation data to geophysical settings requires robust identification of the proper length scale (Abers et al., 2014; Cooper, 2002; Nowick & Berry, 1972). Gribb & Cooper (1998) noted that extrapolation based on grain size did not adequately match geophysical data, and suggested that in a deforming material (such as olivine in the Earth's mantle) the proper length scale may be the stress-effected subgrain size. Numerous studies have focused on diffusion creep as a grain size-sensitive process and attempted to parameterize the frequency shift of Q^{-1} solely in terms of grain size and/or temperature (e.g., Faul & Jackson, 2005) – as will be described in the next section, however, the work of McCarthy & Cooper (2016) suggested that for ice, at least, the high-temperature background behavior is insensitive to grain size. Chapter 4 addresses the question of attenuation in polycrystalline ice through improved measurements.

4.3. Other Mechanisms of Attenuation

The evolution of chemical potential gradients on grain boundaries is not the only source of attenuation in crystalline solids. The high temperature background is so-called because it was often subtracted from attenuation data sets to isolate specific peaks in Q^{-1}. In frequency space these are called "Debye peaks." These peaks, superimposed on the high-temperature background, are indicative of singular mechanisms of exponential decay with distinct relaxation times, $\tau_D = \eta/Y$, where η is the viscosity of the relaxation mechanism (Cooper, 2002; Nowick & Berry, 1972). They are approximately one decade of frequency in width, centered around $\omega\tau_D$ (Fig 4b). Among many physical processes that can produce discrete peaks, some of the most notable are the Snoek and Zener relaxations, due to the rearrangement of interstitial and/or substitutional solute atoms under deviatoric stress (Nowick & Berry, 1972; Snoek, 1941; Zener, 1947), and the "vibrating string" model of dislocation vibration (Granato & Lücke, 1956; Nowick & Berry, 1972). In ice specifically, a discrete peak is observed at high frequencies (~100-1000 Hz) due to the rearrangement of protons within the ice lattice (Kuroiwa, 1964a).

At lower frequencies ($\leq$ 10Hz), a peak attributed to elastically-accommodated grain boundary sliding may appear (Benoit, 2004; Kê, 1947, 1999; Nowick & Berry, 1972; Sundberg & Cooper, 2010). There remains ongoing debate regarding the relative contributions of grain boundaries and lattice dislocations in the relaxation process responsible for this peak – partly due to the measurement of similar peaks in single-crystal materials (Belamri et al., 2006; Benoit, 2004; Ke, 1999; Nowick & Berry, 1972) – although diffusion along subgrain boundaries in polygonized samples has been suggested to explain the presence of such a peak in deformed single crystals (Gribb & Cooper, 1998; McCarthy & Cooper, 2016).

The simultaneous presence of the high-temperature background and discrete peaks associated with specific relaxation mechanisms results in a composite attenuation spectrum (Fig. 4b). When a specific mechanism for the peak can be identified, the relaxation time and strength can be calculated; a composite spectrum can then be modeled as the superposition of the peak onto the high-temperature background (e.g., Sundberg & Cooper, 2010).

4.4. Attenuation in Ice

The work in Chapter 4 builds on a foundation of several studies of attenuation in water ice. In addition to the study of proton movement described above (Kuroiwa, 1964a), the same lab specifically investigated attenuation due to grain boundary processes in ice (Kuroiwa, 1964b) by varying the grain boundary area within polycrystalline samples welded between two single crystals. The measured dissipation was not consistently affected by the area of grain boundaries present in the sample; Kuroiwa hypothesized that the first-order factor in determining the relaxation time of the specimen was, instead, segregation of impurities to the grain boundary. However, the work was conducted at high frequency (177-790 Hz) and the authors did not observe a discrete peak.

Tatibouet et al. (1987) sought to measure the grain boundary peak at lower temperatures (200-273K) and frequencies (1-10^{-3} Hz) than those explored by Kuroiwa (1964b). These authors observed a clear peak in attenuation in Q^{-1} vs. T space that shifted toward lower temperatures at lower frequencies. The presence of the peak was strongly influenced by deformation; when the same bicrystal was plastically deformed to 1% strain, the magnitude of attenuation increased by a factor of 2-3 and a distinct peak was no longer observed. The peak was recovered, however, by annealing the sample. By comparison, deformation of a single crystal did *not* produce a peak, even when the sample was polygonized. Thus, Tatibouet et al. credited the observed peak to the presence of high-angle grain boundaries (Tatibouet et al., 1987).

Most recently, McCarthy & Cooper (2016) measured attenuation in creeping polycrystalline ice by subjecting their specimens to sinusoidally-varying compressive stress while they were simultaneously creeping under a background, compressive stress. McCarthy & Cooper observed that a) the ice was approximately an order of magnitude more attenuating than would be expected from inversion of the Andrade model, b) the attenuation spectrum was insensitive to grain size, and c) the attenuation response was modestly nonlinear. The results suggested that in the GBS regime, the length scale of dissipation may instead be the stress-sensitive subgrain size within the ice; their data collapsed onto the form of the Andrade model inversion when the spectra were normalized to the Maxwell frequency for diffusion creep of a subgrain network with average spacing of 20 μm. Their work implied that for ice creeping in the GBS regime, stress-sensitive microstructural features – rather than grain size – may be the appropriate length scale upon which to base predictions of Q^{-1} (Gribb & Cooper, 1998; McCarthy & Cooper, 2016). The work explored only one creep stress, however, and a constitutive relationship between stress and Q^{-1} could therefore not be determined. Chapter 4 addresses the hypothesis that a stress-sensitive length scale underpins attenuation in creeping polycrystalline ice, and addresses the convolution of the high-temperature background with a grain boundary peak in the frequency range studied.

Abers, G. A., Fischer, K. M., Hirth, G., Wiens, D. A., Plank, T., Holtzman, B. K., … Gazel, E. (2014). Reconciling mantle attenuation-temperature relationships from seismology, petrology, and laboratory measurements. *Geochemistry, Geophysics, Geosystems*, *15*(9), 3521–3542. https://doi.org/10.1002/2014GC005444

Andrade, E. da C. (1910). On the viscous flow in metals, and allied phenomena. *Proceedings of the Royal Society of London. Series A, Containing Papers of a Mathematical and Physical Character*, 1–12.

Ashby, M. F. (1972). Boundary defects, and atomistic aspects of boundary sliding and diffusional creep. *Surface Science*, *31*, 498–542.

Ashby, M. F., & Verrall, R. A. (1973). Diffusion-accommodated flow and superplasticity. *Acta Metallurgica*, *21*, 149–163.

Ball, A., & Hutchison, M. M. (1969). Superplasticity in the aluminum-zinc eutectoid. *Metal Science Journal*, *3*(1), 1–7.

Baluffi, R. W., Brokman, A., & King, A. H. (1982). CSL/DSL Lattice model for general crystal/crystal boundaries and their line defects. *Acta Metallurgica*, *30*(8), 1453–1470.

Barr, A. C., & Pappalardo, R. T. (2005). Onset of convection in the icy Galilean satellites: Influence of rheology. *Journal of Geophysical Research*, *110*(E12). https://doi.org/10.1029/2004JE002371

Belamri, C., Belhas, S., & Rivière, A. (2006). Damping of a high-purity aluminum single crystal at high temperatures. *Materials Science and Engineering: A*, *442*(1–2), 142–146. https://doi.org/10.1016/j.msea.2006.05.167

Benoit, W. (2004). High-temperature relaxations. *Materials Science and Engineering: A*, *370*(1–2), 12–20. https://doi.org/10.1016/j.msea.2003.08.068

Bunton, J. H. (2001). *The Impact of Grain Size on the Shear Creep and Attenuation Behavior of Polycrysalline Olivine* (M.Sc.). Brown University, Providence, RI.

Cassen, P., Reynolds, T., & Peale, S. J. (1979). Is there liquid water on Europa? *Geophysical Research Letters*, *6*(9), 731–734.

Caswell, T. E., Cooper, R. F., & Goldsby, D. L. (2015). The constant-hardness creep compliance of polycrystalline ice. *Geophysical Research Letters*, *42*. https://doi.org/10.1002/2015GL064666

Coble, R. L. (1963). A model for boundary diffusion controlled creep in polycrystalline materials. *Journal of Applied Physics*, *34*(6), 1679–1682.

Collins, G. C., McKinnon, W. B., Moore, J. M., Nimmo, F., Pappalardo, R. T., Prockter, L. M., & Schenk, P. M. (2009). Tectonics of the outer planet satellites. *Planetary Tectonics*, *11*, 264.

Consolmagno, G. J., & Lewis, J. S. (1976). Structural and thermal models of icy Galilean satellites. In *Jupiter: Studies of the interior, atmosphere, magnetosphere and satellites* (pp. 1035–1051). Tucson, Ariz.: University of Arizona Press.

Cooper, R. F. (2002). Seismic wave attenuation: energy dissipation in viscoelastic crystalline solids. *Reviews in Mineralogy and Geochemistry*, *51*(1), 253–290.

Cuffey, K. M., Thorsteinsson, T., & Waddington, E. D. (2000). A renewed argument for crystal size control of ice sheet strain rates. *Journal of Geophysical Research*, *105*(B12), 27889–27894.

Cuffey, Kurt M., & Paterson, W. S. B. (2010). *The Physics of Glaciers* (4th ed.). Burlington, MA: Elsevier, Inc.

Druetta, E., Nasello, O. B., & Prinzio, C. L. D. (2013). Experimental Determination of /phi Tilt Grain Boundary Energies in Ice. *Journal of Materials Science Research*, *3*(1). https://doi.org/10.5539/jmsr.v3n1p69

Durham, W. B., Prieto-Ballesteros, O., Goldsby, D. L., & Kargel, J. S. (2010). Rheological and Thermal Properties of Icy Materials. *Space Science Reviews*, *153*(1–4), 273–298. https://doi.org/10.1007/s11214-009-9619-1

Durham, William B., Stern, L. A., & Kirby, S. H. (2001). Rheology of ice I at low stress and elevated confining pressure. *Journal of Geophysical Research*, *106*(6), 11031–11042.

Duval, P. (1978). Anelastic Behaviour of Polycrystalline Ice. *Journal of Glaciology*, *21*(85), 621–628. https://doi.org/10.3189/S0022143000033736

Faul, U. H., & Jackson, I. (2005). The seismological signature of temperature and grain size variations in the upper mantle. *Earth and Planetary Science Letters*, *234*(1), 119–134.

Findley, W. N., Lai, J. S., & Onaran, K. (1976). *Creep and Relaxation of Nonlinear Viscoelastic Materials*. New York: Dover Publications.

Frost, H. J., & Ashby, M. F. (1982). *Deformation-Mechanism Maprs, the Plasticity and Creep of Metals and Ceramics*. Pergamon press.

Fukuda, A., Hondoh, T., & Higashi, A. (1987). DISLOCATION MECHANISMS OF PLASTIC DEFORMATION OF ICE. *Le Journal de Physique Colloques*, *48*(C1), C1-163-C1-173. https://doi.org/10.1051/jphyscol:1987124

Glen, J. W. (1955). The creep of polycrystalline ice. In *Proceedings of the Royal Society of London A: Mathematical, Physical and Engineering Sciences* (Vol. 228, pp. 519–538). The Royal Society. Retrieved from http://rspa.royalsocietypublishing.org/content/228/1175/519.short

Goldsby, D. L., & Kohlstedt, D. L. (1997). Grain boundary sliding in fine-grained ice I. *Scripta Materialia*, *37*(9), 1399–1406.

Goldsby, D. L., & Kohlstedt, D. L. (2001). Superplastic deformation of ice: Experimental observations. *Journal of Geophysical Research*, *106*(B6), 11017–11030.

Granato, A., & Lücke, K. (1956). Application of Dislocation Theory to Internal Friction Phenomena at High Frequencies. *Journal of Applied Physics*, *27*(7), 789–805. https://doi.org/10.1063/1.1722485

Greeley, R., Sullivan, R., Klemaszewski, J., Homan, K., Veverka, J., Clark, B., … Pappalardo, R. T. (1998). Europa: Initial Galileo Geological Observations. *Icarus*, *135*, 4–24.

Greenberg, R., Geissler, P., Hoppa, G., Tufts, B. R., Durda, D., Pappalardo, R. T., … Carr, M. H. (1998). Tectonic Processes on Europa: Tidal Stresses, Mechanical Response, and Visible Features. *Icarus*, *135*, 64–78.

Gribb, T. T., & Cooper, R. F. (1998). Low-frequency shear attenuation in polycrystalline olivine: Grain boundary diffusion and the physical significance of the Andrade model for viscoelastic rheology. *Journal of Geophysical Research*, *103*(B11), 27267–27279.

Hammond, N. P., & Barr, A. C. (2014). Global resurfacing of Uranus’s moon Miranda by convection. *Geology*, *42*(11), 931–934. https://doi.org/10.1130/G36124.1

Helfenstein, P., & Parmentier, E. M. (1985). Patterns of fracture and tidal stresses due to nonsynchronous rotation: Implications for fracturing on Europa. *Icarus*, *61*(2), 175–184.

Herring, C. (1950). Diffusional Viscosity of a Polycrystalline Solid. *Journal of Applied Physics*, *21*(5), 437–445. https://doi.org/10.1063/1.1699681

Hirth, J. P. (1972). The Influence of Grain Boundaries on Mechanical Properties. *Metallurgical Transactions*, *3*, 3047–3067.

Hondoh, T., & Higashi, A. (1978). X-ray diffraction topographic observations of the large-angle grain boundary in ice under deformation. *Journal of Glaciology*, *21*(85), 629–638.

Hondoh, Takeo, & Higashi, A. (1983). Generation and absorption of dislocations at large-angle grain boundaries in deformed ice crystals. *The Journal of Physical Chemistry*, *87*(21), 4044–4050.

Ke, T. S. (1947). Experimental evidence of the viscous behavior of grain boundaries in metals. *Physical Review*, *71*(8), 533–546.

Ke, T. S. (1999). Fifty-Year Study of Grain-Boundary Relaxation. *Metallurgical and Materials Transactions A*, *30A*, 2267–2295.

Ketcham, W. M., & Hobbs, P. V. (1969). An Experimental Determination of the Surface Energies of Ice. *Philosophical Magazine*, *19*, 1161–1173.

Khurana, K. K., Kivelson, M. G., Stevenson, D. J., Schubert, G., Russell, C. T., Walker, R. J., & Polanskey, C. (1998). Induced magnetic fields as evidence for subsurface oceans in Europa and Callisto. *Nature*, *395*.

Kuroiwa, D. (1964a). Internal Friction of Ice. Ⅰ; The Internal Friction of H2O and D2O Ice, and the Influence of Chemical Impurities on Mechanical Damping. *Contributions from the Institute of Low Temperature Science*, *18*, 1–37.

Kuroiwa, D. (1964b). Internal Friction of Ice. Ⅱ; The Grain Boundary Internal Friction of Ice. *Contributions from the Institute of Low Temperature Science*, *18,* 38–48.

Lakes, R. S. (1998). *Viscoelastic Solids* (Vol. 9). CRC Press.

Langdon, T. G. (1991). The physics of superplastic deformation. *Materials Science and Engineering*, *A137*, 1–11.

McCarthy, C., & Cooper, R. F. (2016). Tidal dissipation in creeping ice and the thermal evolution of Europa. *Earth and Planetary Science Letters*, *443,* 185–194. https://doi.org/10.1016/j.epsl.2016.03.006

McCarthy, C., Takei, Y., & Hiraga, T. (2011). Experimental study of attenuation and dispersion over a broad frequency range: 2. The universal scaling of polycrystalline materials. *Journal of Geophysical Research*, *116*(B9). https://doi.org/10.1029/2011JB008384

McMillan, K. M., Lakes, R. S., Cooper, R. F., & Lee, T. (2003). The viscoelastic behavior of β-In 3 Sn and the nature of the high-temperature background. *Journal of Materials Science*, *38*(12), 2747–2754.

Montagnat, M., & Duval, P. (2000). Rate controlling processes in the creep of polar ice, influence of grain boundary migration associated with recrystallization. *Earth and Planetary Science Letters*, *183*(1), 179–186.

Moore, W., & Schubert, G. (2000). The Tidal Response of Europa. *Icarus*, *147*(1), 317–319. https://doi.org/10.1006/icar.2000.6460

Nabarro, F. R. N. (1948). Deformation of crystals by the motion of single ions. In *Report of a Conference on Strength of Solids* (pp. 75–90).

Nimmo, F., Porco, C., & Mitchell, C. (2014). TIDALLY MODULATED ERUPTIONS ON ENCELADUS: *CASSINI* ISS OBSERVATIONS AND MODELS. *The Astronomical Journal*, *148*(3), 46. https://doi.org/10.1088/0004-6256/148/3/46

Nowick, A. S., & Berry, B. S. (1972). *Anelastic Relaxation in Crystalline Solids*. New York: Academic Press.

Ojakangas, G. W., & Stevenson, D. J. (1989). Thermal state of an ice shell on Europa. *Icarus*, *81*(2), 220–241.

Pappalardo, R. T., & Barr, A. C. (2004). The origin of domes on Europa: The role of thermally induced compositional diapirism. *Geophysical Research Letters*, *31*(1). https://doi.org/10.1029/2003GL019202

Pappalardo, R. T., Head, J. W., Greeley, R., Sullivan, R., Pilcher, C., Schubert, G., … Goldsby, D. L. (1998). Geological evidence for solid-state convection in Europa's ice shell. *Nature*, *391*. Retrieved from http://www.planetary.brown.edu/pdfs/1874.pdf

Pappalardo, R. T., Reynolds, S., & Greeley, R. (1997). Extensional tilt blocks on Miranda: Evidence for an upwelling origin of Arden Corona. *Journal of Geophysical Research*, *102*(E6), 13369–13379.

Paterson, W. S. B. (1991). Why ice-age ice is sometimes "soft." *Cold Regions Science and Technology*, *20*(1), 75–98.

Piazolo, S., Wilson, C. J. L., Luzin, V., Brouzet, C., & Peternell, M. (2013). Dynamics of ice mass deformation: Linking processes to rheology, texture, and microstructure:

Dynamics of Ice Mass Deformation. *Geochemistry, Geophysics, Geosystems*, *14*(10), 4185–4194. https://doi.org/10.1002/ggge.20246

Poirier, J.-P. (1985). *Creep of Crystals*. Cambridge University Press.

Porco, C. C., Helfenstein, P., Thomas, P. C., Ingersoll, A. P., Wisdom, J., West, R., … others. (2006). Cassini observes the active south pole of Enceladus. *Science*, *311*(5766), 1393–1401.

Raj, R., & Ashby, M. F. (1971). On Grain Boundary Sliding and Diffusional Creep. *Metallurgical Transactions*, *2*, 1113–1127.

Raj, Rishi. (1975). Transient behavior of diffusion-induced creep and creep rupture. *Metallurgical and Materials Transactions A*, *6*(8), 1499–1509.

Ramseier, R. O. (1967). Self-Diffusion of Tritium in Natural and Synthetic Ice Monocrystals. *Journal of Applied Physics*, *38*(6), 2553–2556. https://doi.org/10.1063/1.1709948

Readey, D. W., & Kingery, W. D. (1964). Plastic deformation of single crystal ice. *Acta Metallurgica*, *12*, 171–178.

Reynolds, T., & Cassen, P. (1979). On the internal structure of the major satellites of the outer planets. *Geophysical Research Letters*, *6*(2), 121–124.

Roberts, J. H., & Nimmo, F. (2008). Tidal heating and the long-term stability of a subsurface ocean on Enceladus. *Icarus*, *194*(2), 675–689. https://doi.org/10.1016/j.icarus.2007.11.010

Schenk, P. M., & Zahnle, K. (2007). On the negligible surface age of Triton. *Icarus*, *192*(1), 135–149. https://doi.org/10.1016/j.icarus.2007.07.004

Snoek, J. L. (1941). Effect of small quantities of carbon and nitrogen on the elastic properties of iron. *Physica*, *8*(7), 711–733.

Sundberg, M., & Cooper, R. F. (2010). A composite viscoelastic model for incorporating grain boundary sliding and transient diffusion creep; correlating creep and attenuation responses for materials with a fine grain size. *Philosophical Magazine*, *90*(20), 2817–2840. https://doi.org/10.1080/14786431003746656

Sutton, A. P., & Balluffi, R. W. (1995). *Interfaces in Crystalline Materials*. Oxford University Press.

Tatibouet, J., Perez, J., & Vassoille, R. (1987). STUDY OF GRAIN BOUNDARIES IN ICE BY INTERNAL FRICTION MEASUREMENT. *Le Journal de Physique Colloques*, *48*(C1), C1-197-C1-203. https://doi.org/10.1051/jphyscol:1987128

Thomas, P. C., Tajeddine, R., Tiscareno, M. S., Burns, J. A., Joseph, J., Loredo, T. J., … Porco, C. (2016). Enceladus's measured physical libration requires a global subsurface ocean. *Icarus*, *264*, 37–47. https://doi.org/10.1016/j.icarus.2015.08.037

Waite Jr, J. H., Lewis, W. S., Magee, B. A., Lunine, J. I., McKinnon, W. B., Glein, C. R., … Ip, W.-H. (2009). Liquid water on Enceladus from observations of ammonia and 40Ar in the plume. *Nature*, *460*(7254), 487–490. https://doi.org/10.1038/nature08153

Wilson, C. J. L., & Peternell, M. (2012). Ice deformfed in compresison and simple shear: control of temeprature and initial fabric. *Journal of Glaciology*, *58*(207), 11–22. https://doi.org/10.3189/2012JoG11J065

Zener, C. (1947). Stress induced preferential orientation of pairs of solute atoms in metallic solid solution. *Physical Review*, *71*(1), 34.

Chapter 2 | The Constant-hardness Creep Compliance of Polycrystalline Ice

Tess E. Caswell[1], Reid F. Cooper[1], and David L. Goldsby[2]

[1]Brown University, Providence, Rhode Island, 02912, USA

[2]University of Pennsylvania, Philadelphia, Pennsylvania, 19104, USA

Abstract

We have performed creep and stress-reduction experiments on polycrystalline ice (grain sizes, $d \approx 30$ and ≈ 245 μm) in the grain boundary sliding and dislocation creep regimes (stresses σ = 0.5–5 MPa, temperature T = 233 K), to determine the constant-hardness creep compliance under these conditions. Our results are consistent with a microstructural state-variable description of dislocation-effected deformation whose rate is accelerated by grain boundary sliding. The fine-grained specimens reveal no subgrain boundaries, indicating that the stress-sensitive microstructural feature upon which the state-variable behavior is founded may be the dislocation structure of the grain boundaries. Deviations of our constant-hardness data from the behavior predicted by the state-variable formulation allow estimation of the viscosity of the grain boundaries, which is ~4.8×10^6 Pa·s at this temperature.

1. Introduction

Modeling the rheological behavior of glaciers, ice sheets, and interiors of icy moons requires an understanding of the interactions between mechanical processes that occur on multiple timescales. Stresses imposed (or relieved) by relatively rapid and transient events such as calving, crevasse formation, or tidal dissipation occur in the context of a material flowing nominally at a steady state, with a microstructure set and sustained by the long-term, persistent stress state. Changes in stress induced by short-timescale events are imposed upon this microstructure. Full understanding of the material's response to such transient events requires knowledge of the microstructure established over long timescales and the response of that microstructure to a changing stress state.

Hart (1970) postulated that for a material deforming plastically via dislocation creep, deformation-induced microstructure (that is, microstructure that is sensitive to the deviatoric stress and established by a minimum amount of finite strain) can be quantified by a single state variable that he termed the “hardness.” Experimentally, hardness is determined by measuring strain rate vs. stress (the creep compliance) at nominally constant strain (Korhonen et al., 1987). Stone et al. (2004) argued that a single hardness parameter can describe the distributions of mobile lattice defects at all length scales in the material only if those distributions are self-similar, meaning that the statistical distribution of defect spacing is similar at all length scales (cf. Weertman & Weertman, 1983); using this understanding they characterized the hardness in single-crystal halite based upon a single, representative statistical distribution: that of subgrain size.

Stress-reduction experiments provide data describing a material’s hardness. In these experiments, specimens reach steady-state creep under constant stress, at which point the applied stress is instantaneously reduced to induce a transient response related directly to the earlier-established steady-state microstructure. The results of such experiments, quantitatively equivalent to those produced by stress-relaxation tests, map out constant-hardness creep compliance in stress-strain rate space (Korhonen et al., 1985). For a material deforming via dislocation creep, this constant-hardness compliance is described by the “lambda law:”

$$\ln(\sigma^* / \sigma) = (\dot{\varepsilon}^* / \dot{\varepsilon})^{\lambda}, \tag{1}$$

where σ is stress, $\dot{\varepsilon}$ is strain rate, σ* is the hardness parameter, $\dot{\varepsilon}^*$ is the corresponding strain rate parameter (the strain rate at which stress falls to σ^*/e), and λ (≈ 0.15) is a shape factor describing the curve (Hart, 1970; Jackson et al., 1981; Alexopoulos et al., 1982). Constant-hardness compliance deviates from the lambda law when grain boundary sliding (GBS) contributes to the relaxation response (Alexopoulos et al., 1982). When grains are free to slide, GBS leads to stress concentrations at grain junctions, which subsequently cause accelerated flow in grain interiors; this enhances the macroscopic creep rate at low stresses (Crossman and Ashby, 1975).

Many readers will be familiar with a power-law flow law for steady state, i.e., $\dot{\varepsilon} \propto \sigma^n$, in which the stress exponent *n* reflects scaling of strain rate with stress. Because steady-state microstructure is established by stress, "traversing" the flow law through changes in stress implies corresponding changes in microstructure. The lambda law, however, represents the response of a single microstructure to variations in stress (Hart, 1970). Analogous to the stress exponent in this case is the scaling slope between constant-hardness curves, which is related to the evolution of the hardness parameter σ* with stress [the reader is encouraged to consult Stone et al. (2004) for a comprehensive treatment of the relationship between σ* and microstructure].

Here we present constant-hardness creep compliance data, gathered via stress reduction experiments, for polycrystalline ice (hexagonal; polymorph Ih) initially flowing at steady state in the grain boundary sliding and dislocation creep regimes characterized by Goldsby & Kohlstedt (2001). Because basal dislocation glide occurs at extremely low stresses in ice, the GBS rheology involves a serial process of (i) sliding on grain boundaries and (ii) the glide of basal dislocations in the adjacent grains (thus, GBS is a non-Newtonian mechanism, affected—and effected—by the motion of lattice dislocations). We show that even under conditions where GBS is rate-limiting, stress-reduction experiments describe a constant-hardness compliance distribution consistent with Hart's equation of state, which suggests a self-similar defect microstructure created by the flow stress. The mechanical data, however, exhibit similar behavior whether or not subgrain boundaries form during deformation. These results suggest that hardness in the GBS regime is set by the defect structure of the grain boundaries.

2. Experimental Approach

2.1 Specimen Fabrication and Mechanical Testing

Polycrystalline ice samples were manufactured via two methods. Fine-grained samples (mean grain size, $d \approx 30$ μm) were hot pressed from fine-grained powder by the method of Goldsby & Kohlstedt (1997). Coarse-grained samples ($d \approx 245$ μm) were prepared by flooding packed cylinders of coarsely ground ice with degassed, deionized water at 0°C, then slowly refreezing [the "standard ice" of Stern et al. (1997)].

Experiments were conducted in compression in a uniaxial, ambient-pressure, dead-weight creep apparatus [described in Goldsby & Kohlstedt (1997)], which includes an ethanol-bath cryostat that controls sample temperature to a precision of +0.5/−1.0 K. Our experiments were performed at 233 K (−40 ºC). Strain and strain rate in the sample were determined by measuring the distance between two ceramic plates abutting the sample (via a voltage-displacement-transducer—DCDT—extensometer); strain resolution, accounting for analog-to-digital conversion during data acquisition, was $\sim 10^{-6}$. Load was controlled by weights hung from a lever. Constant stress was maintained by incremental addition of weight to the lever as creep progressed (every ~0.5% strain), assuming constant volume of a cylindrical sample. Stress reductions were accomplished by removing partial weight from the lever.

Samples were transferred from storage in dry ice at 195 K (−78° C) into the apparatus at 193K (−80° C). The cryostat was then passively warmed to 233 K over the course of 12-18 h, and the sample allowed to thermally equilibrate for 24 h prior to each experiment.

Stress-reduction experiments followed the methodology of Korhonen et al. (1985). Samples achieved steady-state creep (verified by monitoring strain rate vs. strain) before partial weight was lifted from the lever, instantly reducing the stress on the sample. A series of transients followed each stress reduction, observable in the displacement data (Fig. 1). Elastic recovery occurs immediately, followed by partial anelastic recovery (segment (2) in Fig. 1), which for flow accomplished all or in part by dislocation motion is attributed primarily to the rapid relaxation of mobile dislocations from pileups, e.g., at grain or subgrain boundaries, established at the higher stress. A brief period of low strain rate follows (segment (3)), after which strain rate accelerates as the less-mobile aspects of the dislocation microstructure, i.e., those giving rise to the hardness σ* evolve toward steady state at the new, lower stress (segment (4)). Individual samples were cycled through multiple reductions in stress; following observation of a stress-reduction and low-strain-rate transient, samples were reloaded to the initial, higher stress, the steady state reestablished and another stress-reduction performed to a different reduced stress. Individual samples experienced a maximum of four such steps of stress reduction.

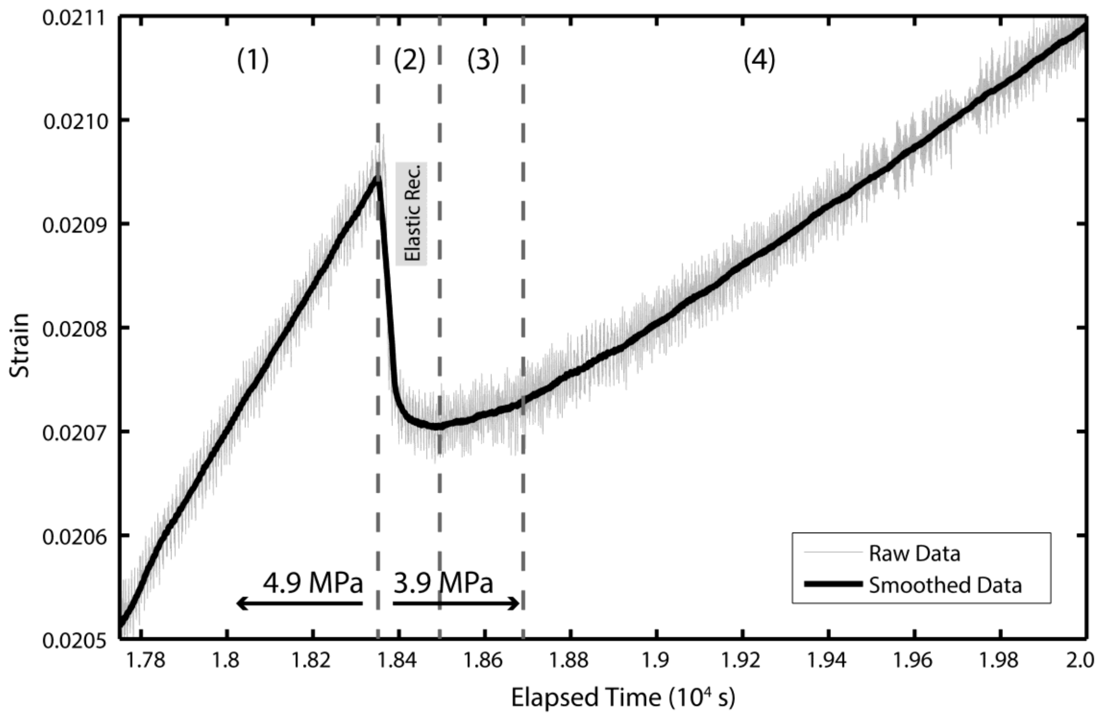

Figure 1: Example of transient flow wrought by stress reduction. The segments labeled are: (1) steady-state creep, (2) elastic and anelastic recovery, the latter wrought by the relaxation of "free" (i.e., mobile) dislocations, e.g., from pileups, (3) the isostructural period, where strain rate reflects the flow response of the rate-limiting microstructure that was established at the previous, higher stress (4.9 MPa) to the new, reduced stress (3.9 MPa), and (4) evolution toward steady-state creep corresponding to the new, reduced stress. The magnitude of elastic recovery in segment (2), which is $\sim 10^{-4}$ for the stress drop shown, is indicated by the gray bar in the figure. The experimental data are smoothed over a 40-s interval.

In the low-strain-rate period (segment (3) in Fig. 1), $\Delta\varepsilon \approx 10^{-5}$. Such strain is insufficient for stress-sensitive, extended-scale dislocation structures (that is, ordered structures created by organization of many dislocations) to evolve into equilibrium with the new applied stress [which requires $\Delta\varepsilon \geq 1\%$, cf. Hamann et al. (2007)]; thus, hardness is unchanged from that established in the steady-state flow prior to the stress reduction. The strain rate in segment (3) therefore reflects the effective viscosity of the initial microstructure, established in steady-state creep at the previous, higher stress, at the new, reduced stress (Korhonen et al., 1985). A series of stress reductions to a range of lower stresses, each from the same initial steady state, therefore maps out the constant-hardness creep compliance of a specimen in stress-strain rate space.

2.2 Microstructure Analysis

Microstructural analyses were performed on experimental specimens and starting material via a combination of reflected-light optical microscopy and cryogenic electron backscatter diffraction (EBSD). The analyses were performed several weeks after completion of the mechanical experiments; as such, all specimens were stored in a cryogenic dewar at 77 K (-196 °C) between experiments and analysis to preserve microstructure.

EBSD was performed on a Zeiss Sigma field-emission scanning electron microscope at the Otago Center for Electron Microscopy (University of Otago, Dunedin, New Zealand) (Piazolo et al., 2008; Prior et al., 2015). Sections for analysis were cut from experimental specimens using a band saw and bonded to copper SEM adapters by a very thin (~100 μm) melt layer, which forms a strong bond while maintaining sample temperature below 223 K (–50 °C). The sample surface was then shaved flat in a cryogenic microtome at 243 K (−30 °C) before insertion into the SEM.

Samples were prepared for optical microscopy by cutting a flat surface with a microtome, then allowing the shaved surface to sublimate in air for 1 h in a cold room at 256 K (−17 °C), producing etched grain and subgrain boundaries. Images were collected digitally using a Leica DM2700 reflected-light microscope also installed in the cold room.

3. Experimental Results: Description and Comment

Our constant-hardness compliance data are presented in Fig. 2. The data are grouped and analyzed according to their initial steady-state creep stress, noted in the key; this is the stress defining segment (1) of any given experiment (cf. Fig. 1). Data groups are identified by symbol shape; different experimental specimens are identified by symbol shading. The data are compared to the steady-state flow law articulated for polycrystalline ice by Goldsby & Kohlstedt (2001), which is plotted as light-grey curves. The steady-state creep rates prior to stress reductions, given by the upper-rightmost data (annotated "SS"), match the flow law well. Furthermore, steady-state data analysis for the fine-grained specimens yields a stress exponent of n = 1.8±0.6, which is the value associated with a GBS rheology that is rate-limited by the actual sliding on the boundary (Goldsby & Kohlstedt, 2001). All data points at lower stresses in Fig. 2 reflect the constant-hardness strain rate described previously (segment (3) in Fig. 1); the compilation of points with the same symbol represents the compliance distribution (set by hardness) of a given microstructure. The total plastic strain accumulated in a given specimen, summing all stress-reduction cycles, was approximately 5%.

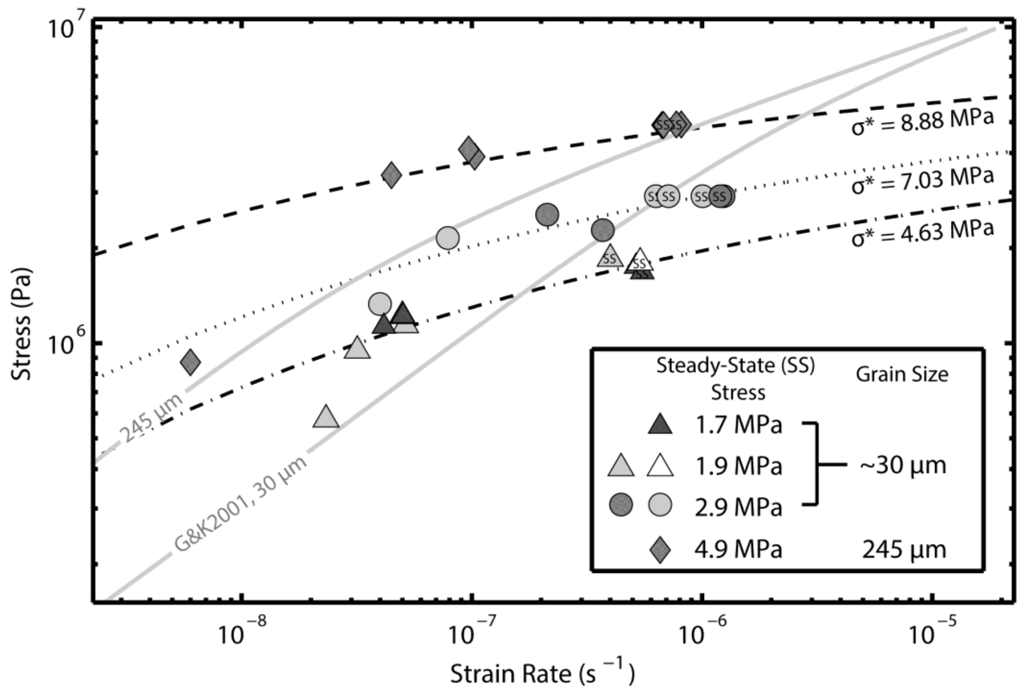

Figure 2: The constant-hardness creep compliance of polycrystalline ice determined by stress-reduction experiments. Data are grouped (key) according to the magnitude of differential stress characterizing segment (1) of an experiment (cf. Fig. 1). . Variations in symbol shading indicate different experimental specimens. The lambda law fits (Eq. (1)) for the data are shown as black broken curves; the hardness (σ*) for each fit is indicated. Deviation from the lambda law at lower stresses indicates a transition in the mechanism rate-limiting relaxation. The steady-state creep rates—here indicated as the clusters of data points at the far right of the graph (the data points annotated "SS")—are accurately predicted by the flow law of Goldsby & Kohlstedt (2001) (G&K2001), plotted as gray lines for comparison.

Fits of the lambda law to the data were determined by evaluating $\ln(\sigma)$ vs. $\dot{\varepsilon}^{-\lambda}$ via least-squares linear regression, from which $\dot{\varepsilon}^*$ and σ^* were determined from the slope and intercept. In each regression plotted in Fig. 2, λ was held constant at 0.15 [the theoretical value (Hart, 1970; Stone et al., 2004)] and all data for a steady-state-stress group were included. The data are well-fit by the lambda law at relatively high stresses, but at low stresses they exhibit higher strain rates than predicted by the lambda law. If one allowed λ to be a fitting parameter for the data groups, again, including all data within a group, unphysically large values of λ resulted. Ignoring the two lowest-stress data for each group, however, produced best fits with $\lambda = 0.13$ and $\lambda = 0.16$ for the 2.9 and 1.8 MPa data, respectively, in good agreement with the theoretical value..

The microstructures of our deformed samples are shown in Fig. 3. Subgrain boundaries are prevalent as shallow sublimation grooves in samples deformed in dislocation creep (Fig. 3a; corresponding to the diamonds in Fig. 2), but are sparse in samples deformed in the GBS regime (Figs. 3b, c; circles and triangles in Fig. 2). In addition, the subgrain boundaries present in the dislocation creep samples are an order of magnitude more widely spaced than predicted by the model of Raj & Pharr (1986). Samples deformed in the dislocation creep regime exhibit irregular grain boundaries, while samples deformed in GBS exhibit smooth grain boundaries and numerous four-grain junctions, a microstructural feature considered diagnostic of GBS (Langdon, 1991; Goldsby & Kohlstedt, 1997). Significant grain growth is not observed in the deformed specimens, based on a comparison to undeformed specimens, which were maintained at 77 K between fabrication and microstructural analysis.

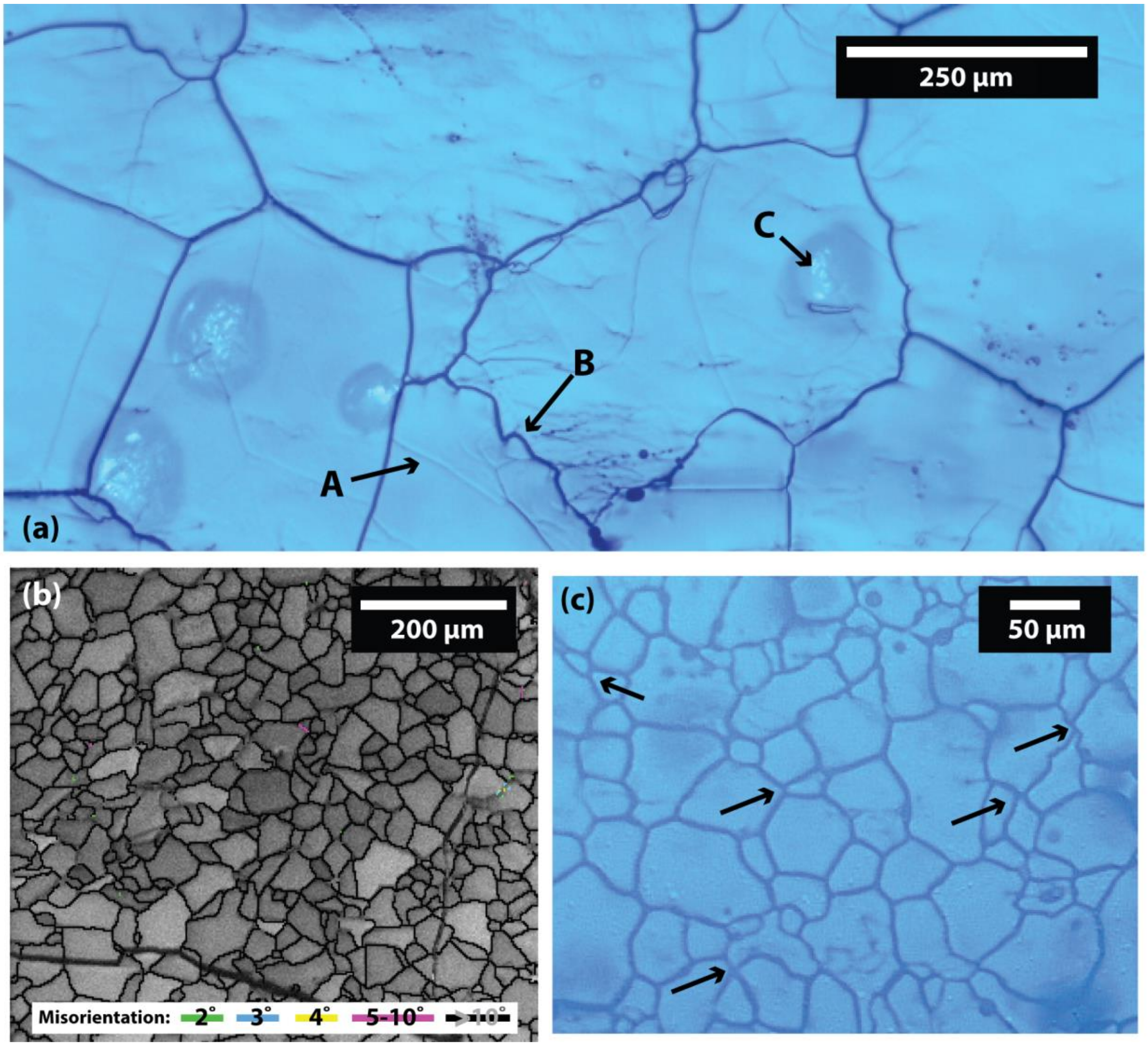

Figure 3: Microstructures corresponding to hardness data in Fig. 2. **(a)** Reflected light micrograph of sample deformed in the dislocation creep regime (d = 245 µm; initial σ = 4.9 MPa). Subgrain boundaries, generally occurring in parallel networks, are visible as shallow sublimation grooves (A). High angle grain boundaries are more deeply etched and exhibit roughness indicative of dislocation creep (B). Air bubbles in the samples are visible below the surface (C). **(b)** EBSD grain boundary map of sample deformed in GBS ($d \approx 30$ µm; initial σ = 1.9 MPa), color-coded by misorientation angle, overlying an EBSD band contrast image (an index of pattern quality); very few subgrains are observed in such samples. The fracture in the bottom left of the image occurred during preparation for EBSD. **(c)** Reflected light image of a sample deformed via GBS. Parallel subgrain "arrays" are rare. Four-grain junctions (arrows) are prevalent, however—indicative of flow rate-limited by GBS.

4. Discussion

The conformance of our data to the lambda law and the scaling of this behavior with stress indicate that the constant-hardness behavior of polycrystalline ice depends upon the applied stress. Furthermore, deviation from the lambda law at low stress is consistent with a material deforming via grain boundary sliding (Korhonen et al., 1987; cf. Crossman and Ashby, 1975). Unlike the behavior observed for halite by Stone et al. (2004), the constant-hardness response of our samples is not affected by the presence (or absence) of subgrains. Because they do not form in the fine-grained samples, their spacing is not a relevant basis upon which to scale the state-variable behavior. We must therefore explore alternative stress-dependent defect structures capable of defining microstructural hardness.

Such a feature may be found by exploring the physics of grain boundary sliding. The stress exponent of our creep data, the form of our constant-hardness curves, and the microstructures of samples deformed at low stress are consistent with steady-state flow that is rate-limited by grain boundary sliding (GBS) that is geometrically accommodated by fast glide of basal dislocations. Despite the fact that the dislocation-glide aspect of the rheology is essentially a short circuit (the mechanism of accommodation does not, to first order, dissipate energy), critical to the physics of GBS is the nucleation and consumption of basal-plane lattice dislocations at the grain boundaries. Thus, grain boundary structure has a direct effect on the GBS rheology and the stress-dependent evolution of this structure may explain the observed behavior in our experiments.

We did not analyze atomic-scale grain boundary structure in our specimens. The effect of applied stress on grain boundary structure in ice has been studied by Hondoh &

Higashi (1978, 1983), however, who performed concurrent x-ray topography and deformation of ice bicrystals. In these experiments, performed at 253 K, initially flat grain boundaries developed planar facets when subjected to a shear stress of ~0.1 MPa and after accumulating strains ~10^{-5} to 10^{-4}. The intersections of these facets generated stress concentrations that subsequently emitted basal dislocations into the grains. Indications of characteristic spacing of grain boundary topography have also been observed in Antarctic ice cores, in which Kipfstuhl et al. (2006) observed characteristic spacing of basal dislocation slip bands—emitted from stress concentrations on the grain boundary and indicative of grain boundary facet spacing—at all depths in the East Antarctic Ice Sheet.

Hondoh & Higashi (1983) attributed the development of faceted grain-boundary topography to interactions amongst grain boundary dislocations (GBDs). GBDs, which arise from the crystallographic mismatch between the grains on either side of the boundary, glide and climb within grain boundaries to produce sliding between grains. GBDs dissociate into lattice dislocations when their motion is impeded by obstacles—e.g., the intersection of facets—during deformation (e.g., Gifkins, 1976). GBDs will be characterized by a spatial distribution, but their mean spacing as a function of stress can be calculated in the same manner as the spacing of mobile lattice dislocations, i.e. proportional to $1/\sigma$, because the elastic stresses generated by GBD's are identical to those of lattice dislocations (Ashby, 1972). The distribution of GBD spacing and the related distribution of grain boundary facet size therefore represent potential stress-dependent microstructural features upon which to scale our hardness data. The adherence of our data to the lambda law suggests that these distributions are self-similar.

We therefore propose that grain boundary facets hinder the motion of GBD's, hardening the grain boundary in a manner comparable to that by which subgrain boundaries harden a material deforming via dislocation creep (cf. Stone et al., 2004). Thus, with sufficient accumulated strain, an increasing stress decreases the facet size, hardens the grain boundary structure and so raises σ^*. Further work is required to quantify the relevant spatial distributions of the elements of grain boundary topography (such as facets) in deforming ice, which is one aspect of our continuing research.

The low-stress tails in our hardness-curve data must reflect some physical aspect of energy dissipation on grain boundaries in our specimens. In materials whose steady-state deformation occurs by dislocation creep, deviation from the lambda law has been previously recognized as the transition from relaxation by dislocation motion to relaxation by grain boundary sliding (e.g. Alexopoulos et al., 1982). In the case of our fine-grained experiments, whose flow is initially rate-limited by the effective viscosity of the grain boundary, deviation from the lambda law represents a transition *from* GBS to a regime rate-limited by another mechanism. The strain rate at which the hardness data deviate from the lambda law is the point at which the strain rates by GBS and this second mechanism are equal; one can therefore solve for the viscosity of the second mechanism following the methodology of Crossman & Ashby (1975):

$$\eta_R = \left[\dot{\varepsilon}_T \left(\frac{C}{d^p} \right)^{1-n} \right]^{\frac{1-n}{n}}, \tag{2}$$

where η_R is the viscosity of the unknown, faster relaxation mechanism, $\dot{\varepsilon}_T$ is the strain rate at which the hardness data deviate from the lambda law, and p the grain size exponent of GBS. In Eq. (2), $C = A \exp(-E/RT)$ where A is the pre-exponential constant, E the activation energy for GBS and RT has the usual meaning. In this analysis, n is that of GBS rate-limited by sliding on the grain boundary.

We have calculated η_R for our two fine-grained experiments. Results and values used in the calculations are given in Table 1. The average of the two values of η_R is 4.8×10^6 Pa·s. This value is similar to the grain boundary viscosity of polycrystalline ice (2.1×10^7 Pa·s) inferred from internal friction experiments conducted by Kuroiwa (1964). Kuroiwa additionally calculated an activation energy of 54±2.7 kJ/mol for the observed relaxation mechanism, which is within the range of previously published values for grain boundary diffusion and volume diffusion in ice (Goldsby and Kohlstedt, 1997; cf. Ramseier, 1967). The hardness data in Fig. 2 make a claim as well: though sparse, the data in the low-stress "tails" for the samples with 30 μm grain size are well-fit by a slope of 1, highly suggestive of diffusion creep.

5. Conclusion/Summary

Stress-reduction experiments have successfully described the constant-hardness creep compliance of polycrystalline ice. Our results are indicative of a hardness set by the applied stress, but the stress-sensitive microstructural feature previously used to scale hardness curves—the distribution of subgrain boundary spacing—is not applicable to our fine-grained samples. The physical basis of the scaling between hardness curves in ice deforming via GBS is instead argued to be the spatial distribution of grain boundary facets, which is developed by the shear stress-impelled motion of grain boundary dislocations. Facets control the emission of basal dislocations into grain interiors—required for accommodation of grain boundary sliding in polycrystalline ice. Grain boundary topography evolves with stress and determines the microstructural hardness of polycrystalline ice.

This work suggests that an icy body (such as a glacier, ice sheet, or shell of an icy satellite) deforming at steady state in the GBS regime develops a stress-dependent topography on the grain boundaries that influences the material's response to short-term, transient loading. The results may be particularly important to constraining the relevant length scale of tidal heating in icy satellites, where tidal stresses interact with long-term convective stresses to heat the ice shell of icy moons such as Europa (e.g., Tobie et al., 2003).

Alexopoulos, P. S., R. L. Keusseyan, G. L. Wire, and C. -Y. Li (1982), Experimental investigation of nonelastic deformation emphasizing transient phenomena by using a state variable approach, in *Mechanical Testing for Deformation Model Development, STP 765*, edited by R. W. Rhode and J. C. Swearengen, pp. 148-184, American Society for Testing and Materials, Philadelphia, PA.

Ashby, M. F. (1972), Boundary defects and atomistic aspects of boundary sliding and diffusional creep, *Surf. Sci., 31*, 498-542.

Crossman, F. W. and M. F. Ashby (1975), The non-uniform flow of polycrystals by grain boundary sliding accommodated by power-law creep, *Acta Metall.*, *23*, 425-440.

Gifkins, R. C. (1976), Grain-boundary sliding and its accommodation during creep and superplasticity, *Metall. Trans. A, 7A*, 1225-1232.

Goldsby, D. L. and D. L. Kohlstedt (1997), Grain boundary sliding in fine-grained ice I, *Scripta Mater., 37*, 1399-1406.

Goldsby, D. L. and D. L. Kohlstedt (2001), Superplastic deformation of ice: Experimental observations, *J. Geophys. Res.*, *106*, 11017-11030.

Hamann, I., C. Weikusat, N. Azuma, S. Kipfstuhl (2007), Evolution of ice crystal microstructure during creep experiments, *J. Glaciol., 53*, 479-489.

Hart, E. W. (1970), A phenomenological theory for plastic deformation of polycrystalline metals, *Acta Metall.*, *18*, 599-610.

Hondoh, T. and A. Higashi (1978), X-Ray diffraction topographic observations of the large-angle grain boundary in ice under deformation, *J. Glaciol., 21*, 629-638.

Hondoh, T. and A. Higashi (1983), Generation and absorption of dislocations at large-angle grain boundaries in deformed ice crystals, *J. Phys. Chem.*, *87*, 4044-4050.

Jackson, M. S., C. W. Cho, P. Alexopoulos, and C. -Y. Li (1981), A phenomenological model for transient deformation based on state variables, *J. Eng. Mater. -T. ASME*, *103*, 314-325.

Kipfstuhl, S., I. Hamann, A. Lambrecht, J. Freitag, S. H. Faria, D. Grigoriev, and N. Azuma (2006), Microstructure mapping: a new method for imaging deformation-induced microstructural features of ice on the grain scale, *J. Glaciol.*, *52*, 398-406.

Korhonen, M. A., S. -P. Hannula, and C. -Y. Li (1987), State variable theories based on Hart's formulation, in *Unified Constitutive Equations for Creep and Plasticity*, edited by A. K. Miller, pp. 89-137, Elsevier Applied Science, London.

Korhonen, M. A., C. -Y. Li, and J. C. Gibeling (1985), A state variable approach to transient creep deformation in stress reduction experiments, *Mater. Sci. Engr.*, *74*, 179-188.

Kuroiwa, D. (1964), Internal friction of Ice II: The grain boundary internal friction of ice, *Contrib. Inst. Low Temp. Sci. (Hokkaido Univ), A18*, 38-48.

Langdon, T. (1991), The physics of superplastic deformation, *Mater. Sci. Engr. A, A137*, 1-11.

Piazolo, S., M. Montagnat, and J. R. Blackford (2008), Sub-structure characterization of experimentally and naturally deformed ice using cryo-EBSD, *J. Micros., 230*, 509-519.

Prior, D. J., K. Lilly, M. Seidemann, M. Vaughan, L. Becroft, R. Easingwood, S. Diebold, R. Obbard, C. Daghlian, I. Baker, T. Caswell, N. Golding, D. Goldsby, W. B. Durham, S. Piazolo, and C. J. L. Wilson (2015), Making EBSD on water ice routine, *J. Micros*., doi:10.1111/jmi.12258.

Raj, S. and G. Pharr (1986), A compilation and analysis of data for the stress dependence of the subgrain size, *Mater. Sci. Engr., 81*, 217-237.

Ramseier, R. O. (1967), Self-diffusion of tritium in natural and synthetic ice monocrystals, *J. Appl. Phys., 38*, 2553-2556.

Stern, L. A., W. B. Durham, and S. H. Kirby (1997), Grain-size-induced weakening of H_2O ices I and II and associated anisotropic recrystallization, *J. Geophys. Res., 102*, 5313-5325.

Stone, D. S., T. Plookphol, and R. F. Cooper (2004), Similarity and scaling in creep and load relaxation of single-crystal halite (NaCl), *J. Geophys. Res.*, *109*, B12201, doi:10.1029/2004JB003064.

Tobie, G., G. Choblet, C. Sotin (2003), Tidally heated convection: Constraints on Europa's ice shell thickness, *J. Geophys. Res., 108(E11)*, 5124, doi:10.1029/2003JE002099

Weertman, J. and J. R. Weertman (1983), Mechanical properties, strongly temperature-dependent, in *Physical Metallurgy (Third Edition)*, edited by J. W. Cahn and P. Haasen, pp. 1309-1340, Elsevier Science Publishers B.V., Amsterdam.

Table 1: Calculated effective grain-boundary viscosities*

Experiment	η_R (Pa·s)
2.9 MPa, d = 31 μm	4.33×10^{6}
1.8 MPa, d = 31 μm	5.33×10^{6}
Parameter	**Value**[a]
A	3.9×10^{-3} MPa$^{-1.8}$m$^{2.4}$s^{-1}
n	1.8
p	1.4
E	49 kJ mol^{-1}

*See Equation (2)

[a] all parameter values from Goldsby & Kohlstedt (2001)

Chapter 3 | Inhibited Grain Growth During Grain Size-sensitive Creep in Polycrystalline Ice; An Energy Dissipation Perspective

Tess E. Caswell[1] and Reid F. Cooper[1]

[1]Department of Earth, Environmental and Planetary Sciences, Brown University, Providence, RI, USA

Abstract

Concurrent creep and annealing experiments in which two identical polycrystalline ice Ih specimens are subjected to the same time-temperature history while one of the specimens is actively deformed via grain size-sensitive (GSS) creep demonstrate a dichotomy in microstructural evolution: under certain conditions, grains do not grow in the deforming specimen. We have explored the conditions of inhibited grain growth through creep (σ = 0.25-1.85 MPa) and annealing (T = 240 K, durations 4-14 d) experiments on specimens of varying initial grain size ($d \approx$ 6-63 μm). The results are interpreted in the context of non-equilibrium thermodynamics, specifically comparing the relative energy dissipation rates of both grain growth and GSS creep. When a higher rate of energy dissipation is achieved by creep than by grain growth, the grains do not grow. An examination of the limited database on GSS flow and grain growth in silicates conforms to the model. The results are applied to the question of rheological weakening and the mechanical evolution of terrestrial ice sheets and the shells of icy satellites in the outer solar system.

1. Introduction

Grain size evolution in deforming, polycrystalline ice is critical to processes both on and off the Earth. Grain size affects terrestrial predictions of the rate of sea level rise through its impact on rheological properties and the rate of ice loss from the Greenland and Antarctic Ice Sheets. Although both field data and numerical models suggest that ice sheets are susceptible to catastrophic collapse on timescales less than 10^3 a (Pollard & DeConto, 2009; Sejrup et al., 2016), the response of these ice sheets to climatic forcing remains one of the greatest uncertainties in projections of 21^{st}-century sea level rise (Alley & Joughin, 2012; Willis & Church, 2012). Models of ice sheet stability incorporate factors including climate coupling (Gasson et al., 2016), grounding line dynamics and buttressing by floating ice shelves (Pollard & DeConto, 2009), basal hydrology (Schoof, 2010), and ice rheology (Deblonde & Peltier, 1991; Pettit et al., 2011), but the latter factor is complicated by the observed grain size-sensitivity of polycrystalline ice at conditions appropriate to glaciers and ice sheets (Cuffey et al., 2000; Goldsby & Kohlstedt, 2001; Stern et al., 1997). An additional element – grain size – must therefore be added to ice sheet flow models, and accurately predicting ice sheet stability in the face of a warming climate thus requires knowledge of grain size evolution within deforming ice.

Beyond Earth, polycrystalline ice flows within the interiors of icy moons of the outer solar system. Jupiter's moon Europa, for example, possesses an ice I shell up to 30 km thick overlying a liquid ocean (Billings & Kattenhorn, 2005; Nimmo et al., 2003; Ojakangas & Stevenson, 1989). The shell experiences convection, driving tectonic features observed on the moon's surface (Kattenhorn & Prockter, 2014; Pappalardo et al., 1998). The vigor of convection and, hence, an understanding of the driving stresses for tectonic deformation are a strong function of the viscosity of the ice (Collins et al., 2009). Europa's ice shell is simultaneously heated by tidal dissipation, which depends upon the viscosity of the ice (Tobie et al., 2003) and upon convective stresses, if present (McCarthy & Cooper, 2016). At Saturn, the icy moon Enceladus erupts plumes of water vapor and ice from over one hundred active vents along four strike-slip faults known as "Tiger Stripes" in the moon's South Polar Terrain (SPT) (Porco et al., 2014; Porco et al., 2006). Plume activity is regulated by tidal forces (Porco et al., 2014) and is thought to be the source of Saturn's E-ring (Baum et al., 1981; Kempf et al., 2010; Spahn et al., 2006), suggesting that the geysers have persisted for some time. The relationships between tidal heating, possible convection beneath the SPT, and deformation in the vicinity of the "Tiger Stripes" depend strongly on the viscosity structure of the ice shell beneath the SPT. Because grain size-sensitive (GSS) flow is expected to dominate at the pressures and temperatures within these deforming ice I shells (Barr & Pappalardo, 2005; Barr & Showman, 2009), the evolution of grain size in these settings is a critical physical process that should be represented in any authoritative model of icy satellite geophysics.

In many settings, such as the margins of active ice streams (Echelmeyer et al., 1994), it is logistically impractical to measure the grain size of the ice directly [although grain size evolution of frost deposited on the surfaces of icy satellites can be inferred from spectral observations (Clark, 1981) and has been modeled (Clark et al., 1983)]. Estimating grain size evolution in a deforming, polycrystalline material generally involves application of piezometers, which are semi-empirical formulae describing the relationship between stress and the grain size set by dynamic recrystallization (Poirier, 1985; Shimizu, 1998; Twiss, 1977). A second approach, similar to piezometers, is the "paleowattmeter" which describes recrystallized grain size as a function of the relative energy dissipation rate by each rheological mechanism effecting creep (Austin & Evans, 2007). The underlying assumption of a piezometer (or wattmeter), however, is that sufficient dislocation activity occurs to recrystallize the material – an assumption that recent experimental work has shown to be inappropriate in ice deforming via grain size-sensitive flow (Caswell et al., 2015). Based on piezometric considerations alone, one might then expect that normal grain growth occurs unopposed in the GSS regime. However, previous experiments conducted on ice in the GSS regime have shown very little change in the grain size of deformed specimens despite experiments lasting more than a week (Caswell et al., 2015; Goldsby & Kohlstedt, 1997). These results suggest that grain growth is inhibited during grain size-sensitive flow.

We propose — and, in this experimental study, demonstrate — that a comprehensive model of grain size evolution should consider rates of (free) energy dissipation. When a nonequilibrium mechanical potential such as a sustained deviatoric stress is applied to a system – as in, for example, a creep test on a specimen of ice or, naturally, when convective stress affects a planetary ice shell – the system texture evolves to a steady-state (or, a "non-equilibrium stationary state") whereby the additional energy input is dissipated by the most rapid means available; this postulate is an application of the maximum entropy principle in dynamics, i.e., non-equilibrium thermodynamics, to crystalline plasticity (Kondepudi & Prigogine, 1998, Ch. 15). In the physics probed here, two physical processes of energy dissipation, specifically grain growth and GSS flow, compete. In general, grains grow because the free-energy density associated with grain boundaries is thereby lowered; the rate of grain growth diminishes with growth because the driving potential is reduced. Strain energy density associated with a persistent deviatoric stress is dissipated by inelastic flow; for a grain-size-sensitive rheology, the rate of that dissipation is diminished as grains grow. The criterion that a system evolves to a texture that, at steady state, maintains as high an energy dissipation rate as practicable means that the response overall is dominated by the competing mechanism that dissipates energy most rapidly. Calculating relative energy dissipation rates of processes occurring at grain boundaries in a polycrystalline material deforming via GSS creep reveals that, for certain conditions of stress and grain size, the system can dissipate energy faster via GSS creep than by grain growth. Under such conditions, grain growth would be suppressed.

2. Theoretical Considerations

The driving force for normal grain growth is the chemical potential gradient across a curved grain boundary (Alley et al., 1995; Feltham, 1957; Hillert, 1965; Sutton & Balluffi, 1995). Because grain boundary interfacial energy, γ_{GB}, is a function of the radius of curvature of the grain, variations in curvature between the opposite sides of a grain boundary produce chemical potential gradients across the boundary that drive atomic diffusion and lead to growth of the low-energy grain. The difference in chemical potential across the boundary is calculated as

$$\Delta\mu_{Growth} = \frac{\zeta\gamma_{GB}\Omega}{\Delta r}, \quad [1]$$

where ζ is a constant depending on the grain growth model, γ_{GB} is grain boundary energy per unit area, Ω is molar volume, and r is grain radius. The value of γ_{GB} for high-angle (>15°) tilt boundaries in ice has been measured as 0.065 J m^{-2}, though this value varies as a function of grain boundary misorientation (Druetta et al., 2013; Ketcham & Hobbs, 1969; cf. Sutton & Balluffi, 1995). The chemical potential gradient arising from this difference across the width of a grain boundary is the driving force for diffusion of atoms/molecules from the more tightly-curved grain to that with larger r (Alley et al., 1995; Hillert, 1965; Sutton & Balluffi, 1995); a grain with larger radius of curvature will thus "eat" a grain with a smaller radius of curvature. The rate at which growth occurs is thus a convolution of this chemical potential gradient and the kinetics of diffusion, which is captured by the equation for normal grain growth:

$$d^2 - d_o^{\,2} = 4Kt\,, \qquad [2]$$

where d is final grain size (diameter), d_o is initial grain size, t is time, and K is the thermally activated growth rate constant (K=$K_o$exp[–Q/RT], where Q is the activation energy for boundary diffusion) (Arena et al., 1997; Gow, 1969; Poirier, 1985). It is K that integrates the chemical potential gradient due to grain boundary curvature with diffusion kinetics.

Equation 2 can be inserted into a simple geometrical expression (number of grains × grain surface area × γ_{GB}) to formulate the time-dependent total grain boundary energy per unit volume (J m^{-3}) during grain growth:

$$E_{GG} = \frac{E_{GB}}{V} = \frac{6\gamma_{GB}}{\sqrt{d_o^{\,2} + 4Kt}}\,. \qquad [3]$$

The number of grains is estimated by dividing a unit volume by the grain volume, and the constant in Eq. 3 is the surface area to volume ratio of the grains (for either cubic or spherical grains). Equation 3 can next be differentiated with respect to time to determine the energy dissipated per unit of time during normal grain growth:

$$\dot{E}_{GG} = -12\gamma_{GB}K\left(d_o^{\,2} + 4Kt\right)^{-3/2}. \qquad [4]$$

When a deviatoric stress is applied to the aggregate, the chemical potential gradient driving grain growth now occurs in the context of new chemical potential gradients generated by differences in normal tractions, T_n, along the grain boundary (Raj & Ashby, 1971). The change in chemical potential produced by a normal traction on the grain boundary is expressed by (Herring, 1950; Raj, 1975):

$$\Delta\mu_{Traction} = \Delta T_n \Omega \ . \qquad [5]$$

For a faceted grain boundary undergoing steady-state grain boundary sliding (as is the case for polycrystalline ice at planetary conditions – cf., Barr & Pappalardo, 2005; Goldsby & Kohlstedt, 2001; Hondoh & Higashi, 1978), the normal traction at the center of a facet may be more than twice that at the edges of the facet (Raj, 1975). The length scale of spatial variability in these tractions determines the chemical potential gradient against which "steady-state" flow of atoms gives rise to diffusion creep (or grain boundary sliding) (Raj & Ashby, 1971; Raj, 1975).

The energy dissipation rate due to grain boundary sliding can be calculated in a straightforward manner as

$$\dot{E}_{GBS} = \sigma\dot{\varepsilon} \qquad [6]$$

where σ is the applied deviatoric stress and $\dot{\varepsilon}$ is the strain rate in the specimen. Diffusion driven by a gradient in normal traction on the grain boundary is inherent in the grain size-sensitivity and Boltzmann statistics of the strain rate,

$$\dot{\varepsilon}_i = \frac{A_i \sigma^{n_i}}{d^{p_i}} \exp\left(\frac{-Q_i}{RT}\right), \qquad [7]$$

where A is the pre-exponential constant, σ is the deviatoric stress, n is the stress exponent, d is the grain size, p is the grain size sensitivity, Q is the activation energy, and RT has the usual meaning. The subscript i is used to indicate the deformation mechanism. Polycrystalline ice deforms by three kinetically independent rheological mechanisms: dislocation creep (which is rate-limited by the glide and climb/cross-slip of lattice dislocations on multiple slip systems), grain boundary sliding (GBS), and diffusion creep (chemical diffusion of H^+ and O^{2-} species either through the lattice or along grain boundaries) (Goldsby & Kohlstedt, 2001). GBS in ice is a serial-kinetic process of sliding along the grain boundary via motion of boundary-defining point and line defects and lattice dislocation glide on the basal (0001) plane. Either of these processes may be rate-limiting. Thus, the composite rheology for polycrystalline ice, incorporating each of these mechanisms, includes four terms:

$$\dot{\varepsilon}_{Tot} = \dot{\varepsilon}_{dis} + \left(\frac{1}{\dot{\varepsilon}_{GBS}} + \frac{1}{\dot{\varepsilon}_{BS}} \right)^{-1} + \dot{\varepsilon}_{diff}, \quad [8]$$

where $\dot{\varepsilon}_{dis}$, $\dot{\varepsilon}_{GBS}$, $\dot{\varepsilon}_{BS}$, and $\dot{\varepsilon}_{diff}$ are the strain rates by dislocation creep, grain boundary viscosity-limited GBS, basal slip-limited GBS, and diffusion creep, respectively (Goldsby & Kohlstedt, 2001).

In Eqs. 4 and 6 we now have a model by which to evaluate grain growth and creep with regard to the maximum entropy principle articulated in Section 1 (Kondepudi & Prigogine, 1998, Ch. 15). As illustrated in Fig. 1a, these processes represent macroscopic manifestations of chemical potential gradients that compete to drive diffusion along (or near) grain boundaries in materials deforming via grain size-sensitive flow. To maximize entropy, the system evolves to a texture that dissipates energy most rapidly. Thus, whichever mechanism has the highest dissipation rate will "win out:" If the energy dissipation rate by GBS exceeds the energy dissipation rate of grain growth, the grains will not grow. Conversely, higher dissipation rate via growth will favor growth. Conditions favoring each process are illustrated schematically in Fig. 1b.

Critical to this discussion is the grain size-sensitivity of Eq. 7. The grain size-sensitivity, p_i, is >0 for both diffusion creep and GBS that is rate-limited by boundary

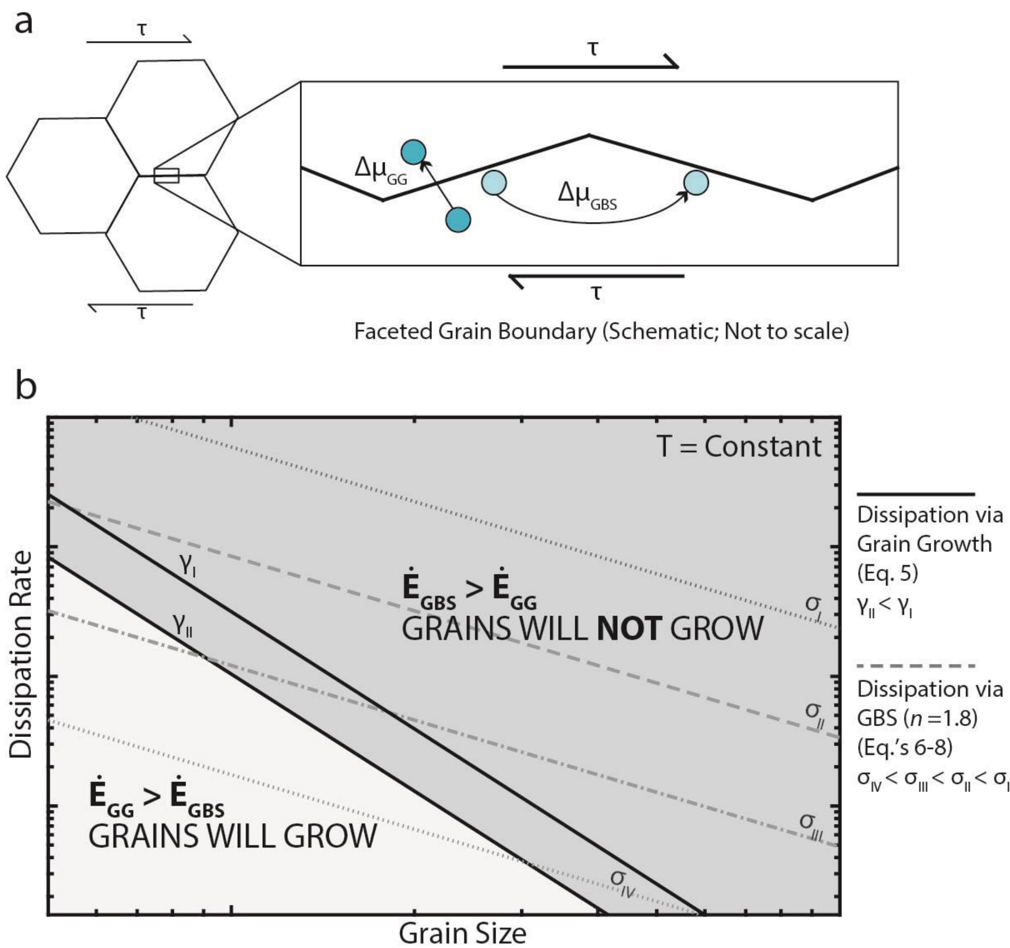

Figure 1: a) Illustration of competing chemical potential differences on a faceted grain boundary subjected to a persistent shear stress, τ. An atom diffusing across the boundary to produce grain growth results in a chemical potential reduction of $\Delta\mu_{GG}$. An atom diffusing from high- to low-normal traction (either through the grain—shown—or along the boundary) produces a chemical potential reduction of $\Delta\mu_{GBS}$. Whichever of these processes produces the highest rate of energy dissipation, $\dot{E}$, will dominate. b) Schematic representation of the predicted effect on grain growth when the dissipation rates due to the chemical potential differences described in (a) vary. When the dissipation rate is greater via GBS than by grain growth, the grains will not grow. Conversely, if a greater dissipation rate occurs via growth, the grains will grow. This is illustrated by comparing the macroscopic dissipation rates achieved by grain growth (solid lines) and steady-state GSS creep (dashed lines). The rate of dissipation by grain growth is affected by interfacial energy (γ) and the grain growth constant (K). Variations in these parameters have similar effects on the dissipation rate, illustrated by changing γ in the figure.

sliding. The implication of this grain size sensitivity is that in the GSS regime, an increase in grain size leads to a reduction of the dissipation rate via GBS (Eq. 6). If this reduction is not accompanied by sufficiently large dissipation due to grain growth, then this path of textural evolution has diminished the system's ability to dissipate energy. If grain growth does not benefit the system by providing the fastest path of energy dissipation, it will not occur.

3. Experimental Approach

3.1. Specimen Preparation

Experimental specimens were prepared specifically to explore grain size evolution and were thus fabricated with different initial grain sizes: "Coarse" specimens with grain size > 30 μm, "Medium" specimens with grain size 10-25 μm, and "Fine" specimens with grain size < 10 μm. Two distinct methods were utilized: hot-pressing and pressure-cycling (Goldsby & Kohlstedt, 2001; Stern et al., 1997). Hot-pressed ice is fabricated by nebulizing deionized water in air and directing the spray into liquid nitrogen (LN_2). The resulting slurry is then sieved in LN_2 to obtain the desired grain size. Sieving is performed under N_2 gas so that atmospheric CO_2 and water vapor do not deposit onto the sieved material. The resulting powder is packed into a cylindrical vacuum mold and hot pressed in dry ice (195 K) at 100 MPa for 2 h. The resulting sample is fully dense and possesses a grain size approximately equal to the particle size of the initial sieved powder (Caswell et al., 2015; Goldsby & Kohlstedt, 1997; Prior et al., 2015). By this method we produced 1-cm diameter, 2-cm length cylindrical specimens of grain sizes in the range 25-60 μm.

Pressure-cycled ice is prepared in an identical manner to hot pressing, except for a sequence of high-pressure/low-pressure cycles prior to the final hot pressing (Stern et al., 1997). Each pressure cycle begins by increasing the (nominally hydrostatic) stress on the sample to 250-300 MPa, which initiates a phase transformation from ice Ih to the high-density polymorph, ice II. The sample is held at 250-300 MPa for 5 min to allow the phase transformation to complete before the pressure is rapidly released. During the phase transformation back to ice I, the kinetics of nucleation dominate relative to those of grain growth and a high density of ice I nuclei is produced. These nuclei then grow to produce specimens of extremely fine grain size (5-10 μm). The pressure-cycling process is repeated three to six times, with greater numbers of cycles producing finer grain sizes. In this manner we produced 1-cm diameter, 2-cm length cylindrical specimens with mean grain sizes 8-30 μm.

The experiments involved characterizing and comparing three types of specimens: starting material (undeformed/unannealed), the deformed material, and material that was annealed under identical (and simultaneous) time-temperature (thermal) conditions as the deformed material without being subjected to a deviatoric stress. In what follows, the first type of material is described as "starting," the second as "deformed" and the third as "thermal." Prior to each experiment, a section of the starting material was cut from the cylindrical sample and placed directly into a liquid nitrogen storage dewar (77 K) for later microstructural comparison; these specimens are subsequently referred to as the "starting" material. A second section of the sample was placed inside the apparatus, adjacent to the deformation specimen but not subject to load; these specimens are subsequently referred to as "thermal" specimens. "Deformed" specimens were subjected to deviatoric stresses of 0.25-1.65 MPa at temperatures of 233-240 K for 4-11 d. The deformed and thermal specimens were quenched simultaneously in liquid nitrogen immediately following each experiment.

All specimens were stored in dry ice (195 K) between fabrication and use, generally for less than 48 h. At the start of each experiment the deformation and thermal specimens were transferred from dry ice to the apparatus, initially equilibrated at 195 K. The apparatus then passively warmed to the experiment temperature, allowing the specimens to thermally equilibrate over the course of 24 h. A low deviatoric stress (250-400 kPa, depending on estimated initial grain size) was applied to the deforming specimen during equilibration in order to suppress grain growth during this timeframe.

Two sets of unconfined, uniaxial creep experiments were conducted to explore grain size evolution as a function of deviatoric stress for specimens of varying initial grain size. The first set of experiments utilized a dead-weight creep apparatus described elsewhere (Goldsby & Kohlstedt, 1997). The second set of experiments utilized a computer-controlled, servo-mechanical apparatus (Instron Model 1361) modified by the addition of an ethanol-bath cryostat that maintains sample temperature to a precision of ±0.5 K (Fig. 2). Strain and strain rate in the specimen were determined by measuring displacement between ceramic plates abutting the specimen using a displacement-voltage transducer (direct current differential transformer—DCDT). Specimen temperature was measured by a Type-T (copper–constantan) thermocouple embedded in the uppermost of these plates. The data acquisition system employed averaging to mitigate electronic noise: though data are recorded at 5 Hz, each recorded data point is an average of 1,000 samples collected at 5 kHz. Including this averaging and analog-to-digital conversion,

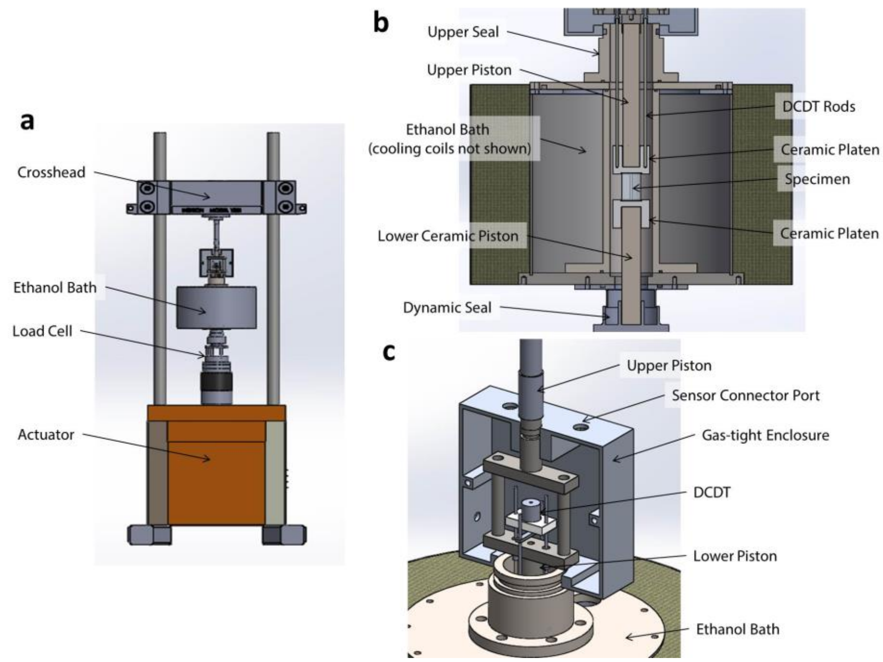

Figure 2: The servomechanical apparatus and cryogenic chamber employed in the majority of experiments. a) The full assembly, including the Instron 1361 load frame and actuator, ethanol bath cryostat, and extensometer. The cryostat is affixed to the load frame by cantilever steel beams (not shown). b) The sample assembly within the cryostat. The liquid reservoir of the dynamic seal at the base of the cryostat provides a low-friction, gas-tight seal at the base of the sample chamber. The specimen (which is ~5 cm in length) is abutted by two ceramic (Macor^{TM}) platens, the distance between which is measured by a direct-current differential transformer (DCDT), shown in (c). The core and body of the DCDT are connected to the lower and upper platens, respectively, by tungsten rods. (c) A gas-tight enclosure at the top of the cryostat houses the DCDT and sample assembly from ambient air, and is periodically purged with dry nitrogen gas to prevent frost.

strain resolution was 1×10^{-7}. Load was measured by a 2.2 kN-capacity load cell with resolution of 0.035 N. The computer-controlled load setpoint was adjusted every ~24 h to maintain constant stress on the sample, again assuming constant-volume deformation of a cylindrical sample.

The experiments were designed to fall into two groups: one in which the deformation conditions favored grain growth in the deformed specimen according to the model presented in Section 2, and the other in which grain growth is expected to be inhibited. Dissipation rates by grain growth were calculated using Eq. 4, then deviatoric stress adjusted to control the dissipation rate by creep (Eq. 6).

In one experiment, a “grow” specimen was also studied. This specimen was sectioned from a deformed specimen after deformation and reinserted into the cryostat for stress-free annealing at 240 K for 48 h. This specific experiment allowed us to evaluate whether cavitation, potentially induced by GBS, influenced grain size evolution in deformed samples.

3.2. Microstructure Analysis

Microstructural analyses were performed via reflected-light optical microscopy. Because microstructural analyses were conducted several weeks after the completion of mechanical experiments, specimens were stored in a liquid-nitrogen dewar (−196°C) between experiments and microscopy.

Microscopy was conducted in a cold room at Lamont-Doherty Earth Observatory (Palisades, New York, USA). Sections for analysis were cut from each specimen using a razor blade in a cooler over liquid nitrogen. Sections were then transferred to the cold room (−17°C) where they were bonded to a glass slide with drops of water. Specimens were prepared for microscopy by shaving a flat surface with a microtome, then allowing the shaved surface to etch via sublimation in the cold room for 1-2 min to produce etched grain boundaries (Caswell et al., 2015). Images were collected with a Leica DM2700 reflected-light microscope in the cold room.

Image analysis was conducted using the NIH software ImageJ. Grain size was measured by the line-intercept method, applying a multiplicative factor 1.5 to account for geometric effects (Exner, 1972). Grain sizes reported are averages taken from multiple images of each sample. EBSD data was analyzed using the Channel 5 HKL software package.

4. Results

4.1. Mechanical Data

The steady-state stress and strain rate pairs from our mechanical tests are shown in Fig. 3. All measured steady-state strain rates are broadly consistent with those predicted by the composite rheology of Goldsby & Kohlstedt (2001) (indicated by gray lines for comparison in Fig. 3), although there is substantial scatter in the “fine” data due to grain growth during the experiments. Multiple load steps were conducted in some experiments. The stress and grain size sensitivities observed in each experiment should be treated with caution, however, because several experiments were conducted under conditions expected to permit grain growth. The resulting stress exponent is therefore a convolution of stress and grain size variations. It is additionally worth noting that the stress exponent for some experiments is constrained by only two data points. For the experiment with

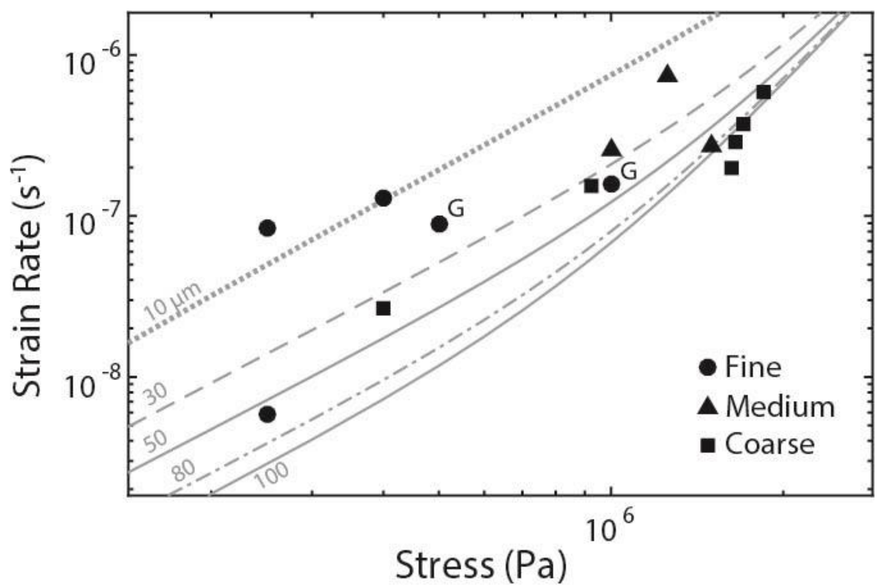

Figure 3: Steady-state strain rate vs. differential stress for our experimental specimens. For reference, the composite flow law of Goldsby & Kohlstedt (2001) is plotted as gray lines for grain sizes comparable to our deformed specimens. The symbol sizes are defined based on the starting – not final – grain size in the specimen; thus, fine-grained specimens which experienced growth are still labeled as "Fine" despite reduced strain rates indicative of grain growth during some experiments. Load steps during which statistically-significant growth occurred are indicated by the letter "G" to the upper right of the corresponding symbol.

most load steps and least measured change in grain size (SD4; experiment designations are descried in Table 1), the observed stress exponent is $n = 1.6$ (cf. Eq. 7).

4.2. Microstructure

Optical micrographs of representative samples are shown in Fig. 4. Two grain boundary morphologies are seen in the deformed specimens depending upon whether grain growth occurred during the experiment. This variation is exhibited in Fig. 4, in which the left-hand column (a-c) illustrates an experiment in which the deformed specimen was subjected to conditions expected to inhibit grain growth, while the right-hand column (d-f) illustrates an experiment in which the deformed specimen was subjected to conditions expected to allow growth.

It is apparent from visual inspection of Figs. 4a and 4b that grain size remains similar between the deformed specimen and the starting material in some experiments. In these experiments the deformed specimen exhibits numerous four-grain junctions (black arrows, Fig. 4b). Many grain boundaries are linear, showing very little evidence for migration. Thermal specimens (e.g., Fig. 4c) exhibit highly curved grain boundaries. Small grains generally possess convex-outward grain boundaries (white arrow), while large grains have concave-inward boundaries (black arrow). Comparison of Figs. 4a and 4c clearly illustrates a marked increase in grain size in the thermal specimen.

Figures 4d and 4e show the starting material and deformed specimen for a single experiment conducted under conditions in which grain growth is expected to occur. It is clear from visual inspection that the grain size in the deformed specimen is much larger than that in the starting material. In contrast to the deformed specimen shown in Fig. 4b (for which growth was not expected to occur), grain boundaries are generally curved

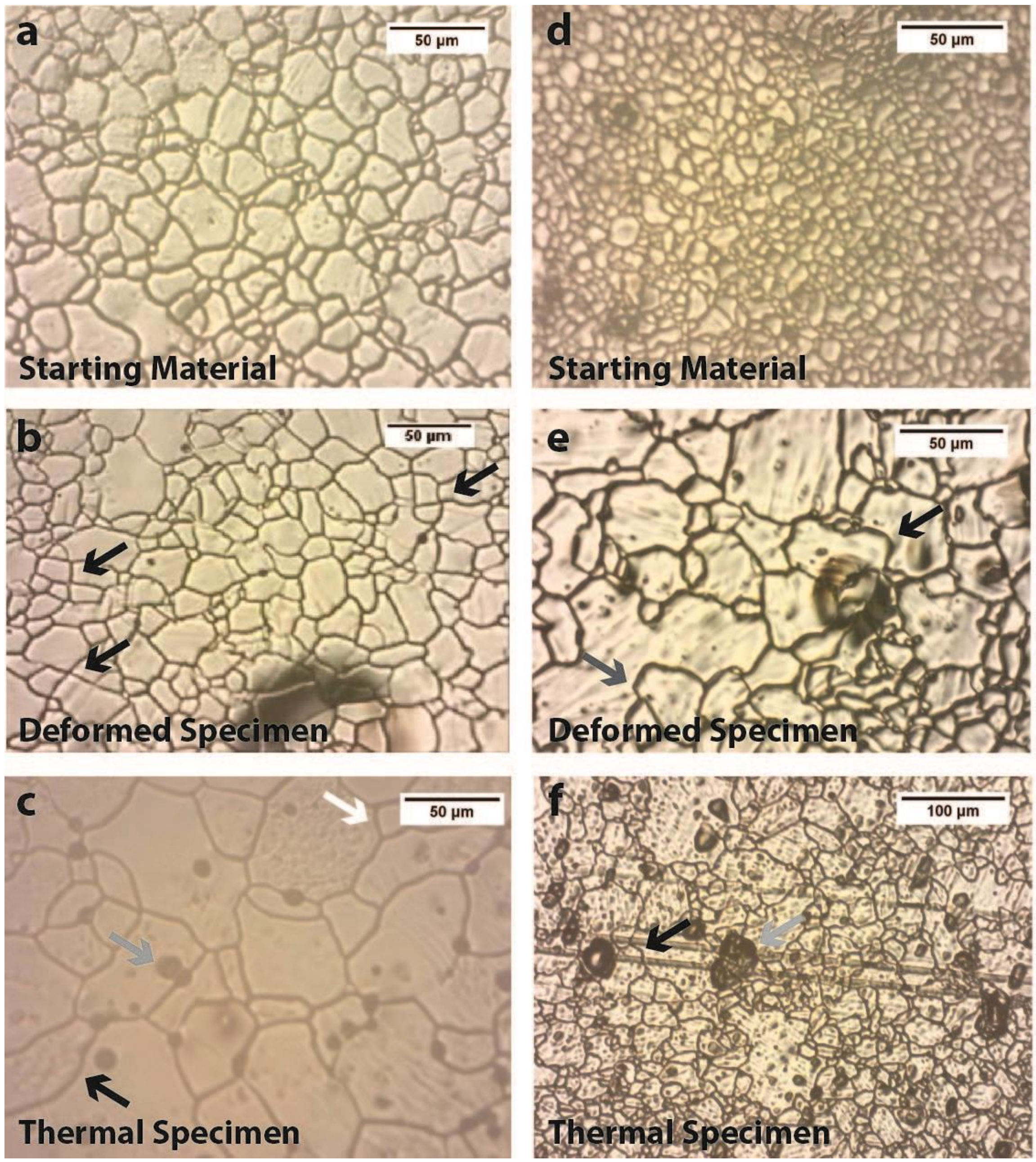
a
50 µm
Starting Material
b
50 µm
Deformed Specimen
c
50 µm
Thermal Specimen
d
50 µm
Starting Material
e
50 µm
Deformed Specimen
f
100 µm
Thermal Specimen

Figure 4: Reflected light micrographs of experimental specimens. The column on the left represents an experiment (code GVF1; see Table 1), conducted under conditions in which grain growth is inhibited in the deforming specimen. The right-hand column represents an experiment (code AVF3), conducted under conditions expected to allow grain growth. a) Starting material. d = 29.9 ± 5.4 µm. b) Deformed specimen (minimum σ_1 = 1 MPa, ε_{total} = 10.1%, duration 3.7d). d = 24.5 ± 5.4 µm. Grain boundaries are generally very straight, and numerous four-grain junctions are visible (black arrows). The grain size is very similar to that in the starting material. The compression axis is perpendicular to the page. c) Thermal specimen, d = 66.8 ± 21.5 µm. Boundaries are concave-in on large grains (black arrow) and concave-out on small grains (white arrow) indicating normal grain growth. Dark spots are frost accumulated on this specimen during microscopy (gray arrow). d) Starting material, experiment AVF3. d = 8.2 ± 0.5 µm. e) Deformed specimen (minimum σ_1 = 0.4 MPa, ε_{total}= 12.1%, duration 9.4d). d = 16.9 ± 3.4 µm. Numerous curved boundaries (e.g., black arrow) indicate a growth texture. Several cuspate boundaries are evident (gray arrows). f) Thermal specimen. Note that the magnification in this image is half that in panel (e). d = 20.1 ± 3.2 µm. Numerous, highly curved grain boundaries are visible. Some boundaries exhibit cusps (black arrow). Frost, accumulated during microscopy, forms dark blots on the surface (gray arrow). Scratches from the microtome blade cross the image from left to right.

(e.g., black arrow, Fig. 4e). A few cuspate boundaries are observed, suggesting pinning of the boundaries in some locations (gray arrow, Fig. 4e). The thermal specimen for the same experiment also shows highly curved boundaries, convex-out small grains, concave-in large grains, and slight cusps on some grain boundaries (black arrow, Fig. 4f).

Though GBS in ice is geometrically accommodated by the glide of basal dislocations, the microstructures of our deformed samples show very little—to first order, none—formation of low-angle (subgrain) boundaries. This is consistent with the dearth of subgrain boundaries seen in EBSD data from specimens deformed in the same rheological regime (Caswell et al., 2015).

Grain size in all samples is indicated by Fig. 5, which differentiates the experiments according to the theory articulated in Section 2 and divides the data according to whether or not growth was expected to occur in the deformed specimen for that experiment. This division will be discussed at length in the following section, but it is immediately clear in Fig. 5 that when growth is not expected to occur – that is, the dissipation rate by GBS is higher than that by grain growth – the grain size of the deformed specimen is similar to that of the starting material, while the thermal specimen exhibits markedly increased grain size.

The grain size of thermal specimens is consistent with normal grain growth. Figure 6 shows the quantity d^2-d_o^2 vs t for the thermal specimens. The data fall into two sets, both fit by Eq. 2 but with different values of the grain growth constant, K. The first set, consisting of the fine-grained specimens, exhibits somewhat sluggish grain growth. This behavior is demonstrated in Fig. 6b, where data from our fine-grained thermal

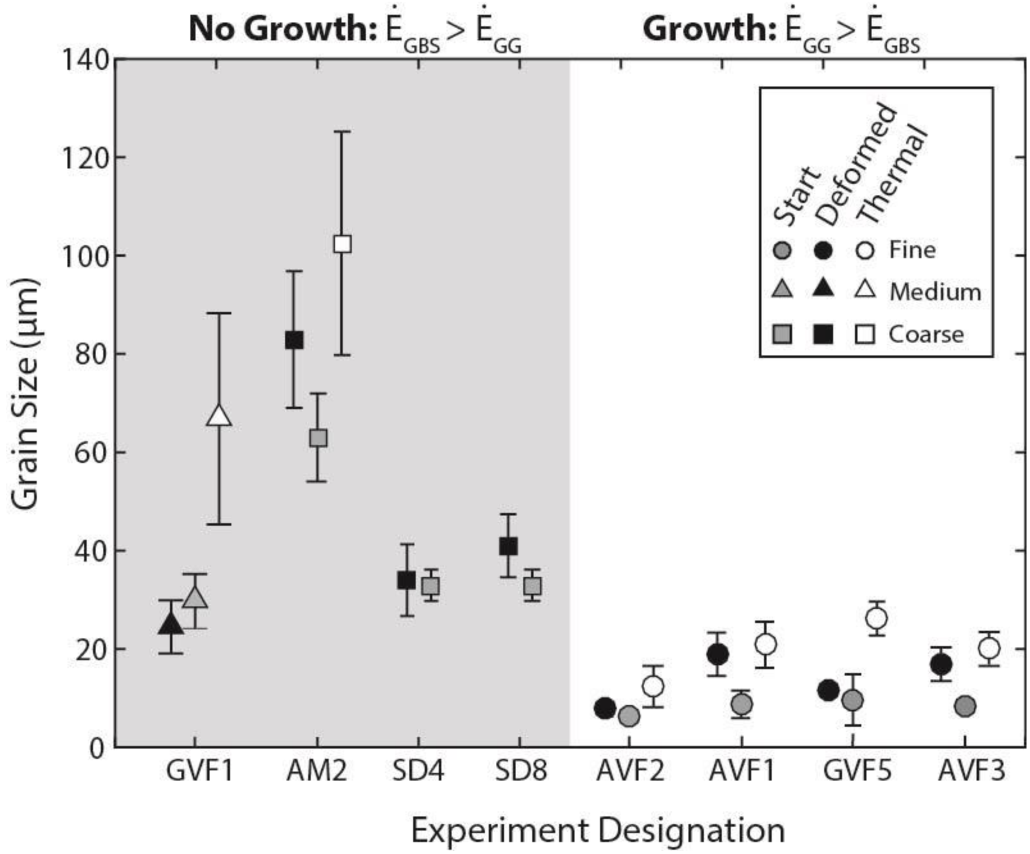

Figure 5: Grain sizes of all specimens. The experiments are divided into two groups: the four experiments on the left are those in which the deformed specimen was subjected to conditions such that the dissipation rate due to creep exceeded that due to grain growth, and therefore no grain growth was expected to occur. The experiments on the right were conducted under conditions favoring grain growth in the deformed specimen. Specimen symbols for each experiment are offset for clarity.

specimens are best fit by Eq. 2 with K = 5×10^{-16} m^2 s^{-1} (dotted line). The "grow" specimen from experiment GVF5, indicated by a diamond in Fig. 6, follows this trend. This growth constant is somewhat low relative to that expected for bubble-free ice based on the grain growth data of Arena et al. (1997). A fit to those authors' low-temperature data yields K_o = 8.9×10^{-7} m^2 s^{-1} and Q = 39 kJ/mol, predicting a value of K = 2.9×10^{-15} m^2 s^{-1} at our experimental conditions. The value that best-fits our experiments is instead comparable to that reported by Arena et al. (1997) for ice with a small concentration of bubbles, $K \approx 4\times10^{-16}$ m^2 s^{-1}. Though no bubbles are readily apparent in the microstructural study of our specimens, we do note that some grain boundaries in the thermal samples exhibit evidence of pinning (e.g., Fig. 4c). A small concentration of extremely small bubbles along grain boundaries, perhaps remnant from the sample fabrication process, may therefore be the source of the sluggish grain growth observed in the fine-grained thermal specimens.

The second group of thermal specimens in Fig. 6a consists of those from coarser-grained experiments. While sparse, the data for these specimens yield individual values of K = 2.8×10^{-15} m^2 s^{-1} for experiment GVF1 and K = 1.5×10^{-15} m^2 s^{-1} for experiment AM2, both highly consistent with the value predicted from the data for bubble-free ice (Arena et al., 1997). These specimens are therefore considered to be completely bubble-free.

5. Discussion

The deformed specimens exhibit microstructures and rheology consistent with grain boundary sliding that is rate-limited by the boundary viscosity. Evidence for GBS includes the low stress exponent (n = 1.6), consistent with the composite rheology of Goldsby & Kohlstedt (2001), and microstructures evincing straight grain boundaries and

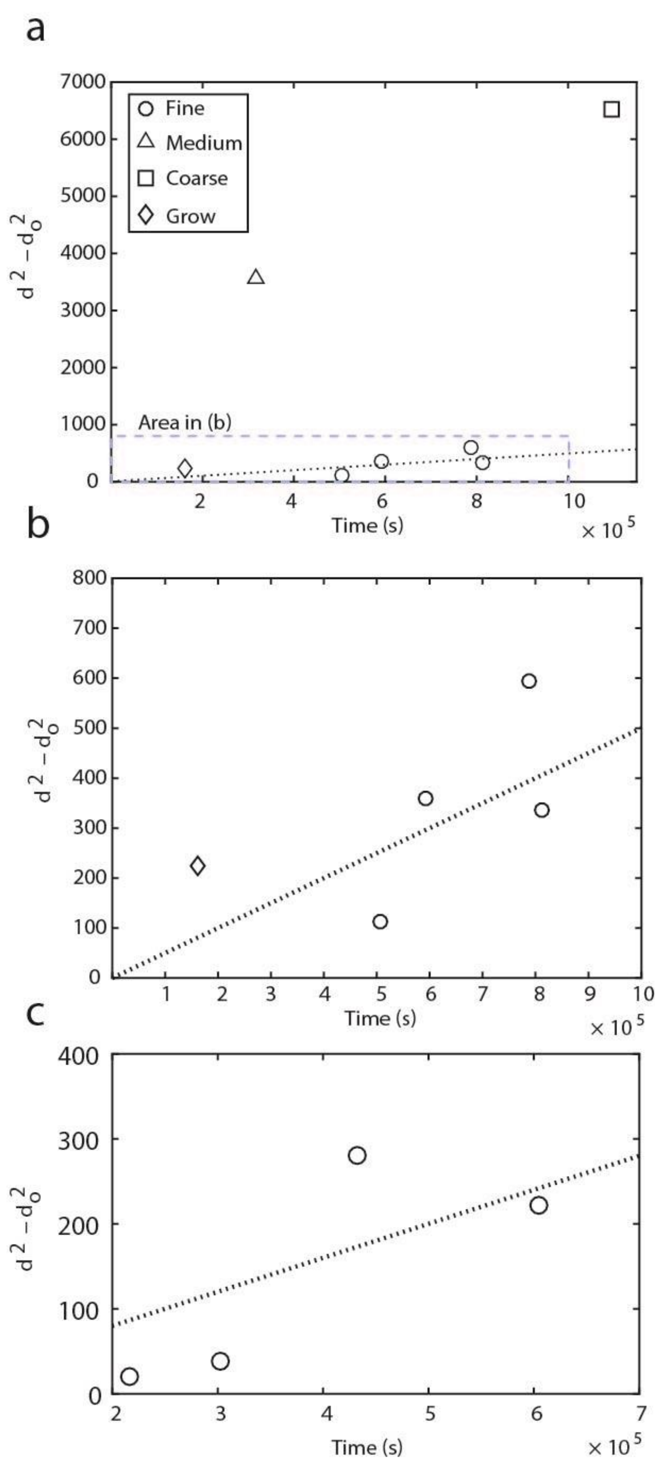

Figure 6: a) Grain growth in thermal specimens. Two trends are observed, indicating different grain growth kinetics for our fine-grained specimens relative to our medium- and coarse-grained specimens. For our fine-grained specimens, shown in (b), the fit to Eq. (3), with $K = 5\times10^{-16}$ m^2s^{-1} is shown as a dotted line. c) Grain growth in deformed specimens conducted under conditions in which the energy dissipation rate via growth exceeds that via GSS creep. Growth of these specimens produces an average grain growth constant $K = 1\times10^{-16}$ m^2s^{-1} (dotted line), which is similar to that observed for thermal samples from the same experiments.

numerous four-grain junctions considered diagnostic of grain switching events during GBS (Ashby & Verrall, 1973; Goldsby & Kohlstedt, 1997; Langdon, 1991). Thus, the rheological behavior is consistent with flow sensitive to chemical potential gradients on the grain boundary, granting license to apply the energy dissipation rate model articulated in Section 2.

Figure 7 schematically evaluates our experimental conditions with respect to the model. Dissipation by grain growth (Eq. 4) is indicated at two values of K (1×10^{-16} m^2s^{-1}, solid black line, and 1×10^{-15} m^2 s^{-1}, dashed black line) and compared to calculated dissipation rates by creep (Eq.'s 6 and 7, GSS creep rate-limited by sliding on the boundaries, with n = 1.8 and p = 1.4). Dissipation rates for experimental data are calculated via Eq. (6), using applied deviatoric stress and observed steady-state strain rates.

Upon inspection of Fig. 7, it is clear that our experimental data fall into two groups: one in which the rate of energy dissipation by grain growth exceeds that for creep, and the other in which the opposite hierarchy exists. This is by design, in order to evaluate the model we have articulated; grain growth is expected to occur in one group and not the other. The first group includes coarser specimens subjected to loading conditions under which the energy dissipation rate via GSS creep is greater than that by grain growth. Grain growth is expected to be suppressed in these deforming specimen and, returning to Fig. 5, we see that this group (which includes experiments coded GVF1, AM2, SD4 and SD8) corresponds exactly to those observed to have suppressed grain growth. The best example of this behavior is experiment GVF1, for which the deformed specimen and starting material have nearly identical grain size (see Fig. 5) while the

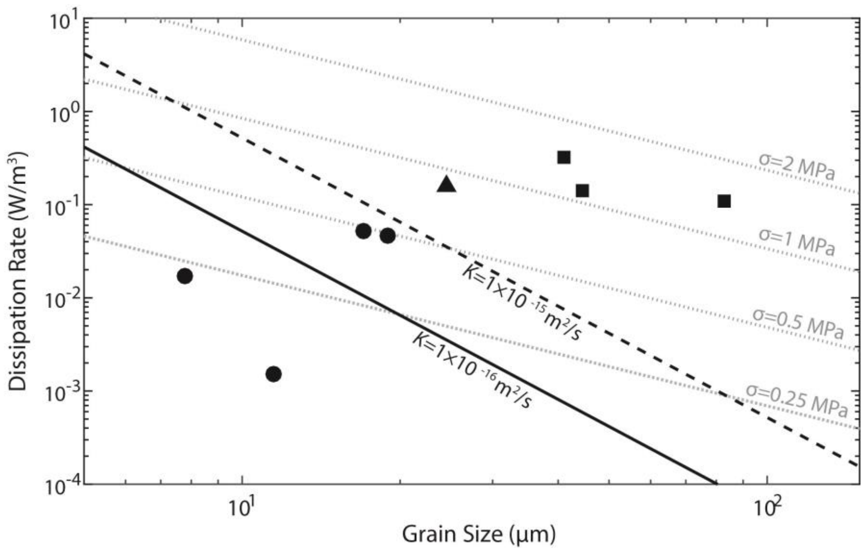

Figure 7: Comparison of dissipation rates by GBS-effected creep (gray lines, Eq. 6) and grain growth (heavy line, Eq. 4) as a function of grain size. Creep dissipation curves are based on "GBS-accommodated basal slip" – i.e., the regime of GBS rate-limited by the grain boundary viscosity, with n = 1.8, as articulated by Goldsby and Kohlstedt (2001). The magnitude of deviatoric stress for each creep dissipation line is given at right. Grain growth dissipation assumes growth for 1 s, essentially maximizing its effect, and employs γ_{GB} = 0.065 J m^{-2}. As in previous figures, squares indicate "Coarse," triangles "Medium," and circles "Fine" specimens.

thermal specimen, which was subjected to identical time-temperature conditions as the deformed specimen, has a final grain size consistent with normal grain growth as described in the results (Arena et al., 1997). Though a thermal specimen was not available for comparison following experiment SD4, this set provides a compelling case for suppressed grain growth: in this case the deformed and starting specimens have essentially identical grain sizes despite an experiment lasting nearly 11 days. By comparison, applying Eq. (2) with a grain growth constant appropriate to thermal specimens in similar experiments [$K = 2.9\times10^{-15}$ m^2 s^{-1} per Arena et al. (1997)] yields a predicted grain size of 110 μm. Similarly, a thermal specimen for experiment SD8 would have a grain size of 70 μm. Thus, in the regime where the dissipation rate by GSS creep exceeds that by grain growth, the grains do not grow.

We acknowledge that the deformed specimen for experiment AM2 exhibits a grain size between that of the starting material and thermal specimen. Applying the value of K obtained for the thermal specimen in this experiment to Eq. (2) indicates that 5.6 days of growth at 240K would be required to produce the observed change in grain size. This time is much shorter than the duration of the experiment, which was nearly 13 days, but too long to be explained by transient load alleviations during the experiment due to, e.g., icing of the apparatus piston. It therefore is unlikely that this growth occurred during the course of the experiment. Similarly, only 0.3 μm of growth would be expected during the ~10 minutes that the specimen was in the -17°C environment of the cold room during microstructure analysis. The discrepancy in grain size is therefore attributed to heterogeneity in the starting material. Though the deformed specimen shows increased grain size relative to the starting material, the thermal specimen exhibits much larger grain size than either, indicating that, regardless of the exact initial grain size in the deformed specimen, growth was clearly inhibited.

The second group of deformed specimens consists of those from experiments conducted under conditions designed to promote grain growth. In these experiments, the predicted dissipation rate due to grain growth exceeds that by GSS creep. This group is indicated by Fig. 5, which demonstrates that growth occurred in each of the deformed specimens within this group. Notably, the deformed specimens in experiments AVF1 and AVF3 possess grain sizes only slightly smaller than that in the corresponding thermal history specimens, indicating that grain growth was uninhibited as these specimens deformed.

To evaluate the grain growth constant, *K*, for this group of specimens we must consider the appropriate value of time to input into Eq. 2. It is well-established that chemical potential gradients along grain boundaries evolve during transient creep, relaxing from elastically induced peaks at the onset of loading to the parabolic distribution required for steady-state (Raj, 1975). It is the diminishment of chemical potential gradients with increasing time during this evolution that gives rise to the decelerating transient in primary creep (Gribb & Cooper, 1998; Raj, 1975). Though this model was explicitly articulated for materials deforming via diffusion creep, the stress reduction data of Caswell et al. (2015) and the linearity of attenuation in ice (Chapter 4), both measured in the regime of GBS rate-limited by sliding on the boundary, indicate that similar diffusional processes occur during the transient phase of GBS rate-limited by the boundary viscosity. With regard to the model articulated in Section 2, the evolution of chemical potential gradients during transient creep can lead to a switch in regimes, from dominance of a chemical potential gradient favoring creep to one favoring grain growth. Interestingly, the point at which grain growth begins to occur in our specimens is not well-correlated with the point at which the rate of macroscopic dissipation due to deformation (Eq. 6) drops below that by grain growth (Eq. 4). Analysis of mechanical data from the experiments indicates that the experiments reach these conditions by (or at) a strain of 0.5%, but fitting to Eq. 2 with elapsed time after $\varepsilon = 0.005$ produces a poor fit ($R^2 = 0.14$). Instead, fitting Eq. 2 using the approximate duration of steady-state creep produces a value of $K = 1\times10^{-16}$ m^2s^{-1} ($R^2 = 0.546$), a value strikingly similar to that calculated for the thermal specimens from the same group of experiments. This result indicates that the chemical potential gradients driving the evolution of grain boundary tractions exceed those driving grain growth until the specimen is at (or near) steady-state.

The model articulated in Section 2 can be applied to scrutinize data (and the interpretation thereof) for grain growth in fine-grained aggregates of San Carlos, AZ, olivine deforming via diffusion creep (Karato et al., 1986). These authors' experiments were conducted on hot-pressed olivine aggregates of grain sizes 5-90 μm specifically to investigate the roles of grain size and water content on diffusion creep of olivine. Citing time-dependent strengthening observed in many – but not all – of their experiments, the authors concluded that grain growth was not affected by deformation and that grain growth was independent of a grain size-sensitive viscosity. Karato et al. (1986) noted, however – and demonstrated by their Fig. 4 – that under identical experimental conditions, their finest-grained (11-30 μm) aggregates experienced time-dependent strengthening while a moderately coarser specimen (67 μm) did not. Although the stress and grain size conditions of their experiments do straddle the recrystallized grain size piezometer (Shimizu, 1998), the total accumulated strain (<20%) is insufficient for recrystallization to control grain size (Bystricky et al., 2000; Piazolo et al., 2013). In addition, the mechanical data provided by Karato et al. for the coarser-grained experiment show no weakening indicative of dynamic recrystallization. Consideration of the data relative to the model proposed here provides an explanation for the apparent discrepancy. By applying Eq.'s. (4) and (6) with γ_{GB} = 0.9 J m^{-2} (Cooper & Kohlstedt, 1982) and K = 7.8×10^{14} m^2 s^{-1} (Karato, 1989), one sees that, at the conditions of the experiments in question (T = 1300ºC, $\dot{\varepsilon}$ =10^{-5} s^{-1}), the finest-grain-sized aggregates produce an energy dissipation rate by grain growth nearly identical to that for creep (for σ = 10 MPa, based on Karato's mechanical data), while in the case of the 65-μm aggregates, the dissipation rate by creep (σ = 60 MPa) exceeds that by grain growth by approximately two orders of magnitude. Thus, our model predicts that their finest-grained specimens would exhibit grain growth while the coarser specimen would not.

The model can also be applied to the data of Durham et al. (2001), who studied GSS flow in ice at low temperatures (i.e., ~220K) and elevated confining pressure (P~50 MPa). These authors observed very little grain growth in their specimens, consistent with observations made by Goldsby & Kohlstedt (1997) and with the model articulated here. Applying the model in Section 2, only one of their experiments – that with the finest grain size and lowest strain rate – falls near the boundary between dissipation rates in Fig. 7; in all others, grain growth should have been suppressed. Indeed, the authors note that the experiment whose conditions resulted in comparable dissipation rates for creep and growth (their code 420) showed a slight increase in grain size relative to the starting material, but no indication of time-dependent strengthening (i.e., grain growth) during the course of the experiment. The authors did observe strengthening in a small, additional subset of their samples, but the interpretation thereof is nebulous. Although they attributed the observed strengthening to grain growth, they were unable to derive realistic grain growth constants when fitting their data to Eq.'s (2) and (7). Furthermore, the microstructures of the strengthened samples exhibited substantial irregularities, including signs of dislocation creep and grain aspect ratios of 50:1, indicative of abnormal grain growth during the ice I-II phase transition as the samples were fabricated (Bennett et al., 1997; Stern et al., 1997). These microstructures indicate that rather than strengthening due to grain growth, strengthening in these specimens was associated with strong fabric caused by abnormal grain growth during specimen fabrication. For samples without abnormal fabric, Durham et al. (2001)'s results are fully in keeping with the model articulated here.

To rule out mechanisms of grain size pinning, we conducted the "grow" experiment to evaluate whether voids created during the process of grain boundary sliding itself might affect our results. Grain boundary sliding has the potential to cause cavitation at steps and facets on grain boundaries (Sutton & Balluffi, 1995, p. 786), and such voids could inhibit grain boundary mobility. The "grow" specimen, however, refutes this possibility: this specimen, which was annealed following deformation that would have produced grain boundary voids, exhibited grain growth consistent with the thermal specimens in other experiments (Fig. 6b). Though we cannot say for certain whether voids were produced because they may be smaller than the resolution of our microstructural observations, the behavior of the "Grow" specimen indicates that even if they are present, voids produced by GBS did not pin the grain boundaries in our samples.

It is additionally possible that grain growth may be slowed by the effect of deformation on grain boundary energy. Low-energy boundaries are created when the relative orientations of grains on either side of the boundary produce a high-density coincident site lattice (CSL) (Sutton & Balluffi, 1995, p. 385). Previous work has shown that low-energy boundary configurations can be produced by deformation in ice; Hondoh & Higashi (1978) observed, via x-ray diffraction of boundaries between ice bicrystals subject to load, that the structure of the boundary evolved into "facets" with CSL orientations. The process of faceting is thought to play a first-order role in the grain boundary viscosity of ice deforming via GBS (Caswell et al., 2015). Thus, it is possible that deviatoric stress-induced faceting of the grain boundaries in our specimens reduces the driving force for grain boundary migration by reducing the magnitude of local grain boundary energy. However, even a reduced driving force would still lead to grain growth, as differences in curvature and, thus, chemical potential differences still exist across the boundary. The complete lack of grain growth seen in our longest experiments suggests that grain growth is not simply slowed during GSS creep, but halted altogether when the rate of dissipation by creep exceeds that by grain growth.

5.1. Geophysical Implications

Because the rheology of ice is grain size-sensitive when deforming via boundary sliding-limited GBS, inhibiting grain growth restrains time-dependent strengthening. Our results suggest that when polycrystalline ice deforms via boundary sliding-limited GBS, grain size will remain constant until either a) deviatoric stress ceases, allowing grain growth to become the most effective energy dissipation process, or b) the deviatoric stress increases such that dislocation creep once again becomes the dominant mechanism, potentially leading to grain size reduction—and subsequent softening—by dynamic recrystallization.

Our results therefore carry implications for settings in which rheological weakening has occurred by dynamic recrystallization. Evidence from experiments and nature indicates that shear localization and seismic slip can produce zones of dynamically recrystallized grains (i.e., mylonites) throughout the mantle and lithosphere (Bestmann et al., 2012; Karato & Wu, 1993; Kim et al., 2010; Smith et al., 2013; Verberne et al., 2014; Warren & Hirth, 2006). Such recrystallized zones may produce rheological weakening of the lithosphere (Rutter & Brodie, 1988), but an oft-cited criticism of models invoking this mechanism of weakening is that grain growth in the mylonitized zone limits the lifetime of weakening. Balancing growth and recrystallization then leads to the "field boundary approach" (De Bresser et al., 2001). Some authors evoke an inhibiting process to constrain grain growth; for example, Warren & Hirth (2006) suggested that permanent grain size reduction is possible due to second-phase pinning in peridotite mylonites. Our results, however, suggest that if the recrystallized grain size is sufficiently small to cause a switch to GSS rheology and the deviatoric stress is sufficient to maintain energy dissipation via GSS creep at a rate higher than that which would be produced by grain growth, the resulting zones of weakness will persist without the need for a pinning process.

The possibility of maintaining a fine grain size without second-phase pinning has profound implications for the tectonics of icy worlds and the deformation of terrestrial glaciers and ice sheets. In these settings, any stress concentration that produces a local grain size reduction sufficient to cause a switch to GSS deformation has thereby produced a zone of rheological weakness. As long as the ice continues to deform by GSS creep, this zone of weakness will persist indefinitely – a potential means of localizing strain at the margins of fast-moving ice streams or at the base of an icy satellite's lithosphere.

In particular, our results are directly applicable to the marginal zones of fast-moving Antarctic ice streams. Low basal drag due to weak basal till (Joughin et al., 2004; Kamb, 2001; Tulacyk et al, 2001) means that the margins are critical in the force balance controlling ice stream motion; shear stresses at margins may provide as much as 93% of the force resisting downstream driving stresses (Echelmeyer et al., 1994; Whillans & van der Veen, 1997). The majority of strain associated with ice stream flow is thus produced at the margins (Bindschadler & Scambos, 1991; Joughin et al., 2002). Marginal ice appears to be very soft in some cases; to match a measured velocity profile across the margin of Whillans Ice Stream (Ice Stream B), Echelmeyer et al. (1994) suggested that ice within the margin is ten-times weaker than that in the central part of the ice stream, though this may apply only to the region of the profile measured by (Echelmeyer et al., 1994) and may represent an extreme datum of variable ice rheology along the margins of Ice Stream B (Joughin et al., 2004). Many authors, including *Echelmeyer et al.* (1994), attributed such softness to shear heating and potential meltwater generation (Perol & Rice, 2015; Suckale et al., 2014), though Cuffey et al. (2000) point out that such enhancement is also possible by a combination of fabric development and grain size-sensitive flow. Our results suggest that it is indeed possible for grain size-sensitive flow to sustain areas of rheological weakness along ice stream margins.

The results also affect estimates of grain size in a convecting ice shell. Barr & McKinnon (2007) assumed that the dislocation component of GBS in ice was sufficient to drive dynamic recrystallization, concluding that the maximum equilibrium grain size within an ice shell is 1-10 mm. Our results and those of Caswell et al. (2015) indicate that this model does not accurately capture the mechanics of grain size evolution within an ice shell. Instead, the field boundary approach may be used to estimate initial grain size in a convecting ice shell. Such an estimate was carried out by Barr & Pappalardo (2005) who calculated, using the grain size-sensitive rheology of Goldsby & Kohlstedt (2001), that convection would not initiate within an icy Galilean satellite if initial deformation occurred by dislocation creep—i.e., for a grain size exceeding 2 cm. Using this estimate as the maximum initial grain size in a convecting ice shell at –8 ºC (265K) (Tobie et al., 2003), an initially coarse grain size (d ~ 2 cm) would not experience substantial change in grain size at a convective stress of ≤ 100 kPa. The surfaces of many icy moons are pervasively fractured, however, and the surface of Europa exhibits evidence for kilometers of displacement along strike-slip faults (Hoppa et al., 2000; Francis Nimmo & Gaidos, 2002; Tufts et al., 1999). Analogous terrestrial faults, such as the San Andreas, exhibit localized shear to the bottom of the mantle lithosphere (Ford et al., 2014), and fault slip produces recrystallization in experiments and natural settings (Bestmann et al., 2012; Smith et al., 2013). Thus, propagation of tectonic stresses to the base of an icy lithosphere may produce geologically long-lived regions of fine grain size.

6. Conclusion

Simultaneous creep and annealing experiments have shown that when ice deforms via steady-state grain size-sensitive creep, grain growth is inhibited when the dissipation rate by grain size-sensitive creep exceeds that due to grain growth. Whether or not grain growth occurs can be predicted by calculating the steady-state dissipation rates for each mechanism, presented in Section 2. When the dissipation rate by creep exceeds that by grain growth, the latter will not occur. These conditions are met for most geophysically relevant grain sizes, meaning that grain growth is expected to be suppressed in the convecting interior of an icy satellite in the outer solar system or in localized shear zones at the margins of fast-moving ice streams.

Table 1: Grain sizes, anticipated dissipation rates by grain growth (Eq. 4) and GBS creep (Eq. 6), and grain growth predictions for each experiment in this study.

Experiment Code	Grain Size Starting (µm)	Grain Size Deformed (µm)	Grain Size Thermal (µm)	$\dot{E}_{GG}$ + (J m^{-3})	$\dot{E}_{GBS}$ † (J m^{-3})	Growth Expected?
GVF1	29.9±5.4	24.5±5.4	66.8±21.5	0.0292	0.2600	N
AM2	63.0±9.0	82.9±13.9	102.5±22.7	0.0031	0.0108	N
SD4*	33±3.2	34±7.3	N/A	0.0217	0.1434	N
SD8*	33±3.2	41±6.4	N/A	0.0217	0.3240	N
AVF2	6.4±1.6	7.8±1.6	12.4±4.2	2.9750	0.0210	Y
AVF1	8.7±2.8	18.9±4.4	20.8±4.7	0.1155	0.0440	Y
GVF5	9.7±5.2	11.5±2.0	26.2±3.4	0.8546	0.0015	Y
AVF3	8.2±0.5	16.9±3.4	20.1±3.3	1.4145	0.0520	Y

* Starting grain size for experiments SD4 and SD8 are from a separate but identically-fabricated specimen.

+ Calculated using Eq. 4, the starting grain size given here, and $K = 1\times10^{-15}$ m^2 s^{-1}.

† Minimum value for any experiments with multiple load steps. Calculated using Eq. 6 and the steady-state stress/strain rate pairs shown in Fig. 3.

References

Alley, R. B., & Joughin, I. (2012). Modeling Ice-Sheet Flow. *Science*, *336*(6081), 551–552. https://doi.org/10.1126/science.1220530

Alley, R. B., Gow, A. J., & Meese, D. A. (1995). Mapping c-axis fabrics to study physical processes in ice. *Journal of Glaciology*, *41*(137), 197–203.

Arena, L., Nasello, O. B., & Levi, L. (1997). Effect of Bubbles on grain Growth in Ice. *Journal of Physical Chemistry B*, *101*(32), 6109–6112. https://doi.org/10.1021/jp9632394

Ashby, M. F., & Verrall, R. A. (1973). Diffusion-accommodated flow and superplasticity. *Acta Metallurgica*, *21*, 149–163.

Austin, N., & Evans, B. (2007). Paleowattmeters: A scaling relation for dynamically recrystallized grain size. *Geology*, 343–346.

Barr, A. C., & McKinnon, W. B. (2007). Convection in ice I shells and mantles with self-consistent grain size. *Journal of Geophysical Research*, *112*(E2). https://doi.org/10.1029/2006JE002781

Barr, A. C., & Pappalardo, R. T. (2005). Onset of convection in the icy Galilean satellites: Influence of rheology. *Journal of Geophysical Research*, *110*(E12). https://doi.org/10.1029/2004JE002371

Barr, A. C., & Showman, A. P. (2009). Heat transfer in Europa's icy shell. *Europa, Edited by RT Pappalardo, WB McKinnon, and KK Khurana, University of Arizona Press, Tucson*, 405–430.

Baum, W. A., Kreidl, T., Westphal, J. A., Danielson, G. E., Seidelmann, P. K., Pascu, D., & Currie, D. G. (1981). Saturn's E ring: I. CCD observations of March 1980. *Icarus*, *47*(1), 84–96.

Bennett, K., Wenk, H. R., Durham, W. B., Stern, L. A., & Kirby, S. H. (1997). Preferred crystallographic orientation in the ice I ← II transformation and the flow of ice II. *Philosophical Magazine A*, *76*(2), 413–435. https://doi.org/10.1080/01418619708209983

Bestmann, M., Pennacchioni, G., Nielsen, S., Göken, M., & de Wall, H. (2012). Deformation and ultrafine dynamic recrystallization of quartz in pseudotachylyte-bearing brittle faults: A matter of a few seconds. *Journal of Structural Geology*, *38*, 21–38. https://doi.org/10.1016/j.jsg.2011.10.001

Billings, S. E., & Kattenhorn, S. A. (2005). The great thickness debate: Ice shell thickness models for Europa and comparisons with estimates based on flexure at ridges. *Icarus*, *177*(2), 397–412. https://doi.org/10.1016/j.icarus.2005.03.013

Bindschadler, R. A., & Scambos, T. A. (1991). Satellite-image-derived velocity field of an Antarctic ice stream. *Science*, *252*(5003), 242–246.

Bystricky, M., Kunze, K., Burlini, L., & Burg, J.-P. (2000). High shear strain of olivine aggregates: Rheological and seismic consequences. *Science*, *290*(5496), 1564–1567.

Caswell, T. E., Cooper, R. F., & Goldsby, D. L. (2015). The constant-hardness creep compliance of polycrystalline ice. *Geophysical Research Letters*, *42*. https://doi.org/10.1002/2015GL064666

Clark, R. N. (1981). Water frost and ice: The near-infrared spectral reflectance 0.65-2.5 um. *Journal of Geophysical Research*, *86*(B4), 3087–3096.

Clark, R. N., Fanale, F. P., & Zent, A. P. (1983). Frost grain size metamorphism: Implications for remote sensing of planetary surfaces. *Icarus*, *56*, 233–245.

Collins, G. C., McKinnon, W. B., Moore, J. M., Nimmo, F., Pappalardo, R. T., Prockter, L. M., & Schenk, P. M. (2009). Tectonics of the outer planet satellites. *Planetary Tectonics*, *11*, 264.

Cooper, R. F., & Kohlstedt, D. L. (1982). Interfacial Energies in the Olivine-Basalt System. *Advances in Earth and Planetary Science*, *12*, 217–228. https://doi.org/10.1007/978-94-009-7867-6_17

Cuffey, K. M., Thorsteinsson, T., & Waddington, E. D. (2000). A renewed argument for crystal size control of ice sheet strain rates. *Journal of Geophysical Research*, *105*(B12), 27889–27894.

De Bresser, J., Ter Heege, J., & Spiers, C. (2001). Grain size reduction by dynamic recrystallization: can it result in major rheological weakening? *International Journal of Earth Sciences*, *90*(1), 28–45. https://doi.org/10.1007/s005310000149

Deblonde, G., & Peltier, W. R. (1991). Delonde & Peltier (1991) Continental Ice Sheet Growth Sims_JGR.pdf. *Journal of Geophysical Research*, *96*(D5), 9189–9215.

Druetta, E., Nasello, O. B., & Prinzio, C. L. D. (2013). Experimental Determination of <1010>/phi Tilt Grain Boundary Energies in Ice. *Journal of Materials Science Research*, *3*(1). https://doi.org/10.5539/jmsr.v3n1p69

Durham, W. B., Stern, L. A., & Kirby, S. H. (2001). Rheology of ice I at low stress and elevated confining pressure. *Journal of Geophysical Research*, *106*(6), 11031–11042.

Echelmeyer, K. A., Harrison, W. D., Larsen, C., & Mitchell, J. E. (1994). The role of the margins in the dynamics of an active ice stream. *Journal of Glaciology*, *40*(136), 527–538. https://doi.org/10.1017/S0022143000012417

Exner, H. E. (1972). Analysis of grain- and particle-size distributions in metallic materials. *International Metallurgical Reviews*, *17*(1), 25–42.

Feltham, P. (1957). Grain growth in metals. *Acta Metallurgica*, *5*(2), 97–105.

Ford, H. A., Fischer, K. M., & Lekic, V. (2014). Localized shear in the deep lithosphere beneath the San Andreas fault system. *Geology*, *42*(4), 295–298. https://doi.org/10.1130/G35128.1

Gasson, E., DeConto, R. M., Pollard, D., & Levy, R. H. (2016). Dynamic Antarctic ice sheet during the early to mid-Miocene. *Proceedings of the National Academy of Sciences*, *113*(13), 3459–3464. https://doi.org/10.1073/pnas.1516130113

Goldsby, D. L., & Kohlstedt, D. L. (1997). Grain boundary sliding in fine-grained ice I. *Scripta Materialia*, *37*(9), 1399–1406.

Goldsby, D. L., & Kohlstedt, D. L. (2001). Superplastic deformation of ice: Experimental observations. *Journal of Geophysical Research: Solid Earth*, *106*(B6), 11017–11030. https://doi.org/10.1029/2000JB900336

Gow, A. J. (1969). On the rates of growth of grains and crystals in south polar firn. *Journal of Glaciology*, *8*(53), 241–252.

Gribb, T. T., & Cooper, R. F. (1998). Low-frequency shear attenuation in polycrystalline olivine: Grain boundary diffusion and the physical significance of the Andrade model for viscoelastic rheology. *Journal of Geophysical Research*, *103*(B11), 27267–27279.

Herring, C. (1950). Diffusional Viscosity of a Polycrystalline Solid. *Journal of Applied Physics*, *21*(5), 437–445. https://doi.org/10.1063/1.1699681

Hillert, M. (1965). On the theory of normal and abnormal grain growth. *Acta Metallurgica*, *13*(3), 227–238.

Hondoh, T., & Higashi, A. (1978). X-ray diffraction topographic observations of the large-angle grain boundary in ice under deformation. *Journal of Glaciology*, *21*(85), 629–638.

Hoppa, G., Greenberg, R., Tufts, B. R., Geissler, P., Phillips, C., & Milazzo, M. (2000). Distribution of strike-slip faults on Europa. *Journal of Geophysical Research*, *105*(E9), 22617–22627.

Joughin, I., Tulaczyk, S., Bindschadler, R., & Price, S. F. (2002). Changes in west Antarctic ice stream velocities: Observation and analysis. *Journal of Geophysical Research: Solid Earth*, *107*(B11), EPM 3-1-EPM 3-22. https://doi.org/10.1029/2001JB001029

Joughin, I., MacAyeal, D., & Tulaczyk, S. (2004). Basal shear stress of the Ross ice streams from control method inversions. *Journal of Geophysical Research*, *109*(B09405).

Karato, S. (1989). Grain growth kinetics in olivine aggregates. *Tectonophysics*, *168*, 255–273.

Karato, Shun-ichiro, & Wu, P. (1993). Rheology of the upper mantle: a synthesis. *Science*, *260*(5109), 771–778.

Karato, S.-I., Paterson, M. S., & FitzGerald, J. D. (1986). Rheology of Synthetic Olivine Aggregates: Influence of Grain Size and Water. *Journal of Geophysical Research*, *91*(B8), 8151–8176.

Kattenhorn, S. A., & Prockter, L. M. (2014). Evidence for subduction in the ice shell of Europa. *Nature Geoscience*, *7*(10), 762–767. https://doi.org/10.1038/ngeo2245

Kempf, S., Beckmann, U., & Schmidt, J. (2010). How the Enceladus dust plume feeds Saturn's E ring. *Icarus*, *206*(2), 446–457. https://doi.org/10.1016/j.icarus.2009.09.016

Ketcham, W. M., & Hobbs, P. V. (1969). An Experimental Determination of the Surface Energies of Ice. *Philosophical Magazine*, *19*, 1161–1173.

Kim, J.-W., Ree, J.-H., Han, R., & Shimamoto, T. (2010). Experimental evidence for the simultaneous formation of pseudotachylyte and mylonite in the brittle regime. *Geology*, *38*(12), 1143–1146.

Kondepudi, D., & Prigogine, I. (1998). *Modern Thermodynamics: From Heat Engines to Dissipative Structures*. Hoboken, NJ: John Wiley.

Langdon, T. G. (1991). The physics of superplastic deformation. *Materials Science and Engineering*, *A137*, 1–11.

McCarthy, C., & Cooper, R. F. (2016). Tidal dissipation in creeping ice and the thermal evolution of Europa. *Earth and Planetary Science Letters*, *443*, 185–194. https://doi.org/10.1016/j.epsl.2016.03.006

Nimmo, F., Giese, B., & Pappalardo, R. T. (2003). Estimates of Europa's ice shell thickness from elastically-supported topography: EUROPAN ICE SHELL THICKNESS FROM FLEXURE. *Geophysical Research Letters*, *30*(5), n/a-n/a. https://doi.org/10.1029/2002GL016660

Nimmo, Francis, & Gaidos, E. (2002). Strike-slip motion and double ridge formation on Europa. *Journal of Geophysical Research*, *107*(E4). https://doi.org/10.1029/2000JE001476

Ojakangas, G. W., & Stevenson, D. J. (1989). Thermal state of an ice shell on Europa. *Icarus*, *81*(2), 220–241.

Pappalardo, R. T., Head, J. W., Greeley, R., Sullivan, R., Pilcher, C., Schubert, G., … Goldsby, D. L. (1998). Geological evidence for solid-state convection in Europa's ice shell. *Nature*, *391*. Retrieved from http://www.planetary.brown.edu/pdfs/1874.pdf

Perol, T., & Rice, J. R. (2015). Shear heating and weakening of the margins of West Antarctic ice streams. *Geophysical Research Letters*, *42*(9), 3406–3413. https://doi.org/10.1002/2015GL063638

Pettit, E. C., Waddington, E. D., Harrison, W. D., Thorsteinsson, T., Elsberg, D., Morack, J., & Zumberge, M. A. (2011). The crossover stress, anisotropy and the ice flow law at Siple Dome, West Antarctica. *Journal of Glaciology*, *57*(201), 39–52.

Piazolo, S., Wilson, C. J. L., Luzin, V., Brouzet, C., & Peternell, M. (2013). Dynamics of ice mass deformation: Linking processes to rheology, texture, and microstructure: Dynamics of Ice Mass Deformation. *Geochemistry, Geophysics, Geosystems*, *14*(10), 4185–4194. https://doi.org/10.1002/ggge.20246

Poirier, J.-P. (1985). *Creep of Crystals*. Cambridge University Press.

Pollard, D., & DeConto, R. M. (2009). Modelling West Antarctic ice sheet growth and collapse through the past five million years. *Nature*, *458*(7236), 329–332. https://doi.org/10.1038/nature07809

Porco, C. C., Helfenstein, P., Thomas, P. C., Ingersoll, A. P., Wisdom, J., West, R., … others. (2006). Cassini observes the active south pole of Enceladus. *Science*, *311*(5766), 1393–1401.

Porco, C., DiNino, D., & Nimmo, F. (2014). How the geysers, tidal stresses, and thermal emission across the south polar terrain of Enceladus are related. *The Astronomical Journal*, *148*(3), 45. https://doi.org/10.1088/0004-6256/148/3/45

Prior, D. J., Lilly, K., Seidemann, M., Vaughan, M., Becroft, L., Easingwood, R., … Wilson, C. J. L. (2015). Making EBSD on water ice routine: ICE EBSD. *Journal of Microscopy*, *259*(3), 237–256. https://doi.org/10.1111/jmi.12258

Raj, R. (1975). Transient behavior of diffusion-induced creep and creep rupture. *Metallurgical and Materials Transactions A*, *6*(8), 1499–1509.

Raj, R., & Ashby, M. F. (1971). On Grain Boundary Sliding and Diffusional Creep. *Metallurgical Transactions*, *2*, 1113–1127.

Rutter, E. H., & Brodie, K. H. (1988). The role of tectonic grain size reduction in the rheological stratification of the lithosphere. *International Journal of Earth Sciences*, *77*(1), 295–307.

Schoof, C. (2010). Ice-sheet acceleration driven by melt supply variability. *Nature*, *468*(7325), 803–806. https://doi.org/10.1038/nature09618

Sejrup, H. P., Clark, C. D., & Hjelstuen, B. O. (2016). Rapid ice sheet retreat triggered by ice stream debuttressing: Evidence from the North Sea. *Geology*, *44*(5), 355–358. https://doi.org/10.1130/G37652.1

Shimizu, I. (1998). Stress and temperature dependence of recrystallized grain size: A subgrain misorientation model. *Geophysical Research Letters*, *25*(22), 4237–4240.

Smith, S. A. F., Di Toro, G., Kim, S., Ree, J.-H., Nielsen, S., Billi, A., & Spiess, R. (2013). Coseismic recrystallization during shallow earthquake slip. *Geology*, *41*(1), 63–66. https://doi.org/10.1130/G33588.1

Spahn, F., Schmidt, J., Albers, N., Horning, M., Makuch, M., Seib, M., … Grun, E. (2006). Cassini Dust Measurements at Enceladus and Implications for the. *Science*, *311*(5766), 1416–1418.

Stern, L. A., Durham, W. B., & Kirby, S. H. (1997). Grain-size-induced weakening of H2O ices I and II and associated anisotropic recrystallization. *Journal of Geophysical Research*, *102*(B3), 5313–5325.

Suckale, J., Platt, J. D., Perol, T., & Rice, J. R. (2014). Deformation-induced melting in the margins of the West Antarctic ice streams. *Journal of Geophysical Research: Earth Surface*, *119*(5), 1004–1025. https://doi.org/10.1002/2013JF003008

Sutton, A. P., & Balluffi, R. W. (1995). *Interfaces in Crystalline Materials*. Oxford University Press.

Tobie, G., Choblet, G., & Sotin, C. (2003). Tidally heated convection: Constraints on Europa's ice shell thickness. *Journal of Geophysical Research*, *108*(E11). https://doi.org/10.1029/2003JE002099

Tufts, B. R., Greenberg, R., Hoppa, G., & Geissler, P. (1999). Astypalaea Linea: A large-scale strike-slip fault on Europa. *Icarus*, *141*, 53–64.

Twiss, R. (1977). Theory and Applicability of a Recrystallized Grain Size Paleopiezometer, 227–244.

Verberne, B. A., Plümper, O., de Winter, D. M., & Spiers, C. J. (2014). Superplastic nanofibrous slip zones control seismogenic fault friction. *Science*, *346*(6215), 1342–1344.

Warren, J. M., & Hirth, G. (2006). Grain size sensitive deformation mechanisms in naturally deformed peridotites. *Earth and Planetary Science Letters*, *248*(1–2), 438–450. https://doi.org/10.1016/j.epsl.2006.06.006

Whillans, I. M., & van der Veen, C. J. (1997). The role of lateral drag in the dynamics of Ice Stream B, Antarctica. *Journal of Glaciology*, *43*(144), 231–237.

Willis, J. K., & Church, J. A. (2012). Regional sea-level projection. *Science*, *336*(6081), 550–551.

Chapter 4 | Low-frequency Attenuation in Creeping, Polycrystalline Ice

Tess E. Caswell[1] and Reid F. Cooper[1]

[1]Department of Earth, Environmental and Planetary Sciences, Brown University, Providence, RI, USA

Abstract

We have measured Young's modulus attenuation (Q_E^{-1}) in creeping, polycrystalline water ice (grain size, d, 15 μm – 1 mm) through creep/attenuation experiments in which stress, $\sigma = \sigma_m \pm \sigma_o \exp(i\omega t)$, where σ_m = 0.4 – 2 MPa, σ_o = 0.05-0.1 MPa, and $\omega = 2\pi f$, where $10^{-4} \leq f$ (Hz) ≤ 0.1 at a temperature of 240 K. The attenuation response is linear in stress, indicating a diffusional mechanism, although the specimens were simultaneously deforming at steady-state via the nonlinear mechanisms of grain boundary sliding and/or dislocation creep. We find that ice exhibits a power-law background absorption overlain by a grain boundary viscosity effect, the character of which is influenced by creep regime. In the GBS regime the effect is broadly distributed, corresponding to a distribution of microstructural length scales spanning at least two orders of magnitude in length, while in the dislocation creep regime the effect is well-matched by an absorption peak at a length scale corresponding to the stress-sensitive distribution of subgrain sizes.

1. Introduction

Attenuation in water ice is critical to understanding the geophysics of icy satellites in the outer solar system. These icy bodies are (or have been) geologically active: for example, Jupiter's moon Europa is riddled with arcuate fractures, bands reminiscent of terrestrial spreading ridges, and disrupted regions known as chaos terrain (Greeley et al., 1998; Pappalardo et al., 1998; Pappalardo & Barr, 2004), while at Saturn, geysers from the South Polar Terrain of diminutive Enceladus erupt in concert with gravitational tides imposed on the icy lithosphere (Nimmo et al., 2014; Porco et al., 2006; Waite Jr et al., 2009). In addition to the array of geologic activity observed on the surfaces of these bodies, some icy moons, such as Europa, Callisto, and Enceladus, are suspected to possess subsurface oceans (Khurana et al., 1998; Thomas et al., 2016; Waite Jr et al., 2009; Zimmer et al., 2000).

For many icy bodies, maintaining oceans and geologic activity to the present day requires a source of energy input to the ice shell in addition to radiogenic and/or accretional heat (Cassen et al., 1979; Pappalardo et al., 1998). Thick layers of low-viscosity water ice overlying global or regional seas are expected to undergo convection (Barr & Pappalardo, 2005; Consolmagno & Lewis, 1978; McKinnon, 2006; Reynolds & Cassen, 1979), which would be expected to freeze an H_2O layer such as Europa's within a few tens of millions of years (Reynolds & Cassen, 1979). One source of energy is tidal dissipation, which generates heat within the ice shell through viscoelastic relaxation of time-varying tidal potential (e.g., Ojakangas and Stevenson, 1989). The physical process transforming tidal strain energy into heat is known as attenuation (Q^{-1}: the inverse of the "quality factor," Q, used in many seismic and geophysical models). For a material undergoing cyclic loading, attenuation is defined as the ratio of energy dissipated to that stored elastically per radian (Nowick & Berry, 1972). The dominant physical process responsible for attenuation varies depending on the material, temperature, and frequency explored (Cooper, 2002; Nowick & Berry, 1972).

1.1. Attenuation: Phenomenology and Theory

Planetary geodynamicists have historically modeled attenuation in an ice shell using the Maxwell solid model (Hammond & Barr, 2014; Ojakangas & Stevenson, 1989; Tobie et al., 2003), with some exceptions (e.g. Castillo-Rogez et al., 2011). The Maxwell model employs a spring and dashpot in mechanical series (kinetic parallel) to simulate the elastic and steady-state viscous properties of a material (Findley et al., 1976). The Maxwell model predicts an attenuation spectrum (Q^{-1} vs $f^{-\varphi}$) with $\varphi = -1$, which shifts in frequency space according to the Maxwell relaxation time: $\tau_M = \eta/Y$, where η is the steady-state viscosity of the material and Y is Young's modulus.

The Maxwell model does not, however, capture the real attenuation behavior of materials (Cooper, 2002). In Figure 1a, which compares the model to experimental data for olivine and borneol (a crystalline organic), one sees that the Maxwell model underestimates attenuation at high frequencies and overestimates attenuation at low frequencies (Cooper, 2002; figure modified from McCarthy et al., 2011). The spectra in Fig. 1 illustrate the form of what is known as the high-temperature background, over which $0 < \varphi \leq 0.5$ (Cooper, 2002; McMillan et al., 2003). Similar values of φ been inferred seismologically (Anderson & Minster, 1979; Molodensky & Zharkov, 1982) and in the lab (Berckhemer et al., 1982; Gribb & Cooper, 1998; Jackson et al., 2002; McCarthy et al., 2011). In Fig. 1a, the Maxwell model and the datasets have been normalized by dividing the measurement frequency by the Maxwell frequency ($f_M = 1/\tau_M$) of the rheological mechanism giving rise to attenuation (McCarthy et al., 2011; McCarthy & Cooper, 2016). The *magnitude* of attenuation has not been normalized. Normalization of this type has been referred to as "master variable" scaling (Abers et al., 2014; Jackson et al., 2014; McCarthy et al., 2011). Proper extrapolation of laboratory data requires interpretation (selection) of the underlying physics of τ_M.

The Maxwell model fails to represent the response of real materials because it lacks anelasticity, that is, time-dependent, recoverable strain (Findley et al., 1976, p. 57).

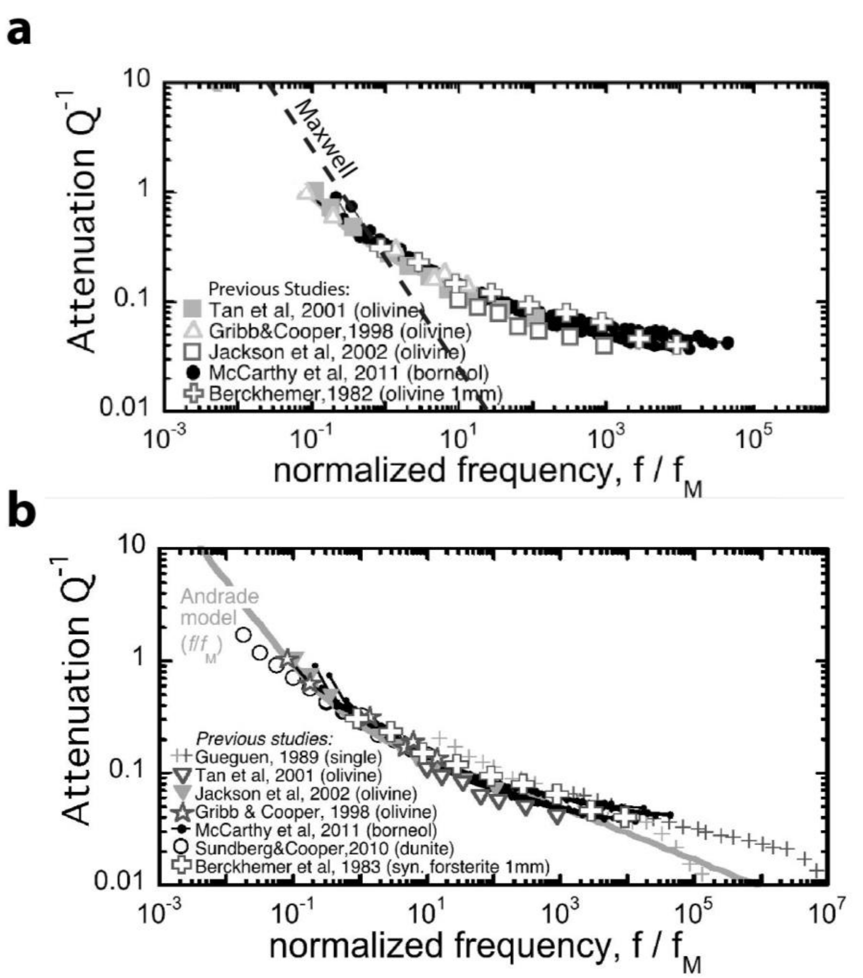

Figure 1: Data and models of attenuation, normalized in frequency space by the Maxwell frequency of the rheological mechanism causing attenuation. a) The Maxwell model, used historically by planetary geophysicists to represent tidal dissipation, relative to real attenuation data that have been normalized based on a Maxwell time corresponding to diffusion creep at the scale of the grain size (after McCarthy et al., 2011). While the data approach the form of the Maxwell model at the lowest (normalized) frequencies, overall the model does not capture real attenuation behavior well. b) The Andrade model, linked to the diffusional evolution of tractions on grain boundaries, against a similar data set (after McCarthy & Cooper, 2016). Specifically included are data for polygonized single-crystal olivine (Gueguen et al., 1989), where the Maxwell frequency for normalization is that of diffusion creep of subgrains (McCarthy & Cooper, 2016). Data deviate from the Andrade model at high frequencies, where the assumption of shear-inviscid grain boundaries breaks down.

Anelasticity is, however, integral to attenuation (Karato, 1993; Nowick & Berry, 1972). An oft-employed solution to this problem is the application of a Burgers solid (e.g., Faul & Jackson, 2005), which adds an anelastic element (with a discrete relaxation time) in mechanical series with the Maxwell solid, thereby producing a discrete peak in the attenuation spectrum (Findley et al., 1976). The "extended Burgers model" sums a number of these elements (the exact number determined by fitting) to capture the high-temperature background spectrum in measured data (Jackson & Faul, 2010). The difficulty with extrapolating the extended Burgers model to geophysical conditions is that each of these semi-arbitrary number of Burgers solids, each with its own discrete relaxation time, must be ascribed a physical basis (Cooper, 2002).

Gribb and Cooper (1998) suggested an alternative method for modeling the high-temperature background based on the Andrade model of viscoelasticity (Andrade, 1910), which represents anelasticity with a power law. Gribb & Cooper (1998) successfully reproduced their measured high-temperature background spectra by first parameterizing the Andrade model from their measured diffusion creep data, then inverting the model to predict attenuation. The predictions matched their measured attenuation data well (Gribb & Cooper, 1998). Good agreement between the Andrade model and their creep data indicated that the physics captured by the model were those of diffusion creep, while the good fit of the Andrade model inversion to their attenuation spectra indicated that the high-temperature background has the same physical basis. Thus the physics of the high-temperature background are those of chemical diffusional in the context of diminishing potential (Gribb & Cooper, 1998; Raj & Ashby, 1971; Raj, 1975). The Andrade model thus provides a representation of the high-temperature background with a sound physical basis that requires only a single, characteristic length scale of diffusion.

Proper computation of τ_M thus requires knowledge of the length scale of diffusion (Gribb & Cooper, 1998; Jackson et al., 2014; McCarthy et al., 2011). Lack of consensus regarding the appropriate choice for this length scale has complicated efforts to determine a "master variable" (Jackson et al., 2014; McCarthy et al., 2011). Based on the kinetics of diffusion creep (Coble, 1963; Herring, 1950; Nabarro, 1948), the length scale is often assumed to be grain size (e.g., Abers et al., 2014; Behn et al., 2009; Jackson et al., 2014). This approach has been successful for a suite of laboratory data on fine-grained materials deforming via diffusion creep (e.g., McCarthy et al., 2011). However, Gribb & Cooper (1998) noted that extrapolations to mantle conditions did not match seismological observations if based primarily on grain size, and instead suggested that in a deforming medium such as the Earth's mantle, diffusion along low-angle (subgrain) boundaries may dominate. As a result, the stress-sensitive subgrain size would serve as the characteristic length scale of diffusion (Gribb & Cooper, 1998; cf. Stone, 1991). Indeed, attenuation data for deformed (polygonized) single-crystal olivine have been normalized in Fig. 1b according to diffusion creep of subgrains (Gueguen et al., 1989; Gueguen & Darot, 1982); one sees that these data collapse onto the "master curve" when so normalized. McCarthy & Cooper (2016) also normalized their (grain size-insensitive) attenuation data for creeping, polycrystalline ice according to a Maxwell time based on diffusion creep at a length scale smaller than the grain size, which collapsed the data onto the form of the Andrade model although the ice was an order of magnitude more attenuating than predicted. Thus, while the diffusional nature of the high temperature background is well agreed-upon, the characteristic length scale of that diffusion remains a subject of active research (Jackson et al., 2014; McCarthy et al., 2011; McCarthy & Cooper, 2016; Morris & Jackson, 2009).

Proper selection of τ_M is further complicated by the potential presence, at specific frequencies, of peaks overlying the high-temperature background (Nowick & Berry, 1972). In pure water ice, notable peaks are associated with the movement of protons through lattice defects (Kuroiwa, 1964a), grain boundary processes (Cole, 1995; Kuroiwa, 1964b; Tatibouet et al., 1987; c.f. Ke, 1999), and the bowing of basal dislocations (Cole, 1995; c.f. Granato & Lücke, 1956).

Of particular relevance to this work are studies conducted on ice at low (<1 Hz) frequencies. Tatibouet et al. (1987) measured attenuation in this frequency range specifically to investigate the grain boundary peak in water ice. Through torsion experiments conducted on bicrystals, these authors clearly resolved a peak associated with the presence of grain boundaries. To investigate attenuation under the conditions expected within an icy satellite, McCarthy & Cooper (2016) conducted creep and attenuation experiments on water ice in the rheological regime of grain boundary sliding rate-limited by the grain boundary viscosity. These authors observed that the ice was more attenuating than predicted by the Andrade model, modestly nonlinear (indicating a contribution of dislocation glide to the response), and insensitive to grain size. The authors suggested that rather than the grain size, it was the stress-sensitive subgrain size that set the length scale of diffusion relevant to the attenuation response, but their data could not be used to explore this hypothesis because they did not vary mean stress in their experiments.

This work addresses the hypothesis of stress-dependent attenuation directly through creep/attenuation experiments conducted at a range of grain sizes (d = 10 μm-1 mm), at a stress state of $\sigma = \sigma_m \pm \sigma_o \exp(i\omega t)$, where mean stress σ_m = 0.4-2 MPa, and sinusoidal stress amplitudes, σ_o = 0.05-0.1 MPa. All experiments were conducted at 240K (a homologous temperature of T/T_{fus} = 0.88). The grain sizes, stress and temperature are chosen so that steady-state creep is by the mechanisms expected within a convecting planetary ice shell (Barr & Pappalardo, 2005; Barr & Showman, 2009): grain boundary sliding rate-limited by the grain boundary viscosity or dislocation creep, according to the rheology for polycrystalline water ice articulated by Goldsby & Kohlstedt (2001). We find that the attenuation response is linear in stress, indicating a fundamentally diffusional mechanism. The measured spectra are consistent with the high-temperature background overlain by a broad, peak-like feature, though the nature of this feature differs fundamentally from that of a peak associated with a discrete relaxation time.

2. Experimental Approach

2.1. Specimen Fabrication

In order to assess the effect of grain size on attenuation, three distinct methods of specimen preparation were utilized: "standard ice" (Cole, 1979), hot-pressing, and pressure-cycling (Goldsby & Kohlstedt, 2001; Stern et al., 1997). Standard ice was fabricated by grinding frozen, deionized water and sieving the resulting powder to separate the desired grain size, which was then packed into a cylindrical mold. Vacuum was drawn on the mold and the powder was then flooded with degassed, deionized water at 0°C/273K. The sample was then frozen slowly, from the bottom-up, overnight at -20°C/253K. The resulting material was fully dense and contained randomly-oriented grains. By this method we fabricated our coarse grain-sized specimen (hereafter referred to as the "Coarse" specimen): 2.5-cm diameter cylinders, 3-5 cm in length, with grain size $d \sim 1$ mm.

Hot-pressed ice was fabricated by nebulizing deionized water in air and directing the spray into liquid nitrogen (LN_2). The resulting slurry was sieved in liquid nitrogen to obtain the desired grain size. Sieving was performed in a chest freezer under N_2 gas so that atmospheric CO_2 and water vapor do not deposit onto the sieved material. The resulting powder was packed into a cylindrical vacuum mold and hot pressed in dry ice (195K) at 100 MPa for 2 h. The resulting sample was fully dense, with a grain size approximately equal to the particle size of the initial sieved powder (Caswell et al., 2015; Goldsby & Kohlstedt, 1997; Prior et al., 2015). By this method we produced our medium and fine grain-sized specimens (hereafter referred to as "Medium" and "Fine" specimens, respectively): 1-cm diameter, 2-cm length cylinders with mean grain sizes of 40 μm (Fine) and 70 μm (Medium).

Pressure-cycled ice was prepared in an identical manner to hot pressing, except for an additional sequence of high-pressure/low-pressure cycles prior to hot pressing (Stern et al., 1997). Each pressure cycle initiated a phase transformation from ice Ih to ice II by increasing the (nominally hydrostatic) stress on the sample to 250-300 MPa. The sample was held at this pressure for 5 min to allow the phase transformation to complete before the pressure was rapidly released, driving a phase transformation back to ice I. During the phase transformation, the kinetics of nucleation dominate relative to those of grain growth and a high density of ice I nuclei is produced. These nuclei then grow to produce specimens of extremely fine grain size (5-10 μm). The pressure-cycling process was repeated six times, followed by hot pressing, to produce our finest grain-sized (hereafter referred to as "Very Fine") specimens: 1-cm diameter, 2-cm length cylinders with initial mean grain size <10 μm.

Prior to each experiment, a sample of the starting material was sectioned from one end of the cylindrical specimen and placed directly into storage in liquid nitrogen (−196°C/77K) for later microstructural comparison. Deformed specimens were also transferred into liquid nitrogen storage immediately following completion of each mechanical experiment.

2.2. Experimental Apparatus and Procedures

Our creep/attenuation experiments were designed specifically to explore the relationship between Q^{-1}, mean stress (σ_m) and sinusoidal stress amplitude (σ_o) across a range of frequencies. The experiments utilized a computer-controlled, servomechanical apparatus (Instron Model 1361, Canton, MA) modified by the addition of an ambient-pressure, liquid nitrogen-cooled, ethanol-bath cryostat that maintained sample temperature within ±0.5°C (Fig. 2). Strain and strain rate in the sample were determined by measuring the displacement between ceramic platens abutting the sample using an extensometer-mounted direct current differential transformer (DCDT). Sample temperature was measured by a Type-T (copper–constantan) thermocouple embedded in the uppermost platen. During deformation, the specimen and extensometer were fully encased in a gas-tight chamber which was periodically purged with gaseous N_2 to preclude frost accumulation on the sample assembly and sensors. Data acquisition was via a National Instruments 24-bit analog-to-digital converter and employed averaging in

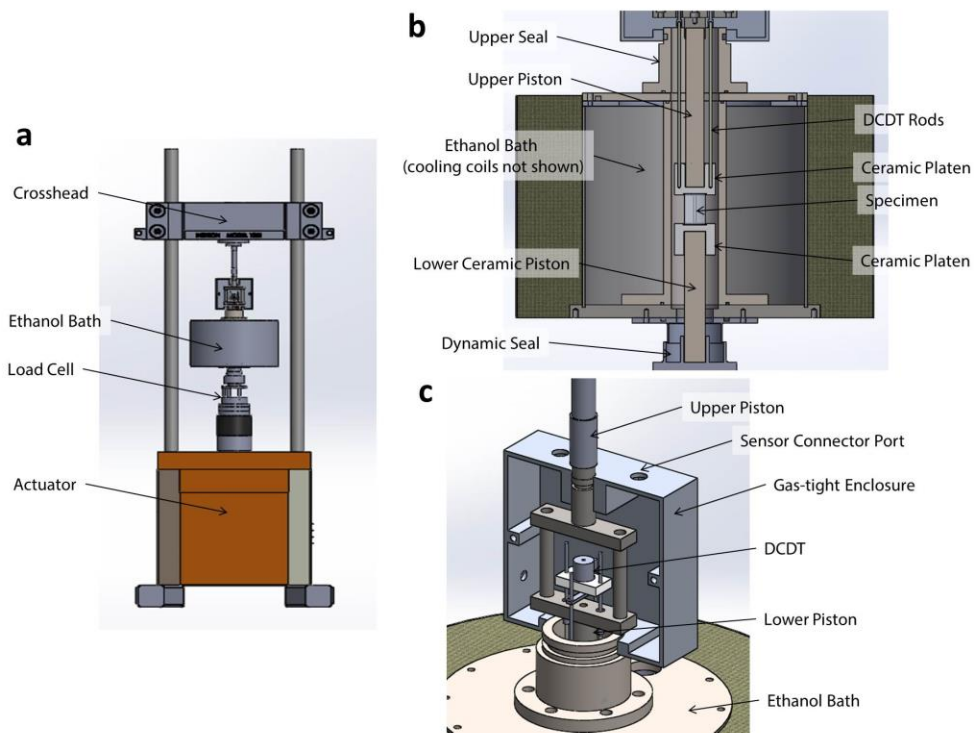

Figure 2: The apparatus employed in this research. a) The Instron 1361 servomechanical actuator and load frame, with liquid nitrogen-cooled cryostat mounted to the load frame. The cryostat is supported by cantilever beams (not shown) affixed to the apparatus' vertical columns. b) Detail of sample assembly within the cryostat. The sample and pistons pass through a gas-tight cylindrical volume isolated from the ethanol bath. The sample itself is abutted by two ceramic platens. Displacement between the platens is measured by an extensometer-mounted DCDT, shown in (c). Load bypasses the sensors via a "cage," which diverts the load to two parallel, steel columns adjacent to the sensor.

LabVIEW to mitigate electronic noise (e.g., during the creep phase data are recorded at 5 Hz, but each recorded datum is an average of one thousand measurements collected at 5 kHz). Measured strain resolution was 10^{-7}. Load was measured by a 2.2 kN-capacity load cell with resolution of 0.035 N. The computer-controlled load setpoint was adjusted every ~24 h to maintain constant stress on the sample, assuming constant-volume deformation of a cylindrical sample.

In the creep phase(s) of each experiment, a constant compressive stress (σ_m) was applied to the sample. The temperature (240K), grain sizes (~10-300 μm), and mean stresses (0.4-2.0 MPa) of the experiments were designed to elicit deformation in the regime of grain boundary sliding that is rate-limited by sliding on the boundary (Goldsby & Kohlstedt, 2001). The exception to this rule is the Coarse specimen, for which steady-state strain rates in the GBS regime would have been prohibitively low; the conditions of this experiment were therefore designed to induce steady-state deformation by dislocation creep. To minimize the effect of inter-sample variability on our results, attenuation measurements were taken using the same specimen at multiple mean stresses. After minimum strain rate (steady-state) was achieved (verified by monitoring strain rate vs strain), a time-varying, sinusoidal compressive stress (σ_0) was overlain on the median stress. σ_o was varied discretely between 0.05-0.1 MPa (corresponding to $\varepsilon \approx 0.5\times10^{-6}$ – 1×10^{-5} at the temperature-corrected modulus of 9.6 GPa after Gammon et al., 1983), with 5-10 cycles per each value of σ_o.

Complex modulus and attenuation were measured from the amplitude ratio and phase lag, respectively, between the peak stress and peak strain (Nowick & Berry, 1972).

Because the apparatus employs uniaxial compressive loading, these measured properties are Young's modulus (*Y*) and attenuation (Q_E^{-1}).

Attenuation was calculated from the phase lag, δ, between the peak stress and peak strain according to (Nowick & Berry, 1972):

$$Q^{-1} = \tan(\delta) \qquad [1]$$

The phase lag was determined by fitting both the stress and strain signals with a sinusoidal waveform using a nonlinear least-squares regression in MATLAB, which also provided 95% confidence bounds. When the steady-state strain rate in the specimen was sufficiently high to superimpose a linear background trend on any waveform set, that trend was subtracted from the strain signal prior to waveform fitting.

2.3. Microstructure Analysis

Microstructure analyses were performed via reflected-light microscopy for all deformed samples and starting material, utilizing a Leica DM2700 optical microscope in a cold room (-17°C/256K) at Lamont-Doherty Earth Observatory (LDEO, Palisades, NY). Samples were transported to LDEO in a liquid-nitrogen-cooled dry shipping container. Once in the cold room, specimens for analysis were cut from the bulk specimen using a band saw, bonded to a glass slide by water droplets and shaved flat using a microtome. Brief sublimation etching (1-2 minutes) revealed grain (and subgrain) boundaries before images were acquired (Caswell et al., 2015).

Image analysis was conducted using the NIH software ImageJ. Grain size was measured by the line-intercept method using a geometrical multiplicative factor of 1.5 (Exner, 1972). Reported values are averages over multiple images from each sample.

3. Experimental Results: Description and Comment

In Fig. 3 we present measured Q^{-1} vs frequency for all grain sizes studied. Two characteristics shared by all of the measured attenuation spectra are illustrated by this figure. First, in the frequency range studied, all spectra display a power-law background ($Q^{-1} \propto f^{-\varphi}$), with φ = ~ 0.4. This power-law slope is consistent with theoretical values of $-0.5 \leq \varphi \leq 0$ for the high-temperature background (Cooper, 2002) and is in family with values reported by previous authors (e.g., Gribb & Cooper, 1998; McMillan et al., 2003); of specific interest is the similarity to the value of φ = 0.38 reported by McCarthy & Cooper (2016) for polycrystalline ice deforming via GSS creep at 240 K. Changing mean stress does not affect the power-law background absorption. Where the power-law background is clear (data for the Fine and Medium specimens), spectra for varied mean stresses overlie one another.

The second general feature shared by all spectra is enhancement of Q^{-1} from the power-law slope at frequencies > ~10^{-3} Hz. The character of this enhancement in Q^{-1} changes as grain size increases. In data for the Very Fine specimens, a partial peak is suggested by an increase in Q^{-1} at the highest frequencies studied. The feature is only partially resolved because it is apparently centered near, or beyond, 0.1 Hz. A small-amplitude peak is suggested in the data for the Fine specimens; these spectra also shallow rapidly with increasing frequency. Although a peak is not fully resolved in data for the Very Fine specimen, the inferred central frequencies in the spectra for the Very Fine and Fine specimens appear to be similar, at or near 10^{-1} Hz. In data for the Coarse specimen, this enhancement manifests as a peak-like feature (centered near 10^{-2} Hz) that dominates the observed spectrum, although there are important differences between the observed

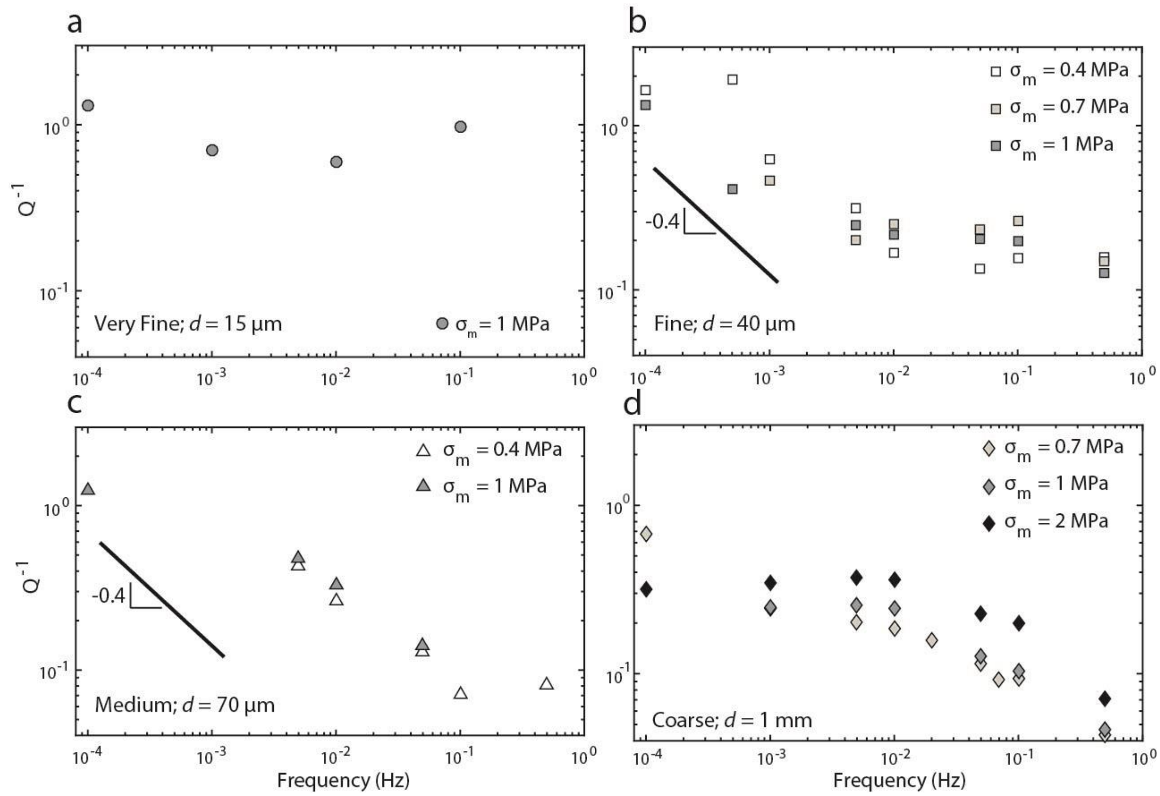

Figure 3: Attenuation spectra for all grain sizes at σ_o = 0.1 MPa. Solid lines are predicted Q^{-1} based on the composite model of Sundberg & Cooper (2010); predictions are inversions of the Andrade model based on fits to creep data for the same specimens at 1 MPa; fitting parameters are given in Table 1.Specimen grain size is indicated in the lower left of each panel: a) Very Fine specimen, for which creep data were too sparse to fit the Andrade model and therefore no Q^{-1} prediction is shown. b) Fine ; c) Medium; c) Coarse. Data sets for all but the Coarse specimen display a power-law background of slope ~ −0.4. A broad peak is apparent in the data for the Coarse specimen; this peak broadens toward higher frequency with increasing mean stress and is broader than one decade in frequency, indicating a distribution of length scales associated with the peak-producing relaxation process.

feature and attenuation peaks commonly described in the literature (c.f. Nowick & Berry, 1972, p.52). Principally, this feature is much wider than a single decade in frequency, indicating a distribution of associated relaxation times rather than the single, discrete relaxation time such as would be associated with a Debye peak (Nowick & Berry, 1972, p. 53). The enhancement of Q^{-1} is not affected by mean stress in data for the Very Fine, Fine, and Medium specimens, but is strongly affected in data for the Coarse specimen (Fig. 2d). There is a clear change in the frequency distribution of the broad peak as σ_m increases from 1 to 2 MPa, as well as a slight increase in height. The peak appears to broaden, rather than shift, as deviatoric stress is increased.

Figure 4 presents the effect of strain amplitude on attenuation in our specimens. Regardless of grain size or deviatoric stress, the magnitude of Q^{-1} is not affected by strain amplitude. This linearity indicates a diffusional mechanism is fundamental to the attenuation response, consistent with previous studies of the high-temperature background (Gribb & Cooper, 1998; Jackson et al., 2014; McMillan et al., 2003).

Figure 5 presents measured modulus dispersion for our specimens. The modulus dispersion is sigmoidal, similar to that which would be expected if dissipation by a mechanism acts in addition to the high-temperature background. This behavior is consistent with the enhanced dissipation observed in our Q^{-1} data at higher frequency. For comparison, the form of the modulus dispersion due to a superposition of the high-temperature background and a peak is illustrated as a dashed line in Fig. 5, while the form of modulus dispersion based on the high-temperature background alone is shown as a dotted line (Sundberg & Cooper, 2010).

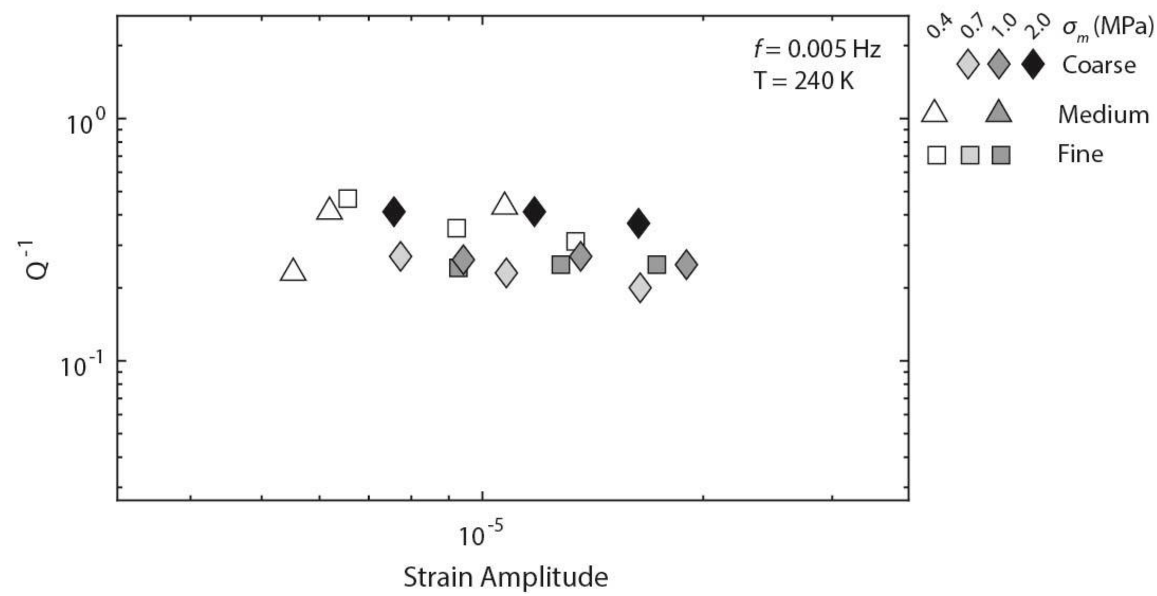

Figure 4: Strain amplitude dependence of attenuation at all grain sizes and creep stresses for which sufficient data are available (no sinusoidal stress variation data were collected for the Very Fine material). Variations in strain amplitude correspond to variations in sinusoidal stress amplitude. The data are linear under all conditions studied, indicating that dissipation is accomplished via a diffusional process, despite the fact that the steady-state rheology is nonlinear.

The microstructures of our samples are illustrated in Fig. 6. The Very Fine specimen (Fig. 6a) exhibits indications of grain growth; in addition to curved grain boundaries in the deformed specimen, the grain size of the specimen (~15 μm) is increased from that of the starting material for this experiment, which was ~8 μm. The microstructures of the Fine and Medium specimens are similar to one another: both evince grain flattening perpendicular to the compression direction (illustrated by Fig. 6b), straight grain boundaries, and numerous four-grain junctions (Fig. 6c), which are microstructural features considered diagnostic of GBS (Langdon, 1991). Finally, the Coarse specimen exhibits crenulated grain boundaries pinned by subgrain boundaries, which are prevalent throughout the specimen (Fig. 6d). The spacing between subgrain boundaries, averaged across multiple images of the specimen, is 53±22 μm. For comparison, a commonly employed model for subgrain size is that of Raj & Pharr (1986):

$$\frac{d_s}{b} = B\left(\frac{G}{\sigma}\right)^{\kappa}, \qquad [2]$$

where b is the magnitude of the Burgers vector of dislocations forming the subgrain boundary, G is the shear modulus of the material, and B and κ are empirical constants. For $B = 23$ and $\kappa = 1$, the mean subgrain size predicted in our Coarse specimen is 38 μm at 1 MPa and 19 μm at 2 MPa. The broad standard deviation of the measured subgrain spacing may be due to the low total accumulated strain in this specimen, which was only 1%, since it is generally accepted that 1-2% is needed to attain a steady-state microstructure (creep experiments by Hamann et al. (2007) showed that 1-2% strain was necessary to reach maximum subgrain boundary density in ice, while concurrent neutron

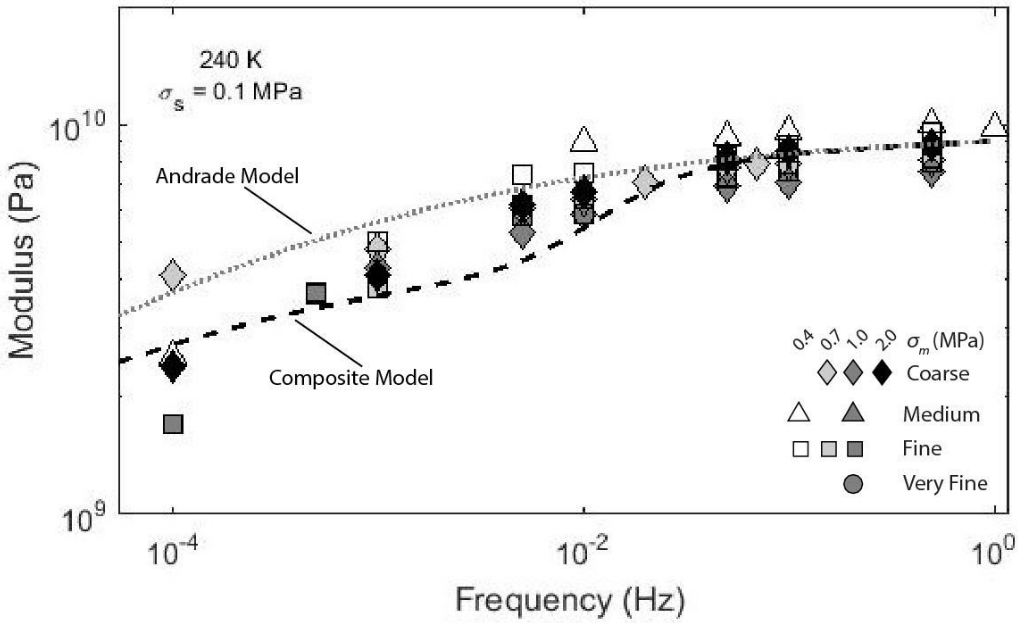

Figure 5: Measured modulus dispersion for all grain sizes and mean stresses. The form of the data is sigmoidal, indicating the contribution of a specific relaxation mechanism in the frequency range studied in addition to the high-temperature background. For comparison, the shapes of two different modulus dispersions are shown: that based solely on the Andrade model (dotted line) and that of the Andrade model with the contribution of a second mechanism with a discrete relaxation time near 100 s (Sundberg & Cooper, 2010).

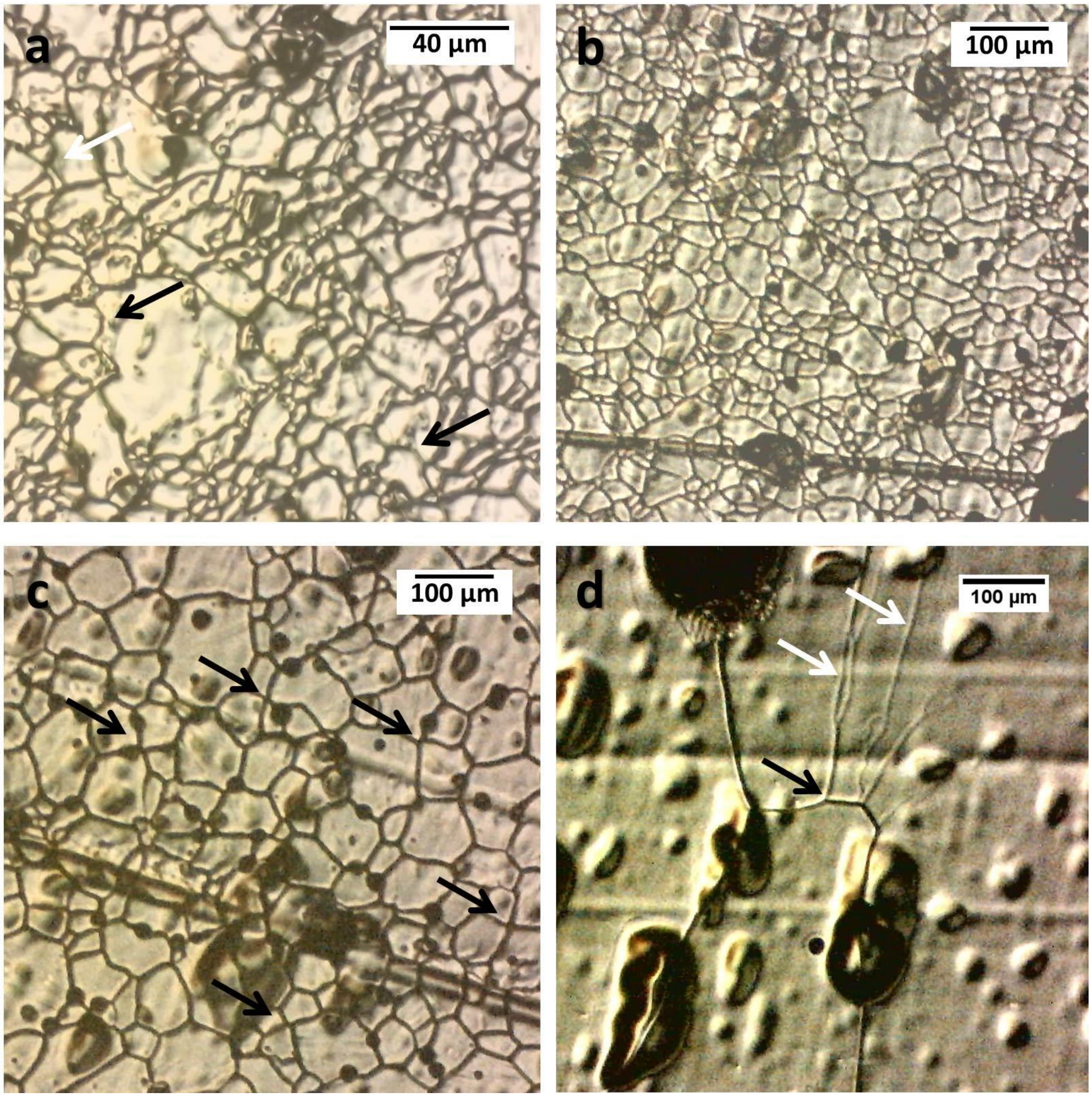

Figure 6: Microstructures of specimens deformed in this study. a) A Very Fine specimen, which shows indications of grain growth including convex-out grain boundaries on small grains (black arrows). The specimen also exhibits four-grain junctions (white arrow). b) A Fine specimen, which exhibits grain flattening observed in both the Fine and Medium specimens. The compression direction is vertical. c) A Medium specimen, exhibiting numerous four-grain junctions (black arrows) and straight grain boundaries. d) A pinned grain boundary (black arrow) in the Coarse specimen, from which numerous subgrain boundaries (white arrows) emanate. The spacing between subgrain boundaries is ~45 µm.

diffraction and deformation of D_2O ice by Piazolo et al. (2013) showed that steady-state grain size in constant strain-rate experiments required ~10% strain). The observed broad distribution of subgrain boundary spacing in the Coarse specimen indicates that the subgrain structure at 2 MPa was not fully equilibrated with the applied stress and that the final subgrain structure is an overprinting of boundaries formed at both 1 MPa and 2 MPa.

4. Discussion

The data demonstrate that the deformation process giving rise to attenuation need not be the same as that by which the material deforms at steady-state. The steady-state flow of our specimens is nonlinear in stress – in ice, both GBS and dislocation creep are power-law mechanisms involving the nucleation and movement of dislocations. Despite this, attenuation in our creeping specimens is linear, indicating a diffusional mechanism.

The linearity of attenuation in a nonlinear creep regime can be reconciled by considering the model of grain boundary "hardness" proposed by Caswell et al. (2015). The model, based on stress-reduction experiments that explored the constant-hardness compliance of ice creeping in the regime of GBS rate-limited by the boundary viscosity, asserts that grain boundaries in ice undergoing GBS develop faceting that promotes the easy motion of grain boundary dislocations between facet intersections and thereby lowers the grain boundary viscosity. The compliance distribution measured by these authors exhibited two regimes: at low stresses, the compliance distribution is linear, while at high stresses the compliance distribution is nonlinear and obeys a theoretical distribution based on defect motion at self-similar length scales (Hart, 1970; Stone, 1991;

Stone et al., 2004). The linearity of our data indicates that small stress perturbations, such as the sinusoidal load applied during our experiments, sample the linear regime of this compliance distribution. Thus, despite a nonlinear steady-state viscosity, attenuation in ice creeping via GBS is linear and due to diffusional processes at length scales smaller than the grain size.

4.1. Scaling of the High-Temperature Background

A diffusional foundation grants the license for exploring the Andrade model fit to our data. To do so, we fit the transient creep data for our specimens to the Andrade function for time-dependent strain:

$$\varepsilon(t) = \sigma\left(\frac{1}{Y_U} + \beta t^{\psi} + \frac{t}{\eta_{SS}}\right), \qquad [3]$$

where Y_U is the unrelaxed Young's modulus, β and ψ are parameters associated with the strength and rate of the grain boundary diffusion process described in Section 1, and η_{ss} is the steady-state viscosity. An example of the quality of fits to our creep data is shown in Fig. 7, and best-fit Andrade model parameters are given in Table 1. Fitting parameters are only available for experiments with sufficiently clean transient creep data, free from thermal or other effects. To calculate attenuation, Eq. (3) is converted to compliance [$J(t) = \varepsilon(t)/\sigma(t)$], then Laplace transformed to a function of frequency (cf., Findley et al., 1976): $J(\omega)=J_1(\omega)+iJ_2(\omega)$. Attenuation is then calculated from the ratio of the imaginary and real components of the compliance:

$$Q^{-1} = \frac{1}{2\pi}\frac{J_2}{J_1}. \qquad [4]$$

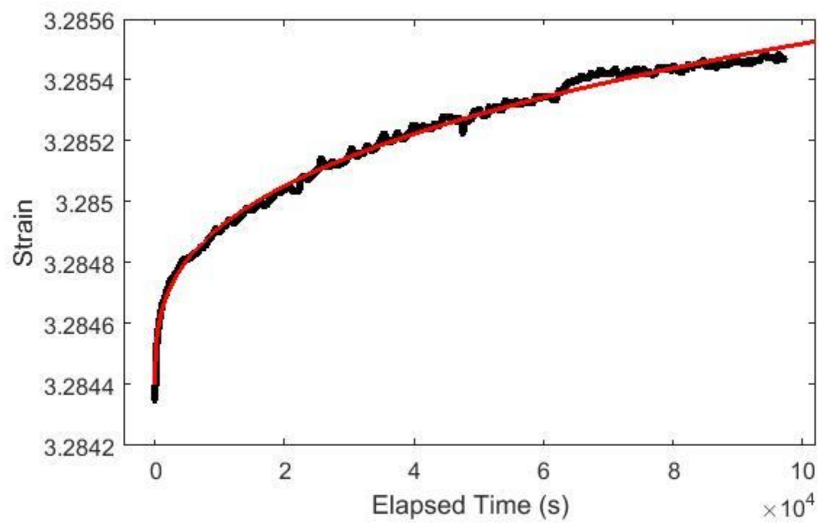

Figure 7: Demonstration of the quality of fit of the Andrade model (red line) to transient creep of the Coarse specimen (black data) following application of σ = 0.7 MPa. Fitting parameters are given in Table 1.

Andrade model predictions produced in this manner are shown for comparison to our data as dashed lines in Fig. 8. The predictions are in the ballpark of our attenuation data, matching the lowest frequency studied for each data set, but deviate markedly from our data with increasing frequency. Unsurprisingly, the Andrade model alone does not capture the enhancement of attenuation at higher frequencies, due to the feature enhancing Q^{-1} as described in Section 3. Incorporating this feature into any model of attenuation requires an exploration of potential length scales underlying the physics.

4.2. Q^{-1} Enhancement in the Dislocation Creep Regime

In much of the geophysical literature (e.g., Dalton et al., 2009; Jackson et al., 2014; Karato, 1989), peaks in the frequency range of the feature observed in data for our Coarse specimen are attributed to the process of elastically accommodated grain boundary sliding (hereafter, eGBS). During this anelastic process, the elastic energy accumulated along grain boundary topography is partially dissipated by the viscosity of the grain boundary when load is reversed. The relaxation time for eGBS is

$$\tau_{GBS} = \frac{\eta_{GB} l}{\delta G_U}, \qquad [5]$$

where η_{GB} is the grain boundary viscosity and G_U is the unrelaxed shear modulus (Kê, 1947; Nowick & Berry, 1972). The length scale, l, is defined by the slip distance during boundary sliding. Although the classical formulation of grain boundary relaxation assumes a planar, flat boundary and thus takes l to be the grain size (Ke, 1999), we relax this assumption and choose not to define l as the grain size *a priori*. Nowick & Berry (1972, p. 437) specifically point out that obstacles to GBS may result in τ depending on a length scale smaller than grain size. The calculations of Raj & Ashby (1971), upon which

Eq. (5) is based, indicate that the shape and wavelength of grain boundary topography may be first-order in relaxation processes on the grain boundary, a point reiterated by Kê (1999). For the approximate central frequency of the feature in the spectra for our Coarse specimen, which is 0.01 Hz, Eq. (5) yields a relaxation length scale of 61 μm [η_{GB} = 5.3×10^6 Pa·s and G_U = 3.6 GPa after Caswell et al. (2015) and Gammon et al. (1986), respectively]. This length scale is very similar to the spacing of subgrain boundaries observed in our Coarse specimen, 53 μm (Fig. 6d). In addition to the similarity in relaxation length scale, the observed shift of the Q^{-1} spectra to higher frequencies (corresponding to smaller length scales of relaxation) with increasing stress is consistent with the inverse stress sensitivity of subgrain size (Shimizu, 1998; Twiss, 1977). The effect of subgrain boundaries on eGBS in ice is therefore to crenellate the grain boundaries with cusps (through pinning, as seen in Fig. 6d), the length scale of which affects the length scale of sliding. Thus, the distribution of length scales at which elastically accommodated GBS occurs must be extended to include the stress-effected subgrain size.

The attenuation model of Sundberg & Cooper (2010) specifically addressed the superposition of an Andrade model-based high-temperature background with elastically-accommodated GBS. The Sundberg & Cooper (2010) model expresses the composite compliance as

$$J(t) = J_U + J_U\Delta\left(1-\exp\left(\frac{-t}{\tau_{GBS}}\right)\right) + \beta t^{\psi} + \frac{t}{\eta_{SS}}, \qquad [6]$$

where Δ is the relaxation strength [$\Delta = (G_U\text{-}G_R)/G_R$]. The attenuation spectrum predicted by Eq. (6) for our Coarse specimen, based on the Andrade model fits in Table 1 and τ_{GBS}

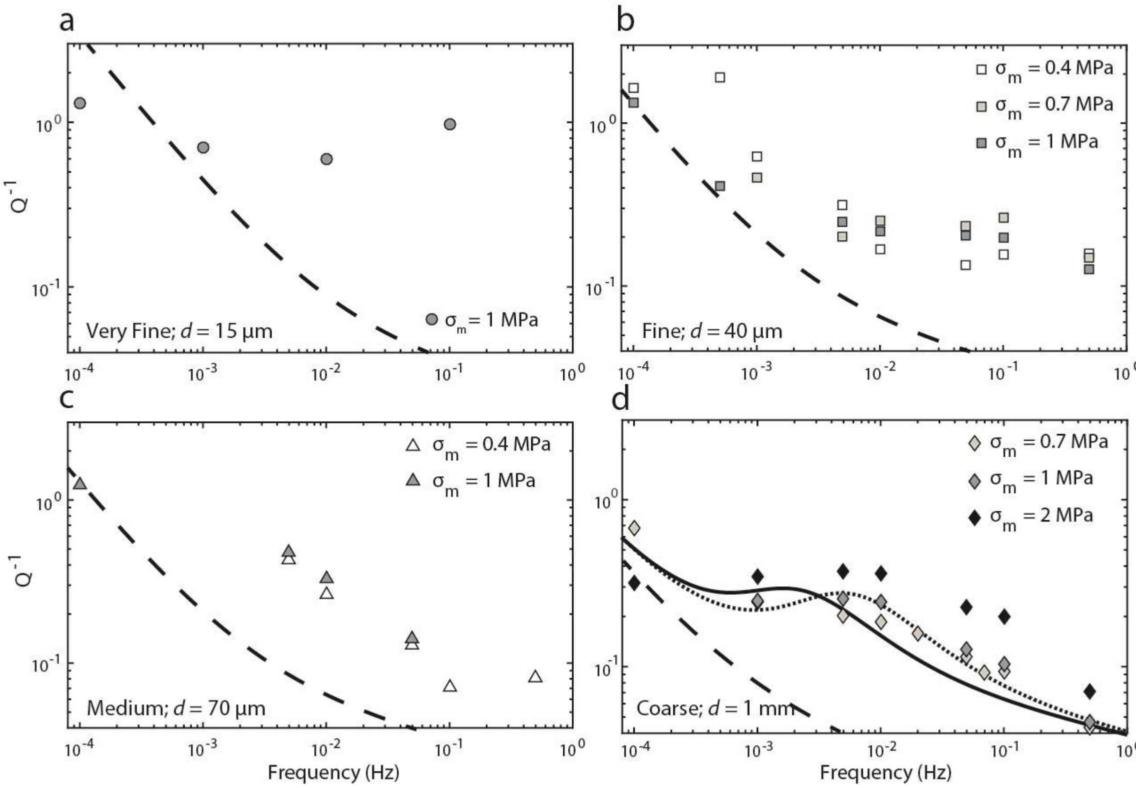

Figure 8: Comparison of the measured attenuation spectra to models described in the text. Data presented are identical to those in Fig. 3, comprised of attenuation spectra for all grain sizes at σ_0 = 0.1 MPa. Each panel contains an Andrade model prediction of Q^{-1} (dashed lines), while the Coarse grain-sized data (panel d) includes the composite model of Sundberg & Cooper (2010). The position of the peak due to eGBS is modeled using the mean spacing of subgrains observed in the deformed specimen (53 µm; Solid line) and that predicted by Raj & Pharr (1986) at 2 MPa (19 µm; Dotted line). The fit of the composite model to the data is good, although it does not capture the full frequency breadth of the eGBS feature.

for the observed subgrain size of 53 μm, is plotted as a solid line in Fig. 8d. Considering the broad distribution of subgrain sizes seen in the Coarse specimen, the absorption peak position predicted by the subgrain size of Raj & Pharr (1986) at 2 MPa (19μm) is also plotted. The relaxation strength, Δ, was determined by fitting Eq. (6) to our modulus dispersion; an adequate fit requires that the relaxed modulus must be 55% of the unrelaxed modulus and, thus, the relaxation strength (Δ in Eq. 6) is ~0.82. A material such as ice (with Poisson's ratio = 1/3) would be expected to have a relaxation strength of 0.64 or less, depending on the model used (Ghahremani, 1980; Ke, 1947; Sundberg & Cooper, 2010).

The match between our data and the Sundberg and Cooper (2010) model prediction is acceptable. However, the model does not capture the full breadth of frequency of the peak-like feature seen in our data. This breadth indicates that a distribution around the mean subgrain size acts to enhance attenuation in the frequency range studied, which is consistent with microstructural observations by, for example, Stone et al. (2004), who observed a normal (and self-similar) distribution of stress sensitive microstructural features at all length scales studied. Thus, future models should employ a normal distribution of grain boundary relaxation length scales centered about the mean subgrain size.

The maximum stresses applied to the Coarse specimen is less than one third the compressive fracture strength of granular ice (Schulson, 2001). No modulus reduction, which would indicate damage accumulation (specifically, microcracking) in the specimen, is observed with increasing σ_m or σ_o (cf. Dieter, 1986, Ch. 7). In addition, fractures are not observed in the deformed specimen (Fig. 6). Thus, brittle failure or subcritical crack growth is not considered to have affected the mechanical response characterized in these experiments.

4.3. Q^{-1} Enhancement in the GBS Regime

The subgrain model does not apply to our finer grained specimens because subgrains do not form in ice in the regime of grain boundary sliding rate-limited by sliding on the boundaries (Caswell et al., 2015). In addition, the broad peak observed in the data for the Coarse specimen does not appear at finer grain sizes, though small increases in attenuation are observed, as noted previously, near 0.1 Hz in spectra for both the Very Fine and Fine specimens. In general, the data are better described by continuous enhancement relative to the Andrade model predictions, with greater enhancement at finer grain sizes (Fig. 8).

It is important to note that the diffusion models through which the Andrade model is linked to attenuation assume that grain boundaries are inviscid in shear – that is, no mechanical energy is dissipated by sliding on the boundary, to first order. For materials whose steady-state rheology is dominated by diffusion creep, this assumption breaks down for attenuation at relatively high frequencies (>0.1 Hz), at which point data exhibit increased attenuation relative to the Andrade model (see, e.g., the "master curve" of McCarthy & Cooper, 2016). The assumption of shear-inviscid grain boundaries must be reconsidered for a material deforming by a mechanism in which the grain boundary viscosity is inherently rate-limiting. The enhancement of Q^{-1} across a broad range of frequency in our spectra indicates that this assumption is breaking down at lower frequencies than in the diffusion creep regime; that is, grain boundary effects begin to dominate the entire spectrum, rather than produce a discrete peak, at fine grain sizes.

A continuous distribution in Q^{-1} may be due to either a) a continuous distribution of relaxation length scales, each with a distinct relaxation time, or b) a single length scale that produces a continuous distribution of compliances, as in the case of the high-temperature background effected by chemical diffusion in the context of diminishing potential. If the former, we can estimate the length scale associated with the relaxation time at which the data deviate from the Andrade model by assuming $\tau_r = \eta/G_U$, where η is the viscosity of the relaxation mechanism and G_U is the unrelaxed shear modulus of ice at 240K (3.6 GPa; Gammon et al., 1983). We take the lower bound frequency to be 10^{-3} Hz, where data for the Fine and Very Fine specimens begin to deviate from the Andrade model prediction (Fig. 8). Frequencies in the range of 10^{-3} – 10^{-1} Hz correspond to viscosities on the order of $(3.6\times)10^{12}$–10^{10} Pa s, respectively.

Viscosity can be used to estimate a length scale of diffusion via the expression for diffusion creep (Coble, 1963; Frost & Ashby, 1982; Herring, 1950; Nabarro, 1948):

$$\eta_{Diff} = \frac{kTl^p}{W\Omega\delta D} \qquad [7]$$

where l is the length scale of diffusion, Ω is atomic volume, δ is the grain boundary width (assumed to be $2b$, where b is the magnitude of the burgers vector: 4.5×10^{-10} m), W is a constant, and D is the diffusion coefficient. Equation (7) is derived for a 2D, hexagonal grain network (Raj & Ashby, 1971). For boundary diffusion, $p = 3$, $W = 132$, and D is the grain boundary diffusion coefficient, D_b (Coble, 1963; Raj & Ashby, 1971). For volume diffusion, $p = 2$, $W = 36$, and D is the volume diffusion coefficient, D_v (Herring, 1950; Nabarro, 1948; Raj & Ashby, 1971).

We first apply the boundary diffusion-limited version of Eq. (7), with $\delta = 9\times10^{-10}$ m, $\Omega = 3.27\times10^{-29}$ m^3 (Fletcher, 1970), and $D_b = 6.67\times10^{-15}$ m^2 s^{-1} at 240K (Goldsby & Kohlstedt, 2001; Nasello et al., 2005; Ramseier, 1967). The boundary diffusion coefficient is estimated from the creep data of Goldsby & Kohlstedt (2001) and is an upper bound. Based on Eq. (7), the length scales of relaxation are 3.1 μm at $f = 10^{-3}$ Hz, 1.4 μm at $f = 10^{-2}$ Hz, and 0.7 μm at $f = 10^{-1}$ Hz. The length scales corresponding to volume diffusion are slightly larger: 12 μm at $f = 10^{-3}$ Hz, 3.7 μm at $f = 10^{-2}$ Hz, and 1.2 μm at $f = 10^{-1}$ Hz (employing $D_v = 1.07\times10^{-16}$ m^2 s^{-1} at 240K, after Ramseier, 1967).

Only the largest of these potential length scales approaches the grain size of our specimens: that for volume diffusion at 10^{-3} Hz, 12 μm, which is similar to the grain size of the Very Fine specimen. Conversely, the length scales implied by Eq. (5) at these frequencies (~600 μm at 10^{-3} Hz; see Section 4.2) are substantially larger than the grain size of the Very Fine or Fine specimens. While diffusion at length scales larger than the grain size is possible (and, in fact, required in order to fit the data of Stone et al., 2004 to the compliance distribution of Hart (1970)), eGBS at length scales an order of magnitude larger than the grain size is less plausible because it would require stress heterogeneity at that length scale, which is not consistent with modeled stress concentrations during GBS, where the spacing of stress concentrations is on the order of the grain size (Wei et al., 2008).

Diffusion at a distribution of length scales smaller than the grain size is consistent with the model of constant-hardness compliance articulated at the beginning of this section. That model predicts a distribution of length scales of grain boundary topography (Caswell et al., 2015). In addition, the diffusional component of the compliance in that model is not affected by deviatoric stress, which is consistent with the insensitivity of Q^{-1} to deviatoric stress observed for our samples creeping via GBS. Thus, we attribute the observed broad distribution of enhanced Q^{-1} during GBS creep to diffusion along a distribution of length scales corresponding to grain boundary topography.

A direct comparison between our data and that of McCarthy & Cooper (2016) is warranted. In all cases for which similar grain sizes were investigated, our specimens are approximately one order of magnitude less attenuating than comparable specimens probed by McCarthy & Cooper. In addition, the McCarthy & Cooper data are nonlinear in stress, indicating a contribution of dislocation motion to the observed attenuation. It is possible that, because these authors used a higher sinusoidal stress amplitude (σ_0 = 0.16–0.17 MPa), their experiments accessed the nonlinear regime of the grain boundary compliance distribution described at the beginning of Section 4, which would explain both of these differences; accessing the dislocation-effected regime of the compliance would result in nonlinearity, while dislocation glide across grains – which is pure dissipation – would produce the additional dissipation seen in the McCarthy & Cooper (2016) data. Further exploration of the extrapolation from the Caswell et al. (2015) compliance distribution to the linearity of attenuation as a function of increasing sinusoidal stress amplitude is required to validate this hypothesis. Finally, the McCarthy & Cooper (2016) data do not resolve a peak. According to our observations and this model, one would reasonably be expected in their coarsest grain-sized specimens, which were creeping in the dislocation creep field. This difference is attributed to the improved resolution of our apparatus, which provided much cleaner strain signals and, thus, much higher resolution in Q^{-1} than was available in the McCarthy & Cooper study.

4.4.Geophysical Implications

The attenuation peak exhibited by our Coarse specimen would affect interpretations of terrestrial, seismic observations of glaciers and ice sheets (e.g., Peters et al., 2012; Wiens et al., 2008), where the ice has a grain size on the order of 1 mm, deforms (at least in part) by dislocation creep, and possesses microstructure similar to that of our Coarse specimen, including the presence of subgrains (Weikusat et al., 2009). In this setting, models of attenuation must consider the effect of deformation microstructure – either grain boundary structure or the presence of subgrain boundaries – when inverting attenuation for the properties of the ice. Direct extrapolation of the magnitude of attenuation measured in this study should be done with caution, however, as many glaciers and ice sheets exist at temperatures above 255K, where premelting affects the thermodynamic properties of ice deformation (Dash et al., 1995; Goldsby & Kohlstedt, 2001). Measurements of attenuation need to be performed at temperatures >255K to discern whether the effect of grain boundary topography persists in the regime of premelting.

Enhanced attenuation in the grain boundary sliding regime is likely to affect the despinning timescales of small icy bodies such as Iapetus (e.g., Castillo-Rogez et al., 2011; Levison et al., 2011), where rotational frequencies approach those measured in this study. Tidal forcing at Europa, however, occurs at a frequency lower than that at which the grain boundary effect appears in our data. The Andrade model parameterization for creep of the Coarse specimen is directly applicable to models of ice shell dynamics, however, as the anticipated grain size in a deforming planetary ice shell is expected to be on the order of 1mm (Barr & McKinnon, 2007).

The implications of this work are greatest in the terrestrial seismological context. The data presented here clearly indicate that the attenuation spectrum of a deforming material may be affected – indeed, dominated – by stress-induced length scales much smaller than the grain size. When interpreting seismic waves that have traversed the deforming interior of the Earth, one must therefore consider whether those waveforms have sampled a microstructure finer than the grain size. The method of such consideration is relatively straightforward. We have shown in this section that, for a material deforming via dislocation creep, the composite model of Sundberg & Cooper (2010) given in Eq. (6) represents the measured attenuation well when the length scale of elastically accommodated grain boundary sliding (l in Eq. 5) is the stress-sensitive subgrain size, calculated via Eq. [2]. In tectonic regions where variations in seismic anisotropy suggest changing mantle flow fields (e.g., Peyton et al., 2001), spatial and temporal variability of the stress field should also be evaluated with respect to microstructural evolution. As indicated by data for the Coarse specimen, if the microstructure has not fully equilibrated to changes in stress, grain boundary effects may dominate over a broader frequency range.

5. Conclusion

Attenuation in creeping, polycrystalline water ice, measured at differential strains $\leq 5\times10^{-5}$, which is similar to the strain associated with diurnal tidal flexing of Europa's ice shell (Greenberg et al., 2002), is linear in stress despite a steady-state rheology that is nonlinear. This indicates that at sufficiently low amplitudes of cyclic strain (or stress), attenuation in creeping ice can be attributed to the diffusional component of deformation alone, regardless of a nonlinear steady-state creep response. For coarse-grained, polygonized specimens creeping in the dislocation creep field, the high-temperature background absorption is overlain by a peak due to elastically-accommodated grain boundary sliding. The relaxation time associated with the observed peak is associated with the stress-sensitive subgrain size, not the grain size, and is broadened by the presence of a distribution of subgrain sizes. For specimens deforming via GBS that is rate-limited by sliding on the boundaries, the attenuation spectra deviate from the Andrade model inversion – i.e., the effect of grain boundary viscosity begins to dominate and the assumption of shear-inviscid grain boundaries breaks down – at lower frequencies with decreasing grain size. In the regime where grain boundary viscosity affects attenuation, the form of the spectra may be associated with diffusion along a distribution of length scales of grain boundary topography.

Table 1: Andrade model parameters (β, ψ) determined from least-squares regression of transient creep data, where available. η_{ss} from measured minimum strain rate.

Grain Size	$\boldsymbol{\sigma_{ms}}$ (MPa)	η_{SS} (Pa·s)	$\boldsymbol{\beta}$ ($Pa^{-1}\ s^{-\psi}$)	$\boldsymbol{\psi}$
Coarse (d = 1 mm)	2	1.11×10^{14}	1.65×10^{-11}	0.35
	1	2.94×10^{13}	2.3×10^{-11}	0.19
	0.7	7×10^{13}	3.35×10^{-11}	0.34
Medium ($d \approx 70$ μm)	1	1.1×10^{13}	1.15×10^{-11}	0.20
Fine ($d \approx 40$ μm)	1	1.1×10^{13}	*	*
Very Fine ($d \approx 15$ μm)	1	2.86×10^{12}	*	*

* Transient creep data for this experiment were not available. Values of β and ψ from the Medium specimen were used to predict Q^{-1} for the Very Fine and Fine specimens in Fig. 8.

References

Abers, G. A., Fischer, K. M., Hirth, G., Wiens, D. A., Plank, T., Holtzman, B. K., … Gazel, E. (2014). Reconciling mantle attenuation-temperature relationships from seismology, petrology, and laboratory measurements. *Geochemistry, Geophysics, Geosystems*, *15*(9), 3521–3542. https://doi.org/10.1002/2014GC005444

Anderson, D. L., & Minster, J. B. (1979). The frequency dependence of Q in the Earth and implications for mantle rheology and Chandler wobble. *Geophysical Journal International*, *58*(2), 431–440.

Andrade, E. da C. (1910). On the viscous flow in metals, and allied phenomena. *Proceedings of the Royal Society of London. Series A, Containing Papers of a Mathematical and Physical Character*, 1–12.

Barr, A. C., & McKinnon, W. B. (2007). Convection in ice I shells and mantles with self-consistent grain size. *Journal of Geophysical Research*, *112*(E2). https://doi.org/10.1029/2006JE002781

Barr, A. C., & Pappalardo, R. T. (2005). Onset of convection in the icy Galilean satellites: Influence of rheology. *Journal of Geophysical Research*, *110*(E12). https://doi.org/10.1029/2004JE002371

Barr, A. C., & Showman, A. P. (2009). Heat transfer in Europa's icy shell. *Europa, Edited by RT Pappalardo, WB McKinnon, and KK Khurana, University of Arizona Press, Tucson*, 405–430.

Behn, M. D., Hirth, G., & Elsenbeck II, J. R. (2009). Implications of grain size evolution on the seismic structure of the oceanic upper mantle. *Earth and Planetary Science Letters*, *282*(1–4), 178–189. https://doi.org/10.1016/j.epsl.2009.03.014

Berckhemer, H., Kampfmann, W., Aulbach, E., & Schmeling, H. (1982). Shear modulus and Q of forsterite and dunite near partial melting from forced-oscillation experiments. *Physics of the Earth and Planetary Interiors*, *29*(1), 30–41.

Cassen, P., Reynolds, T., & Peale, S. J. (1979). Is there liquid water on Europa? *Geophysical Research Letters*, *6*(9), 731–734.

Castillo-Rogez, J. C., Efroimsky, M., & Lainey, V. (2011). The tidal history of Iapetus: Spin dynamics in the light of a refined dissipation model. *Journal of Geophysical Research*, *116*(E9). https://doi.org/10.1029/2010JE003664

Caswell, T. E., Cooper, R. F., & Goldsby, D. L. (2015). The constant-hardness creep compliance of polycrystalline ice. *Geophysical Research Letters*, *42*. https://doi.org/10.1002/2015GL064666

Coble, R. L. (1963). A model for boundary diffusion controlled creep in polycrystalline materials. *Journal of Applied Physics*, *34*(6), 1679–1682.

Cole, D. M. (1995). A model for the anelastic straining of saline ice subjected to cyclic loading. *Philosophical Magazine A*, *72*(1), 231–248.

Cole, David M. (1979). Preparation of polycrystalline ice specimens for laboratory experiments. *Cold Regions Science and Technology*, *1*, 153–159.

Consolmagno, G. J., & Lewis, J. S. (1978). The evolution of icy satellite interiors and surfaces. *Icarus*, *34*(2), 280–293.

Cooper, R. F. (2002). Seismic wave attenuation: energy dissipation in viscoelastic crystalline solids. *Reviews in Mineralogy and Geochemistry*, *51*(1), 253–290.

Dalton, C. A., Ekström, G., & Dziewonski, A. M. (2009). Global seismological shear velocity and attenuation: A comparison with experimental observations. *Earth and Planetary Science Letters*, *284*(1–2), 65–75. https://doi.org/10.1016/j.epsl.2009.04.009

Dash, J. G., Fu, H., & Wetlaufer, J. S. (1995). The premelting of ice and its environmental consequences. *Reports on Progress in Physics*, *58*, 115–167.

Dieter, G. E. (1986). *Mechanical Metallurgy* (3rd ed.). McGraw-Hill, Inc.

Exner, H. E. (1972). Analysis of grain- and particle-size distributions in metallic materials. *International Metallurgical Reviews*, *17*(1), 25–42.

Faul, U. H., & Jackson, I. (2005). The seismological signature of temperature and grain size variations in the upper mantle. *Earth and Planetary Science Letters*, *234*(1), 119–134.

Findley, W. N., Lai, J. S., & Onaran, K. (1976). *Creep and Relaxation of Nonlinear Viscoelastic Materials*. New York: Dover Publications.

Fletcher, N. H. (1970). *The chemical physics of ice*. Cambridge, UK: Cambridge University Press.

Frost, H. J., & Ashby, M. F. (1982). *Deformation-Mechanism Maprs, the Plasticity and Creep of Metals and Ceramics*. Pergamon press.

Gammon, P. H., Kiefte, H., Clouter, M. J., & Denner, W. W. (1983). Elastic constants of artificial and natural ice samples by Brillouin spectroscopy. *Journal of Glaciology*, *29*(103), 433–460.

Ghahremani, F. (1980). Effect of grain boundary sliding on anelasticity of polycrystals. *International Journal of Solids and Structures*, *16*(9), 825–845.

Goldsby, D. L., & Kohlstedt, D. L. (1997). Grain boundary sliding in fine-grained ice I. *Scripta Materialia*, *37*(9), 1399–1406.

Goldsby, D. L., & Kohlstedt, D. L. (2001). Superplastic deformation of ice: Experimental observations. *Journal of Geophysical Research: Solid Earth*, *106*(B6), 11017–11030. https://doi.org/10.1029/2000JB900336

Granato, A., & Lücke, K. (1956). Application of Dislocation Theory to Internal Friction Phenomena at High Frequencies. *Journal of Applied Physics*, *27*(7), 789–805. https://doi.org/10.1063/1.1722485

Greeley, R., Sullivan, R., Klemaszewski, J., Homan, K., Veverka, J., Clark, B., … Pappalardo, R. T. (1998). Europa: Initial Galileo Geological Observations. *Icarus*, *135*, 4–24.

Greenberg, R., Geissler, P., Hoppa, G., & Tufts, B. R. (2002). Tidal-tectonic processes and their implications for the character of Europa’s icy crust. *Reviews of Geophysics*, *40*(2). https://doi.org/10.1029/2000RG000096

Gribb, T. T., & Cooper, R. F. (1998). Low-frequency shear attenuation in polycrystalline olivine: Grain boundary diffusion and the physical significance of the Andrade model for viscoelastic rheology. *Journal of Geophysical Research*, *103*(B11), 27267–27279.

Gueguen, Y., & Darot, M. (1982). Upper mantle plasticity from laboratory experiments. *Physics of the Earth and Planetary Interiors*, *29*, 51–57.

Gueguen, Y., Darot, M., Mazot, P., & Woirgard, J. (1989). Q-1 of forsterite single crystals. *Physics of the Earth and Planetary Interiors*, *55*, 254–258.

Hamann, I., Weikusat, C., Azuma, N., & Kipfstuhl, S. (2007). Evolution of ice crystal microstructure during creep experiment. *Journal of Glaciology*, *53*(182), 479–489.

Hammond, N. P., & Barr, A. C. (2014). Global resurfacing of Uranus’s moon Miranda by convection. *Geology*, *42*(11), 931–934. https://doi.org/10.1130/G36124.1

Hart, E. W. (1970). A phenomenological theory for plastic deformation of polycrystalline metals. *Acta Metallurgica*, *18*, 599–610.

Herring, C. (1950). Diffusional Viscosity of a Polycrystalline Solid. *Journal of Applied Physics*, *21*(5), 437–445. https://doi.org/10.1063/1.1699681

Jackson, I., & Faul, U. H. (2010). Grainsize-sensitive viscoelastic relaxation in olivine: Towards a robust laboratory-based model for seismological application. *Physics of the Earth and Planetary Interiors*, *183*(1–2), 151–163. https://doi.org/10.1016/j.pepi.2010.09.005

Jackson, I., Faul, U. H., & Skelton, R. (2014). Elastically accommodated grain-boundary sliding: New insights from experiment and modeling. *Physics of the Earth and Planetary Interiors*, *228*, 203–210. https://doi.org/10.1016/j.pepi.2013.11.014

Jackson, I., Fitz Gerald, J. D., Faul, U. H., & Tan, B. H. (2002). Grain-size-sensitive seismic wave attenuation in polycrystalline olivine. *Journal of Geophysical Research: Solid Earth*, *107*(B12), ECV 5-1-ECV 5-16. https://doi.org/10.1029/2001JB001225

Karato, S. (1989). Grain growth kinetics in olivine aggregates. *Tectonophysics*, *168*, 255–273.

Karato, Shun-ichiro. (1993). Importance of anelasticity in the interpretation of seismic tomography. *Geophysical Research Letters*, *20*(15), 1623–1626.

Ke, T. S. (1947). Experimental evidence of the viscous behavior of grain boundaries in metals. *Physical Review*, *71*(8), 533–546.

Ke, T. S. (1999). Fifty-Year Study of Grain-Boundary Relaxation. *Metallurgical and Materials Transactions A*, *30A*, 2267–2295.

Khurana, K. K., Kivelson, M. G., Stevenson, D. J., Schubert, G., Russell, C. T., Walker, R. J., & Polanskey, C. (1998). Induced magnetic fields as evidence for subsurface oceans in Europa and Callisto. *Nature*, *395*.

Kuroiwa, D. (1964a). Internal Friction of Ice. Ⅰ; The Internal Friction of H2O and D2O Ice, and the Influence of Chemical Impurities on Mechanical Damping. *Contributions from the Institute of Low Temperature Science*, *18*, 1–37.

Kuroiwa, D. (1964b). Internal Friction of Ice. Ⅱ; The Grain Boundary Internal Friction of Ice. *Contributions from the Institute of Low Temperature Science*, *18*, 38–48.

Langdon, T. G. (1991). The physics of superplastic deformation. *Materials Science and Engineering*, *A137*, 1–11.

Levison, H. F., Walsh, K. J., Barr, A. C., & Dones, L. (2011). Ridge formation and de-spinning of Iapetus via an impact-generated satellite. *Icarus*, *214*(2), 773–778. https://doi.org/10.1016/j.icarus.2011.05.031

McCarthy, C., & Cooper, R. F. (2016). Tidal dissipation in creeping ice and the thermal evolution of Europa. *Earth and Planetary Science Letters*, *443*, 185–194. https://doi.org/10.1016/j.epsl.2016.03.006

McCarthy, C., Takei, Y., & Hiraga, T. (2011). Experimental study of attenuation and dispersion over a broad frequency range: 2. The universal scaling of polycrystalline materials. *Journal of Geophysical Research*, *116*(B9). https://doi.org/10.1029/2011JB008384

McKinnon, W. B. (2006). On convection in ice I shells of outer Solar System bodies, with detailed application to Callisto. *Icarus*, *183*(2), 435–450. https://doi.org/10.1016/j.icarus.2006.03.004

McMillan, K. M., Lakes, R. S., Cooper, R. F., & Lee, T. (2003). The viscoelastic behavior of β-In 3 Sn and the nature of the high-temperature background. *Journal of Materials Science*, *38*(12), 2747–2754.

Molodensky, S. M., & Zharkov, V. N. (1982). On the Chandler wobble and variation with frequency of Q in the mantle. *Izv. Akad. Nauk SSSR, Fizika Zemli*, 3–16.

Morris, S. J. S., & Jackson, I. (2009). Implications of the similarity principle relating creep and attenuation in finely grained solids. *Materials Science and Engineering: A*, *521–522*, 124–127. https://doi.org/10.1016/j.msea.2008.09.157

Nabarro, F. R. N. (1948). Deformation of crystals by the motion of single ions. In *Report of a Conference on Strength of Solids* (pp. 75–90).

Nasello, O. B., Di Prinzio, C. L., & Guzmán, P. G. (2005). Temperature dependence of "pure" ice grain boundary mobility. *Acta Materialia*, *53*(18), 4863–4869. https://doi.org/10.1016/j.actamat.2005.06.022

Nimmo, F., Porco, C., & Mitchell, C. (2014). TIDALLY MODULATED ERUPTIONS ON ENCELADUS: *CASSINI* ISS OBSERVATIONS AND MODELS. *The Astronomical Journal*, *148*(3), 46. https://doi.org/10.1088/0004-6256/148/3/46

Nowick, A. S., & Berry, B. S. (1972). *Anelastic Relaxation in Crystalline Solids*. New York: Academic Press.

Ojakangas, G. W., & Stevenson, D. J. (1989). Thermal state of an ice shell on Europa. *Icarus*, *81*(2), 220–241.

Pappalardo, R. T., & Barr, A. C. (2004). The origin of domes on Europa: The role of thermally induced compositional diapirism. *Geophysical Research Letters*, *31*(1). https://doi.org/10.1029/2003GL019202

Pappalardo, R. T., Head, J. W., Greeley, R., Sullivan, R., Pilcher, C., Schubert, G., … Goldsby, D. L. (1998). Geological evidence for solid-state convection in Europa's ice shell. *Nature*, *391*. Retrieved from http://www.planetary.brown.edu/pdfs/1874.pdf

Peters, L. E., Anandakrishnan, S., Alley, R. B., & Voigt, D. E. (2012). Seismic attenuation in glacial ice: A proxy for englacial temperature: ENGLACIAL TEMPERATURE FROM SEISMIC *Q*. *Journal of Geophysical Research: Earth Surface*, *117*(F2), n/a-n/a. https://doi.org/10.1029/2011JF002201

Peyton, V., Levin, V., Park, J., Brandon, M., Lees, J., Gordeev, E., & Ozerov, A. (2001). Mantle flow at a slab edge: Seismic anisotropy in the Kamchatka region. *Geophysical Research Letters*, *28*(2), 379–382.

Piazolo, S., Wilson, C. J. L., Luzin, V., Brouzet, C., & Peternell, M. (2013). Dynamics of ice mass deformation: Linking processes to rheology, texture, and microstructure: Dynamics of Ice Mass Deformation. *Geochemistry, Geophysics, Geosystems*, *14*(10), 4185–4194. https://doi.org/10.1002/ggge.20246

Porco, C. C., Helfenstein, P., Thomas, P. C., Ingersoll, A. P., Wisdom, J., West, R., … others. (2006). Cassini observes the active south pole of Enceladus. *Science*, *311*(5766), 1393–1401.

Prior, D. J., Lilly, K., Seidemann, M., Vaughan, M., Becroft, L., Easingwood, R., … Wilson, C. J. L. (2015). Making EBSD on water ice routine: ICE EBSD. *Journal of Microscopy*, *259*(3), 237–256. https://doi.org/10.1111/jmi.12258

Raj, R. (1975). Transient behavior of diffusion-induced creep and creep rupture. *Metallurgical and Materials Transactions A*, *6*(8), 1499–1509.

Raj, R., & Ashby, M. F. (1971). On Grain Boundary Sliding and Diffusional Creep. *Metallurgical Transactions, 2*, 1113–1127.

Ramseier, R. O. (1967). Self-Diffusion of Tritium in Natural and Synthetic Ice Monocrystals. *Journal of Applied Physics*, *38*(6), 2553–2556. https://doi.org/10.1063/1.1709948

Reynolds, T., & Cassen, P. (1979). On the internal structure of the major satellites of the outer planets. *Geophysical Research Letters*, *6*(2), 121–124.

Schulson, E. M. (2001). Brittle failure of ice. *Engineering Fracture Mechanics*, *68*(17), 1839–1887.

Shimizu, I. (1998). Stress and temperature dependence of recrystallized grain size: A subgrain misorientation model. *Geophysical Research Letters*, *25*(22), 4237–4240.

Stern, L. A., Durham, W. B., & Kirby, S. H. (1997). Grain-size-induced weakening of H2O ices I and II and associated anisotropic recrystallization. *Journal of Geophysical Research*, *102*(B3), 5313–5325.

Stone, D. S. (1991). Scaling laws in dislocation creep. *Acta Metall. Mater.*, *39*(4), 599–608.

Stone, D. S., Plookphol, T., & Cooper, R. F. (2004). Similarity and scaling in creep and load relaxation of single-crystal halite (NaCl). *Journal of Geophysical Research*, *109*(B12). https://doi.org/10.1029/2004JB003064

Sundberg, M., & Cooper, R. F. (2010). A composite viscoelastic model for incorporating grain boundary sliding and transient diffusion creep; correlating creep and attenuation responses for materials with a fine grain size. *Philosophical Magazine*, *90*(20), 2817–2840. https://doi.org/10.1080/14786431003746656

Tatibouet, J., Perez, J., & Vassoille, R. (1987). STUDY OF GRAIN BOUNDARIES IN ICE BY INTERNAL FRICTION MEASUREMENT. *Le Journal de Physique Colloques*, *48*(C1), C1-197-C1-203. https://doi.org/10.1051/jphyscol:1987128

Thomas, P. C., Tajeddine, R., Tiscareno, M. S., Burns, J. A., Joseph, J., Loredo, T. J., … Porco, C. (2016). Enceladus's measured physical libration requires a global subsurface ocean. *Icarus*, *264*, 37–47. https://doi.org/10.1016/j.icarus.2015.08.037

Tobie, G., Choblet, G., & Sotin, C. (2003). Tidally heated convection: Constraints on Europa's ice shell thickness. *Journal of Geophysical Research*, *108*(E11). https://doi.org/10.1029/2003JE002099

Twiss, R. (1977). Theory and Applicability of a Recrystallized Grain Size Paleopiezometer, 227–244.

Waite Jr, J. H., Lewis, W. S., Magee, B. A., Lunine, J. I., McKinnon, W. B., Glein, C. R., … Ip, W.-H. (2009). Liquid water on Enceladus from observations of ammonia and 40Ar in the plume. *Nature*, *460*(7254), 487–490. https://doi.org/10.1038/nature08153

Wei, Y., Bower, A., & Gao, H. (2008). Recoverable creep deformation and transient local stress concentration due to heterogeneous grain-boundary diffusion and sliding in polycrystalline solids. *Journal of the Mechanics and Physics of Solids*, *56*(4), 1460–1483. https://doi.org/10.1016/j.jmps.2007.08.007

Weikusat, I., Kipfstuhl, S., Faria, S. H., Azuma, N., & Miyamoto, A. (2009). Subgrain boundaries and related microstructural features in EDML (Antarctica) deep ice core. *Journal of Glaciology*, *55*(191), 461–472.

Wiens, D. A., Anandakrishnan, S., Winberry, J. P., & King, M. A. (2008). Simultaneous teleseismic and geodetic observations of the stick–slip motion of an Antarctic ice stream. *Nature*, *453*(7196), 770–774. https://doi.org/10.1038/nature06990

Zimmer, C., Khurana, K. K., & Kivelson, M. G. (2000). Subsurface Oceans on Europa and Callisto: Constraints from Galileo Magnetometer Observations. *Icarus*, *147*(2), 329–347. https://doi.org/10.1006/icar.2000.6456

Appendix A: Symbol Key

Symbol	Description
E	Activation Energy
β	Andrade Model, Transient Magnitude
ψ	Andrade Model, Power Law Exponent
ω	Angular Frequency (rad/s)
Ω	Atomic volume
Q^{-1}	Attenuation
R	Ideal Gas Constant
b	Burgers vector
J	Compliance
D	diffusion coefficient (subscript *b*= boundary*;* *v* = volume)
C_E	Dislocation core energy
r_o	Dislocation core radius
ξ	Dislocation energy density (Grain Boundaries)
W	Energy (W_d, energy dissipated; W_s, energy stored) during cyclic loading
f	Frequency
θ	Grain boundary misorientation angle
δ	Grain Boundary Width
C	Grain Boundary Viscosity Temperature Dependence
K	Grain growth constant
d	Grain size
Θ	Gravitational Constant
$\sigma*$	Hardness Parameter, Stress
$\dot{\varepsilon}*$	Hardness Parameter, Strain Rate
λ	Hardness Distribution Shape Factor
l	Length scale of diffusion
p	Length scale dependence, Power-law creep and Diffusion
Mp	Mass, parent planet
m	Mean motion
Y	Modulus, Young's
G	Modulus, Shear
e	Orbital eccentricity
ν	Poisson's Ratio
α	Power-law creep, pre-exponential (Grain size-insensitive)
A	Power-law creep, pre-exponential (Grain size-sensitive)
n	Power-law creep, stress exponent
Q	Quality Factor
Σ	Reciprocal density (Coincident Site Lattice theory)
τ	Relaxation time
r_s	Satellite radius
a	Semi-major axis
ε	Strain
σ	Stress
ds	Subgrain size
B, κ	Subgrain Piezometer constants
T	Temperature
k_2	Tidal Love number, degree-two
t	Time
η	Viscosity